A Home Energy Management Strategy for Load Coordination in Smart Homes with Energy Storage Degradation Quantification

A Thesis

Presented in Partial Fulfillment of the Requirements for the Degree Master of Science in the Graduate School of The Ohio State University

By

Cory Miller, B.Sci.

Graduate Program in Department of Mechanical Engineering

The Ohio State University

2022

Master's Examination Committee:

Dr. Stephanie Stockar, Advisor

Dr. Marcello Canova

Abstract

Modern households are becoming increasingly electrified with all-electric appliances, renewable energy sources, and electric vehicles. While these homes ultimately mitigate the rate of climate change; without a resilient grid, large-scale market penetration is infeasible. To support grid resilience, utility companies have began incentivizing homeowners to defer appliance loads to times of lower electricity via day-time variable pricing schemes. Modern homeowners enrolled in these programs can maximize their financial benefits by installing energy storage systems and energy management strategies which can schedule appliance loads, energy distribution, and energy consumption.

The work in thesis focuses on the design of a home energy management system that schedules multiple smart appliances including plug-in hybrid and battery electric vehicle charging, operation of heating, ventilation, and air conditioning system, energy usage from solar photo-voltaic cells, energy storage and usage from stationary energy storage system, and power consumed from the grid. Considering a day-time variable pricing scheme, the energy management strategy minimizes electrical grid cost to the user, while minimizing user's discomfort in the form of temperature deviation from set-point and time of appliance completion from request. To achieve this goal, the home energy management strategy is formulated

as a model predictive controller and at every time step a multi-objective function is minimized using a meta-heuristic algorithm genetic algorithm.

The performance of the the home energy management strategy is analyzed by comparing results to a simplistic control strategy. A simulation campaign is conducted to compare the relative performance of the the home energy management strategy at a multitude of plant model settings such as house location, house size, stationary energy storage size, and others. Additionally, to ensure the the home energy management strategy does not significantly degrade the stationary energy storage system, a semi-empirical battery aging model is developed to post-process simulation campaign results.

This work resulted in a the home energy management strategy that, on average, reduced yearly electricity cost by $160 while still minimizing user discomfort. Additionally, it was found that the the home energy management strategy did not impose significant battery degradation.

This thesis is dedicated to my grandfather, Reverend John Miller, who lived a life dedicated to bringing joy, acceptance, and unconditional love to anyone he came in contact with. And also to my grandmother, Marcy Miller, whose relentless support and care for our family will never go unnoticed. This work and so much more could not have been done without both of you.

Acknowledgments

I express my sincere gratitude to my advisor, Dr. Stephanie Stockar for her unwavering support, guidance, and creative insight to develop the work in this thesis. Additionally, I cannot express enough how thankful I am for the confidence and encouragement she has had in me to pursue curiosity in my research projects. It has been an invaluable experience to have her as an advisor & mentor and I am thrilled to continue learning from her in future engineering endeavours.

I would also like to thank Mithun Goutham for his immense knowledge in the field modeling and control, as well as his continued mentorship. Also thanks to Dr. Xiaoling Chen for his expertise in battery degradation modeling. This work could not have been completed without both of their technical assistance and teamwork.

Additionally, I would like to thank Dr. Marcello Canova for accepting to be a member of my thesis committee as well as the relevant knowledge I gained from his graduate courses. I am grateful to Rachel Blaser and Prasad Dev Hanumalagutti for their support and guidance throughout this research work.

Finally, I would like to thank my family for their encouragement to pursue this work and specifically to my brother, Brennen Miller, who perpetually motivates me as an engineer by sharing in the joys and excitement of innovation.

Thank you all!

Table of Contents

List of Tables

List of Figures

Chapter 1: Introduction

The summer of 2022 has set countless record high temperatures across the globe. Heatwaves have strewn across Europe throughout much of July such as the UK reaching an all-time high of 40.3C (104.54F) surpassing the prior record of 38.7C set in 2019 [6]. The ever-increasing number and severity of heatwaves are directly harmful to individuals around the world [7, 8]. In the United States from 1999 to 2003, heat-related deaths were responsible for more deaths than any other weather related event [9, 10]. In many cases, the heatwaves caused grid system damages, economical losses, and disruptions via unprecedented demand on utilities and subsequent power outages [11].

The increase in severity and frequency of extreme weather events has resulted in decreasing electrical grid reliability [12]. Approaches to ensure the integrity of the grid span from the macro-scale, such as creating utility resiliency during high demand times with energy storage systems [13] to the micro-scale, such as incentivising individual households to defer heating ventilation and air conditioning loads to off-peak times with customer demand response programs [14]. For example, a homeowner could wait until later in the day when electricity cost is low to turn on their laundry machine. Due to manual or automatic load deferral

of home appliances to off-peak demand times, electricity cost savings of approximately 12% has been reported [15–17]. This type of solution will increase the resiliency of the grid during high demand times, and if done automatically via an integrated controller, can maximize the electricity cost savings to the homeowner without the need for human interaction.

Aside from climate change forcing abnormal peak power demands on the grid, other factors are also perpetuating the need to reconsider the timing and amount of electricity consumption used in our homes. From 2005 to 2015, the total number of all-electric homes in the United States increased by approximately 5% [18]. This increase may seem insignificant; however, the rapid rate of all-electric adoption dates back to 1980 in which before that year, only 17% of homes built were all-electric and after that year the number was 35% [18]. The expanding growth of electricity use in the residential sector overtime is summarized in Figure 1.1 that shows the source of energy utilization in the United States over 70 years [1].

Additionally, moderns homes have began integrating local generation from renewable energy sources, such as solar photovoltaic systems, with stationary energy storage systems [19, 20]. It is projected that this increase in local renewable generation in conjunction with the possibility of saving energy for later use will help decrease the total amount of energy drawn from the grid by the residential sector [21].

In this context, to maximize energy cost savings to homeowners, a home energy management (HEM) strategy could be utilized to optimize home energy consumption and renewable energy generation against variable grid electricity prices. Additionally, with the increased use of stationary energy storage, the HEM strategy

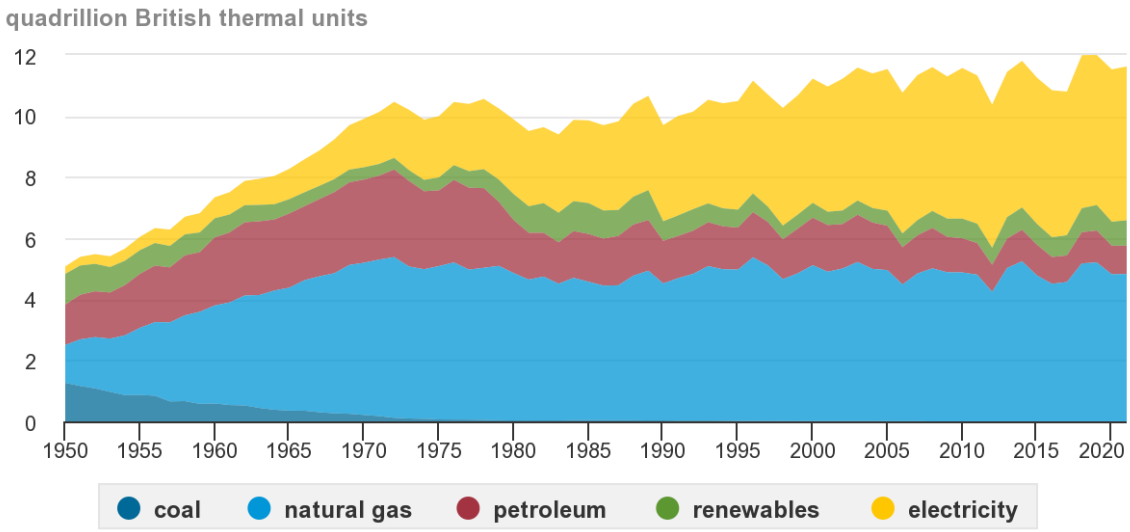

Figure 1.1: U.S. Residential Sector Energy Consumption by Energy Source, 1950 to 2021 [1]

could be used to manage energy storage charge and discharge commands to save energy for high electricity cost times or to ensure excess renewable energy is not wasted during times of low demand.

1.1 Affecting User Behavior via Utility Pricing Schemes

Electric utilities in the United States and elsewhere have understood that demand response programs, hence encouraging consumers to shift and reduce their electricity usage, are an effective tool to maintain resiliency in their grid systems [22]. In general, utility-side demand response management programs are be classified into three categories [2]:

1. Direct Load Control which utilities remote shut down of load regions (neighborhoods) during high demand to avoid system failure [2].

2. Load Leveling which flattens the overall demand curve. For example, peak clipping which is the shifting of consumer loads from high demand times to low demand times [2].

3. Incentive-Based Strategies to encourage users to shift their loads to off-peak hours. For example, discounted electricity cost during times of low demand [2].

Specific management strategies for realizing the aforementioned programs are summarized in Figure 1.2.

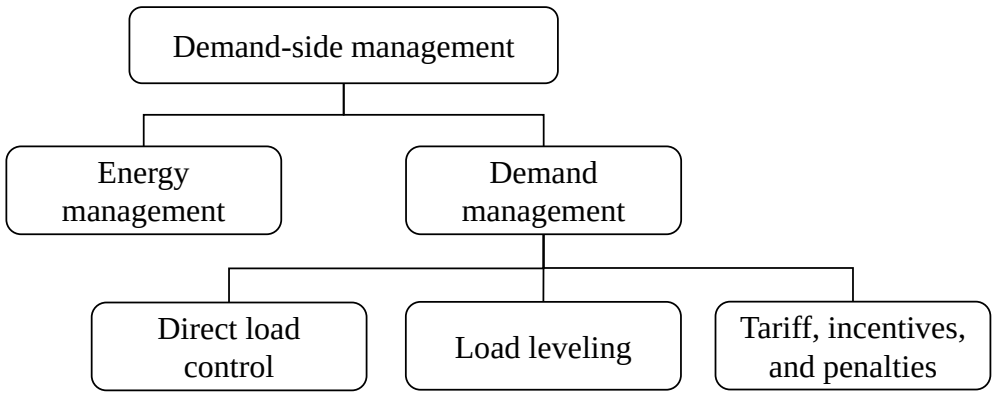

Figure 1.2: Demand-Side Management Strategies and Programs [2]

For the residential sector, incentive-based strategies or demand response plays a critical role in peak-demand shaving, risk and reliability management, carbon emission reduction, and energy cost reduction [23]. This is realized by using the price of energy as a control signal to encourage specific user consumption behavior.

For example, completing high demand loads during times of low grid demand such as the middle of the night [23]. Most commonly, time of use pricing is used which predetermines variable pricing throughout the day [24]. Less commonly, real time pricing is implemented which varies daily pricing based on predicted future demand in the grid [24].

In this thesis, a smart home enrolled in a demand side program with a time of use electricity pricing scheme is considered.

1.2 Home Energy Management Systems

The objective of a HEM strategy is to integrate and coordinate all the electric loads in a house [25]. When a smart home is enrolled in a demand response program, the home energy management strategy can be used to schedule smart appliances such as heating, ventilation, and cooling (HVAC), laundry and dish-washing, and vehicle charging to minimize the user's electricity costs and meet any additional program requirements such as maximizing instantaneous power [26] or minimizing user discomfort to ensure acceptability.

1.2.1 Current Deployments of Home Energy Management Systems

The popularity of demand side management has grown in recent years as grid utilities are motivating home owners with cost incentives and government entities are funding research projects to help curb grid reliability issues. In 2021 the United States Department of Energy announced a $61 million investing initiative for select communities to accelerate the research and adoption of grid-interactive efficient buildings [27]. As part of this demonstration program, Oak Ridge National

Laboratory has implemented a demand response program that aimed to curb the HVAC power consumption in a community of 62 homes in Reynolds Landing in suburban Birmingham, Alabama [28]. Results show 15% reduction in peak electricity demand, while meeting customer acceptability requirements.

Similarly, in 2018, the National Renewable Energy Laboratory in collaboration with Xcel Energy, a large Colorado utility company, investigated the integration of vehicle charging and solar power generation as part of demand-response programs [29]. The deployment program included ten homes retrofitted with solar panels, stationary energy storage and with owners that drove plug-in electric or electric vehicles. The coordination strategy resulted in a 81.7 MWh surplus during peak demand times, compared to an average of 69.2 MWh consumption by the conventional homes.

Finally, the California Energy Commission, together with the Alternative Energy Systems Consulting Inc., studied the effect of integrating smart thermostat with plug-in electric and electric vehicle charging, solar generation, and stationary energy storage [30]. Using a time of use pricing scheme, the implementation of demand response resulted in 38% reduction of energy demand during peak hours.

1.2.2 Online Solution Methods for Household Load Scheduling

For online deployment of a HEM strategy for flexible load scheduling, HVAC operation, and renewable energy generation, a computationally efficient approach must be utilized. Although offline approaches can be used to determine optimal energy management, they require an input of the exact timing of appliance requests, ambient temperature, and available energy for renewable generation.

To solve the demand side management problem online, a number of computationally efficient approaches have been investigated in literature, mainly heuristic and meta-heuristic approaches [31]. These approaches can be classified into three categories: swarm intelligence techniques, evolutionary algorithms, and general recursive algorithmic techniques.

Among the swarm intelligence techniques, particle swarm optimization (PSO) has been used to solve many real world optimization applications including the demand side management scheduling problem [32–34]. In [35], a receding horizon approach was used, in which the nonlinear optimization problem was solved with PSO with the goal of minimizing user cost by scheduling interruptible appliance loads and HVAC operation. The problem was solved in response to various electricity pricing schemes and achieved reductions in electricity cost to the user of 10% by rescheduling appliance loads and vehicle charging around a time of use pricing scheme [35].

Hybrid approaches have also been utilized in a large body of literature which invoke both optimization-based and heuristic approaches to achieve more efficient calculation for online implementation. In [31], a hybrid approach was used by implementing PSO for its global search capabilities and sequential quadratic programming for its local search capabilities. The HEM strategy optimized energy storage operation, grid consumption, fuel cell energy generation, and scheduling of deferrable appliance loads online. The house temperature was also ensured to be set between a desirable range [31].

The genetic algorithm is an evolutionary algorithm that is found to outperform the PSO in optimization problems that involve discrete variables [36]. For

this reason, the genetic algorithm has been widely applied in literature for the online, household scheduling problem where appliance activation is modeled using discrete variables. The optimization of discrete variables involved in the energy scheduling of a smart home is addressed in [37] by using a genetic algorithm. In [38], the genetic algorithm was successfully applied for the optimal scheduling of air conditioners and inverters to reduce the electricity bills and peak load under a real time electricity pricing scheme. To reduce the electricity expense and alleviate the peak to average ratio, [39] implemented genetic algorithm to solve a nonlinear optimization problem considering a combined pricing model to avoid high peak to average ratio in the lowest electricity price region. In [40] a genetic algorithm-based optimization approach was used to meet a controllable heating, ventilation, and cooling load with higher efficiency of a hybrid system that combines renewable energy sources and energy storage systems. In [41], by redistributing the deferrable loads equally to all the time slots, the demand side management problem was realized with an objective to minimize the power utilization during the electricity rush hour and this was solved using genetic algorithm and succeeded in reducing the overall power utilization by 22%. In addition to electricity cost, genetic algorithm was also utilized to optimize the consumer comfort in [42, 43].

1.3 Energy Storage Systems and Battery Degradation

The integration of distributed electricity generation from renewable energy sources, such as photovoltaic solar panels, in smart homes yields the potential for drastic consumer-end energy savings. For example, a 400 square foot array of solar panels on a roof has the potential to cover the entirety of a house's energy consumption

which totals approximately 900 kWh per month [44]. However, like for many renewable sources, this electricity generation rate is highly variable due to differences in weather and season. Even for the average-sized photovoltaic system, the mismatch between solar power production and simultaneous household loads could result in a significant power surplus, especially during peak daytime solar irradiance [45]. Therefore, it is difficult to impose an efficient HEM strategy to control power distribution from the renewable energy source [46].

This issue can be addressed by integrating appropriately sized lithium-ion batteries, such that the excess power generated can be stored and used in periods of insufficient solar power, instead of drawing power from the electricity grid. This has also become increasingly viable economically because of a continued trend of decreasing prices of lithium-ion batteries, which are predicted to be the technology of choice for residential applications, with an 89% drop in the cost per kWh between 2010 and 2020 [47, 48]. It has been found that in some states, energy storage systems paired with residential solar panels can actually yield a greater return on investment than selling back surplus electricity with a photovoltaic system only [49].

In a household equipped with photovoltaic and an energy storage system, a HEM strategy could be capable of determining the charge-discharge strategy for the utilization of the energy storage system in response to a time of use pricing scheme and free power available from the photovoltaic panels.

An important factor considered by potential energy storage system adopters is the useable lifetime of the battery, which is associated with the return on investment. Battery aging with capacity fade is also crucial to an HEM strategy because

it reduces the ability of the battery to meet the energy demands of the home appliances. Therefore, the relationship between the HEM strategy and battery aging should be investigated.

1.3.1 Current Practices for Modeling Battery Degradation

When integrating an energy storage system with a HEM strategy, the battery will be periodically charged from either renewable or grid power sources, and then discharged to supply energy to the appliances. This cycling behavior ages the battery in addition to the calendar aging mode [50, 51]. The battery aging causes capacity decay and resistance increase which reduces the energy and power performance of a battery respectively [52].

A large body of literature focuses on understanding and mitigating battery aging using both experimental and modeling techniques [3, 53]. For modeling the battery aging phenomenon, different approaches have been utilized ranging from physics-based, partial differential equation models to data driven approaches [3, 51, 54]. A comparison of different lumped parameter models has been presented in [55].

Physics-Based battery aging models are built starting from the basic electrochemical mechanisms in a battery that are related to aging process. Such mechanisms include the increase of solid electrolyte interface (SEI) layer [51], the loss of active materials (LAM) [4, 56], lithium plating [57], and cracks in the SEI layer [58, 59]. For example, the aging due to SEI layer growth can be physically described by modeling the side reaction between lithium and the electrolyte using the Tafel and Nernst equations [51] and the crack in either the active material of

the SEI layer can be predicted using equations describing the relations between, stress strain, displacement, or volume change [58]. Although including additional details in the model equations will improve the accuracy of modeling, the computational complexity is also increased. Moreover, the time scales of the electrochemical events inside the battery are much faster compared to dynamics of the energy management systems, making the numerical simulation more challenging.

Fully data-driven battery aging models are computationally efficient, but lose the connection with the underlying physics. Simple data-driven models implement generic data fitting equations such as an empirical aging law [60], or the Arrhenius law equation [61]. In contrast, more advanced data-driven approaches have been developed where a deep learning algorithm is used to emulate the aging phenomenon [54], or where the remaining useful battery life is determined via a Monte Carlo simulation algorithm [62]. While data-driven aging model approaches can reduce computation time significantly, they always lack confidence in results outside of their calibration range.

Finally, semi-empirical aging models are a mix of physics-based and data-driven approaches. These models simplify the physical process in the battery aging mechanisms with assumptions in either the limiting factors or the working conditions such as the C-rate, temperature, or state of charge (SOC) values [3,59]. Most semi-empirical models further decouple battery aging from the original electrochemical reactions because of the distinct time scales for the two processes. With this, the aging models are simplified into feedforward models without affecting the battery model parameters over a short duration [3].

1.4 Contributions

Although there is large set of literature committed to solving the demand side energy management and scheduling problem, the cost benefits of implementing a HEM strategy for a multitude of household types has yet to be investigated. Additionally, a developed HEM controller should be easily implementable regardless of household; therefore, the strategy should solve the problem with approximately equal performance, irrespective of model settings. For these reasons, a sufficiently fast HEM strategy should be developed to conduct an extensive simulation campaign across a wide range of model settings.

The contributions of this thesis are:

- **The development of a real-time capable home energy management strategy**: In this thesis, a HEM algorithm is developed for the optimal coordination of the electric loads in a smart home. The strategy is designed to minimize the total operating cost to the user, while satisfying user acceptability requirements. To allow for online implementations and applications to simulation studies, the proposed strategy is required to compute in real time. These objective are achieved by formulating the optimization problem as a sequential receding horizon problem.

- **The evaluation of benefits obtained by the integration of an optimization-based home energy management strategy**: In this thesis the cost savings performance of the proposed strategy is compared against a baseline scenario. Hence, when no coordination nor scheduling is performed. This study considers location, seasonality, and house characteristics as variable factors.

- **The development of a semi-empirical battery degradation model**: In addition to total savings obtained by the proposed HEM strategy, a metric associated with battery utilization and associated degradation is also included. To determine the effect of load scheduling on battery life, a simple semi-empirical battery degradation model is presented in this thesis.

- **The preliminary evaluation of fast charging technologies on battery life**: The proposed semi-empirical degradation model is used to develop a real-time capable strategy for a direct-current fast charging profile that accounts for both, the degradation due to the charging event together with the effect of the upcoming driving event.

1.4.1 Publications

- Miller, C., Goutham, M., Chen, X., Hanumalagutti, P., Blaser, R., Stockar, S. "A Semi-Empirical Approach to a Physically Based Aging Model for Home Energy Management Systems" IEEE Conference on Control Technology and Applications, 2022.

- Miller, C., Goutham, M., Chen, X., Stockar, S. "DC Fast Charging Optimization for Capacity Fade Minimization" IFAC International Symposium on Advances in Automotive Control, 2022.

- Chen, X., Goutham, M., Miller, C., Hanumalagutti, P., Blaser, R., Stockar, S. "The Effect of Optimal Load Scheduling on the Performance of Smart Home Management System"

Chapter 2: Prior Work

In this chapter, a summary of previous work to develop the smart home plant model and its subsystems together with a simple baseline controller is given. The complete description of the model and baseline control development is given in [63, 64].

2.1 Smart Home Plant Model

The purpose of the smart home model is to capture the overall energy demand and its distribution among all subsystems in the home due to predicted user activities. This model will be used as a plant model for the load controller development.

The smart home model consists of energy consuming subsystems such as the HVAC operation, plug-in electric and electric vehicle charging, and user activities; together with energy generating subsystems such as solar panels; and energy storage components. Figure 2.1 illustrates the subsystems in the smart home where subsystems inside the home are energy consuming and energy generating or storing subsystems are outside the home in the figure.

The relation that governs the operation of all the subsystems included in this model is the power balance between the energy demand and supply:

$$P_{Grid} + P_{Solar} + P_{ES} = P_{HVAC} + P_{xEV} + P_{Appl,C} + P_{Act,NC} \tag{2.1}$$

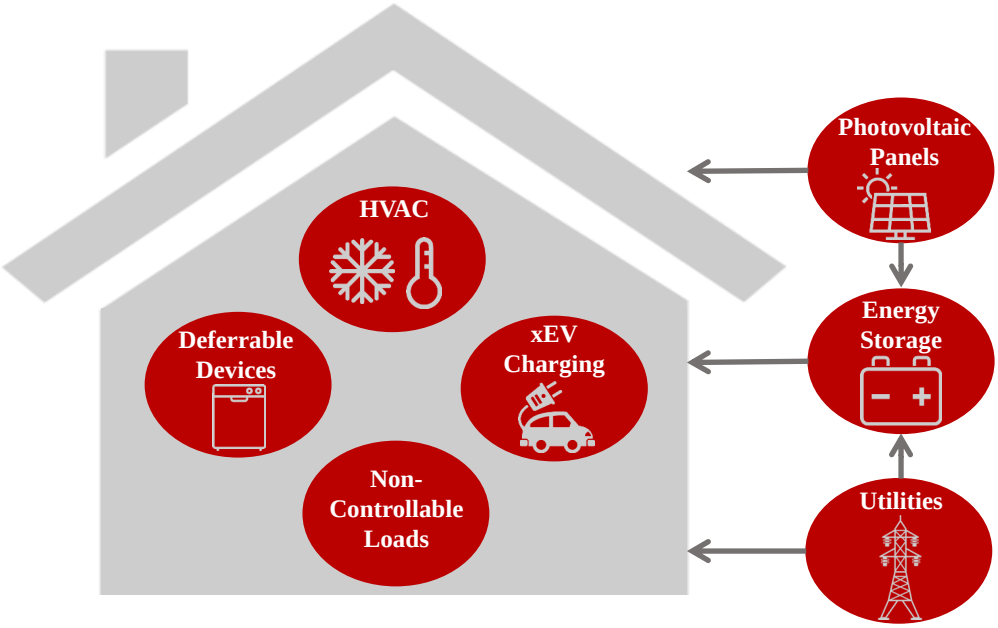

Figure 2.1: Smart Home Plant Model

Where P_{Grid} is the power consumed by the grid, P_{solar} is the power generated by the solar panels, P_{ES} is the power to charge or discharge the battery, P_{HVAC} is the power for the operation of HVAC, P_{xEV} is the power to charge the plug-in electric or electric vehicle, $P_{Appl,C}$ is the power consumed due to controllable appliances, and $P_{Act,NC}$ is the power consumed due to non-controllable activities. It is worth noting that in the power balance, positive energy storage power corresponds to discharging.

2.1.1 Photovoltaic System

The power generated by a photovoltaic panel system is calculated using a simple relationship as presented in [65].

$$P_{Solar}(t) = \eta_{PV} \cdot G(t) \cdot A_{PV} \tag{2.2}$$

Where η_{PV} is the efficiency of the solar panel, which is assumed to be a function of the ambient and panel temperature, $G(t)$ is the useful solar irradiation power density, and A_{PV} is the total area of the solar panels [64].

The useful solar irradiation power density, $G(t)$, includes the direct solar radiation and the diffuse solar radiation and is mapped based on location, season, and panel tilt using the System Advisor Model [66]. The power generated for the household is simply calculated by multiplying the solar irradiation power density by the are of the solar panels.

2.1.2 Residential Energy Storage

The power associated with the stationary energy storage is:

$$P_{ES}(t) = \begin{cases} V_{ES}(t) \cdot I_{ES}(t) \cdot \eta_{ES} & I_{ES}(t) > 0 \\ V_{ES}(t) \cdot I_{ES}(t) / \eta_{ES} & I_{ES}(t) < 0 \end{cases} \tag{2.3}$$

where η_{ES} is the battery charging and discharging efficiency, which is assumed to be constant, V_{ES} is the battery voltage, and I_{ES} is the battery pack current.

The energy storage pack voltage is given by:

$$V_{ES}(t) = V_{ES,cell}(t) \cdot N_{ES,series} \tag{2.4}$$

where $N_{ES,s}$ is the number of cells in the pack in series, $V_{ES,cell}$ is the cell voltage determined using a 0th order equivalent circuit model [67]:

$$V_{ES,cell}(t) = V_{OC}(SOC_{ES}, T_{ES}) - R_0(SOC_{ES}, T_{ES}) \cdot I_{ES,cell}(t) \tag{2.5}$$

where $I_{ES,cell}(t)$ is the current applied to individual cells, R_0 is the internal resistance of each cell which is a function of state of charge and temperature of the

pack, and V_{OC} is the open-circuit voltage which is also a function of state of charge and temperature of the pack. The internal resistance and open circuit voltage are mapped based on the values from [67].

Due to the relatively low currents applied to residential energy storage systems, the heat generation of the batteries is assumed to be negligible and a thermal model is not included for the energy storage system. Instead the battery temperature is assumed to be either the same as ambient temperature if stored outside, or the same as the house temperature if stored inside.

The cell current is calculated as:

$$I_{ES,cell}(t) = I_{ES}(t)/N_{ES,p} \tag{2.6}$$

Where $N_{ES,p}$ is the number of cells in the pack in parallel.

Finally, the state of charge, is determined by:

$$\frac{dSOC_{ES}(t)}{dt} = -\frac{I_{ES,cell}(t)}{Q_{cell}} \tag{2.7}$$

Under the assumption that there is no imbalance in the pack and where Q_{Cell} is the nominal cell capacity.

The number of cells in series and parallel are selected to meet the desired total pack capacity $Q_{ES,des}$ and voltage $V_{ES,des}$:

$$Cells_{ES,parallel} = Q_{ES,des}/Q_{cell} \tag{2.8}$$

$$Cells_{ES,series} = V_{ES,des}/V_{cell} \tag{2.9}$$

Where $Q_{ES,des}$ is the desired pack capacity and $V_{ES,des}$ is the desired pack voltage. Both of these values are set to be equivalent to the specifications of the Tesla Powerwall 2 as was done in [64] as a reference for sizing where the desired capacity

is 13.5 kWh and the desired voltage is 50V. Depending on the size of the house, multiple energy storage units of 13.5 kWh can be added.

2.1.3 HVAC

The electric power demand associated with the HVAC system operation is the summation of the heating or cooling power and the fan regulation power:

$$P_{HVAC}(t) = \begin{cases} P_{heat} + P_{fan} & T_\infty \leq T_{ref} \\ P_{cool} + P_{fan} & T_\infty > T_{ref} \end{cases} \tag{2.10}$$

where P_{heat} is the heating power, P_{cool} is the cooling power, P_{fan} is the fan power, T_∞ is the environment temperature, and T_{ref} is a threshold temperature to determine when to switch between heating and cooling operation [63]. When the ambient temperature is less than the reference temperature then it is assumed to be winter and when the ambient temperature is greater than the reference temperature then it is assumed to be summer.

The energy consumed during heating and cooling operation is:

$$P_{heat} = \frac{\dot{m}_{HVAC} \cdot \pi(t) \cdot c_p \cdot \Delta T}{COP(\Delta T)}, \ \Delta T = T_{HVAC} - T_\infty \tag{2.11}$$

$$P_{cool} = \frac{\dot{m}_{HVAC} \cdot \pi(t) \cdot c_p \cdot \Delta T}{SHR \cdot COP(\Delta T)}, \ \Delta T = T_\infty - T_{HVAC} \tag{2.12}$$

where $\dot{m}_{HVAC}$ is the HVAC mass flow rate, π is the fan regulation command, c_p is the air specific heat capacity at constant pressure, ΔT is the temperature difference between the HVAC supply air temperature and the ambient temperature, T_{HVAC} is the supply air temperature of HVAC, SHR is the Sensible Heat Ratio, and COP is the Coefficient of Performance as described in [63]. Note that the heating system

can only be on or off; therefore, π can only be 1 or 0. However, the cooling system is assumed to have a 3 state capability; on, off, or half load.

The energy consumed by the fan is:

$$P_{fan} = \frac{\dot{m}_{HVAC} \cdot \Delta P}{\eta_{fan} \cdot \rho_{air}} \tag{2.13}$$

where ΔP is the static pressure drop, η_{fan} is the constant efficiency of the fan, and ρ_{air} is the air density.

The governing equation for the household temperature dynamics is obtained by applying conservation of energy to the control volume represented by the house:

$$m_a c_v \frac{d}{dt} T_a(t) = \pi(t) \cdot \dot{m}_{HVAC} \cdot c_p [T_{HVAC} - T_a(t)] - \frac{T_a(t) - T_\infty}{R_{tot}} \tag{2.14}$$

where m_a is the air mass inside the house, c_v is the air specific heat capacity at constant volume, T_a is the air temperature inside the house, and R_{tot} is the equivalent thermal resistance of the interface between house and environment. The detailed model development is presented in [68].

2.1.4 Plug-in Electric and Electric Vehicle Charging

The modeling of the vehicle charging follows the same approach to the charging of the energy storage system. The power required to charge the vehicle is:

$$P_{xEV}(t) = V_{xEV}(t) \cdot I_{xEV}(t)/\eta_{xEV} \tag{2.15}$$

Where η_{xEV} is the constant charge efficiency of the battery, $I_{xEV}(t)$ is the current applied to the battery pack, and $V_{xEV}(t)$ is the battery pack voltage:

$$V_{xEV}(t) = V_{xEV,cell}(t) \cdot N_{xEV,s} \tag{2.16}$$

Where $N_{xEV,s}$ is the number of cells in the pack in series, $V_{xEV,cell}$ is the cell voltage determined using a 0th order equivalent circuit model [67]:

$$V_{xEV,cell}(t) = V_{OC}(SOC_{xEV}) - R_0(SOC_{xEV}) \cdot I_{xEV,cell}(t) \tag{2.17}$$

Where $I_{xEV,cell}(t)$ is the current applied to individual cells, R_0 is the internal resistance of each cell which is a function of state of charge, and V_{OC} is the open-circuit voltage which is also a function of state of charge. The internal resistance and open circuit voltage are mapped based on the values from [67].

The cell current is calculated as:

$$I_{xEV,cell}(t) = I_{xEV}(t)/N_{xEV,p} \tag{2.18}$$

Where $N_{ES,p}$ is the number of cells in the pack in parallel.

Finally, the state of charge is determined by:

$$\frac{dSOC_{xEV}(t)}{dt} = -\frac{I_{xEV,cell}(t)}{Q_{cell}(t)} \tag{2.19}$$

Under the assumption that there is no imbalance in the pack and where Q_{cell} is the nominal cell capacity.

The number of cells in series and parallel are selected to meet the desired total pack cpacity $Q_{xEV,des}$ and voltage $V_{xEV,des}$:

$$N_{xEV,p} = Q_{xEV,des}/Q_{cell} \tag{2.20}$$

$$N_{xEV,s} = V_{xEV,des}/V_{cell} \tag{2.21}$$

The desired vehicle model is an input to the system; based on this input, the battery capacity, $Q_{xEV,des}$, and voltage, $V_{xEV,des}$, can be determined [64].

The initial state of charge of the vehicle at plug-in is modeled as a function of vehicle efficiency and miles traveled. Additionally, the expected time of plug-in at home can be modeled based on the EV Project data [64, 69].

The vehicle battery is charged with a standard level 2 charger with a constant 7.56 kW applied during charging. The vehicle is charged with a constant-current constant-voltage charging protocol. The total energy demanded by the vehicle battery to reach full charge can be determined using the 0th order equivalent circuit model described prior.

2.1.5 User Activities

Finally, a number of user activities that are associated with a power demand are considered. The model is based on a statistical approach and is developed to reproduce the data collected as part of the ATUS census [68, 70].

For the model development, user activities are divided among deferrable and non-deferrable loads. The non-controllable activities in the model include sleeping, no-power activity, cleaning, cooking, and leisure. The power request associated with each non-controllable activities is summarized in Table 2.1.

Table 2.1: Operating Power of Non-Controllable Activities

Activity	**Power $P_{Act,NC}$ [W]**
Sleeping	0
No-Power Activity	0
Cleaning	1250
Cooking	1225
Leisure	300

Similarly, activities related to the utilization of smart appliances, such as operating the dishwasher and doing laundry, have been considered. For laundry, an all-in-one machine is considered in which washer and dryer are combined in a single unit. The power demands associated with deferrable loads are summarized in Table 2.2.

Table 2.2: Operating Power and Time of Controllable Appliances

Appliance	**Power $P_{Appl,C}$ [W]**	**Operating Time [min]**
Laundry - Washer	425	30
Laundry - Dryer	3400	30
Dishwasher	1800	60

An example of daily user activities is illustrated in Figure 2.2. The corresponding power demand from the user activities are also summarized in Figure 2.2.

2.2 Baseline Controller

To simulate the household plant model, a simple baseline controller which reproduces the scenario of no load coordination was developed. The baseline strategy includes a dead-band control on the HVAC system to maintain the house indoor temperature within desired bounds, an energy storage controller that charges the battery when there is solar surplus and discharges when the power demand is not met by the solar panel energy generation, and the requests of controllable devices are fulfilled as soon as requested without any deferred operations. The integration of the baseline controller with the smart home plant model is illustrated in Figure

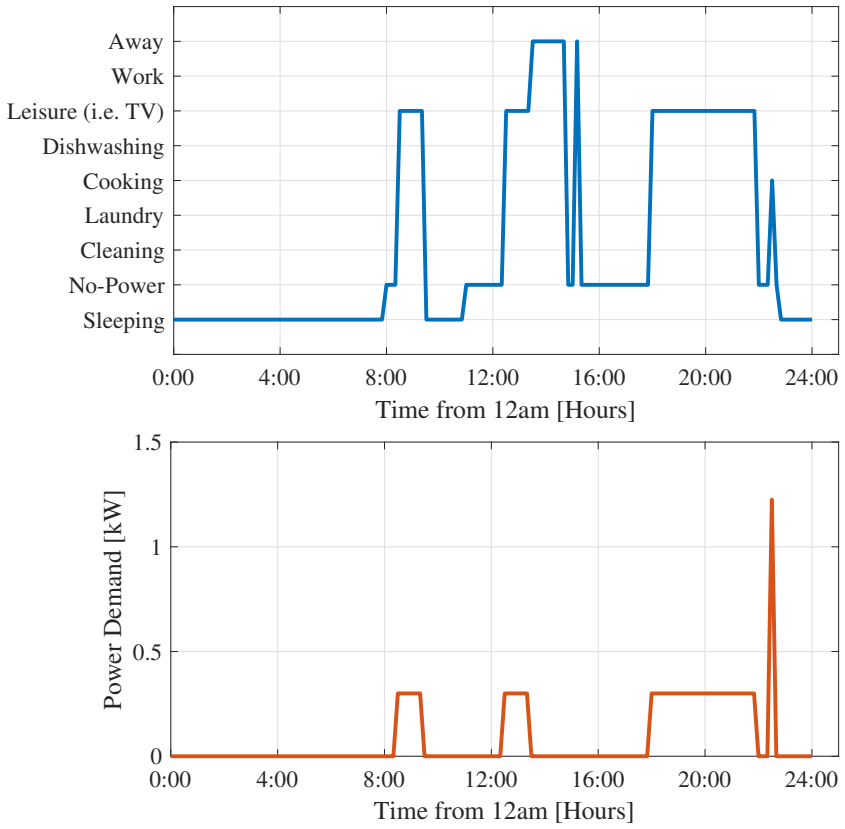

Figure 2.2: Example of Daily User Activity and Corresponding Power Consumption

2.3 where the case definition variables represents the external inputs depending on plant model settings, for example ambient temperature depending house location.

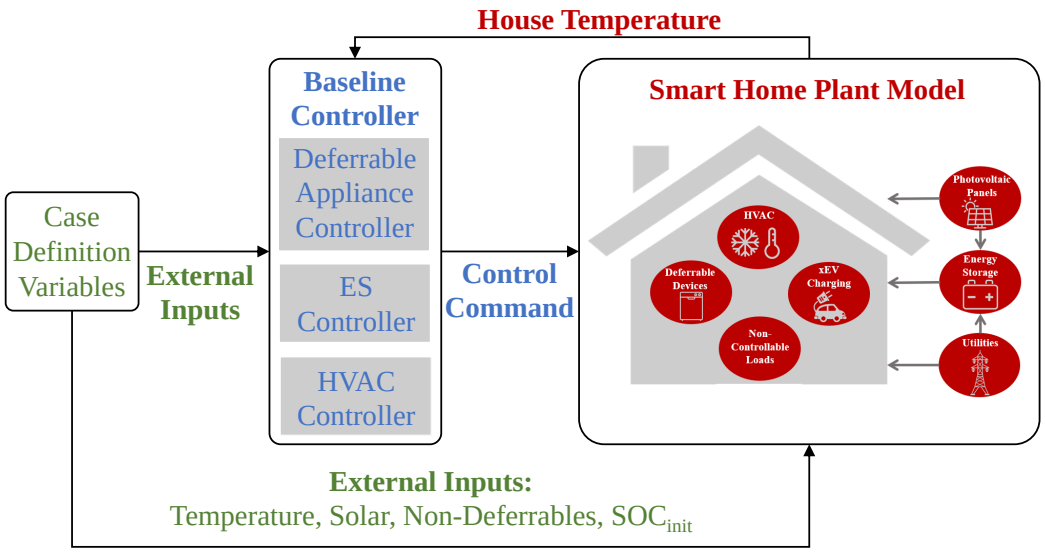

Figure 2.3: Baseline Control Integration with the Smart Home Plant Model

2.2.1 HVAC Dead-Band Control

The baseline thermostat HVAC control aims to ensure that the household temperature T_a remains within the desired bound with a bang-bang controller that will only impose on or off commands. For example, in summer when the ambient temperature is above a certain temperature threshold, the HVAC is set to cooling operation and will turn on when the household temperature surpasses a certain set point and tolerance:

$$\pi_{cool} = \begin{cases} 0 & \text{if } T_a \leq T_{des} - \Delta T_{band} \\ 1 & \text{if } T_a > T_{des} + \Delta T_{band} \end{cases}, \tag{2.22}$$

$$\pi_{heat} = \begin{cases} 1 & \text{if } T_a < T_{des} - \Delta T_{band} \\ 0 & \text{if } T_a \geq T_{des} + \Delta T_{band} \end{cases} \tag{2.23}$$

where T_{des} is the desired temperature set by the thermostat and ΔT_{band} is the half width of the temperature tolerance band.

2.2.2 Energy Storage Charge and Discharge Control

The stationary battery is controlled based on the power balance defined in Equation 2.1 and the availability of surplus solar energy.

The baseline controller utilizes the solar power to meet the instantaneous household power demand. If the generation is greater than the demand and the state of charge is less than 90%, the surplus power is used to charge the battery. When the solar generation is less than the total demand and the state of charge of the battery is higher than 20%, power is drawn from the energy storage system. Any additional power deficit is then covered by drawing from the electrical grid.

$$\pi_{ES} = \begin{cases} 1 & \text{if } SOC_{ES} < 0.9 \ \& \ P_{Solar} \leq P_{Household} \\ -1 & \text{if } SOC_{ES} > 0.2 \ \& \ P_{Solar} > P_{Household} \\ 0 & \text{else} \end{cases} \tag{2.24}$$

Where $P_{Household}$ is the summation of the power consuming household operations as shown on the right hand side of the power balance in Equation 2.1.

2.2.3 Deferrable User Activities and Vehicle Charging

In the baseline scenario, deferrable user activities and vehicle charging demands are met as soon as requested. For example, if a user turns on the dishwasher, the appliance runs immediately. Similarly, if a user plugs in a vehicle at 7pm and requires 10 kWh to fully recharge, the vehicle will start charging at 7:00 pm and be completely charged by approximately 8:20 pm.

Chapter 3: Home Energy Management System Controller

In this chapter, a multi-objective optimization problem is formulated as a decentralized model predictive control problem with a receding time horizon, which is then solved using a meta-heuristic optimization algorithm. The results from a one-day simulation are analyzed as a sample. Finally, a simulation campaign is conducted to analyze the operation of the developed smart home plant model with two types of controllers and various model settings simulated over a one-year time period each.

3.1 Formulation of the Optimization Problem

The objective of the smart home energy management algorithm is to coordinate the scheduling of smart appliances, vehicle charging and operate the HVAC to minimize the electricity cost in response to a time of use pricing scheme, and to minimize the associated discomforts to the user. Resident discomforts are formulated as a deferral cost associated with a delay in meeting a load demand after it was requested, and as a temperature discomfort cost associated with the temperature deviation from the desired set-point.

For the smart home considered in this thesis, the global optimal control problem is formulated in discrete form as follows:

$$\min_{u} J(x,u,w) = \sum_{k=0}^{N-1} c_e(k)P_{Grid}(k) + c_d(k)\left[E(w_k) - u_{D,L,xEV}(k)\right] + c_t(k)\left[T_a(k) - T_{set}\right]^2 \tag{3.1a}$$

Subject to:

$$x_{k+1} = f_k(x_k, u_k, w_k) \tag{3.1b}$$

$$x_{min} \leq x_k \leq x_{max}\ \forall k = 1:N \tag{3.1c}$$

$$u_{D,L}(k) \in \{0,1\}\ \forall k = 0:N-1 \tag{3.1d}$$

$$u_{HVAC}(k) \in \{0, 0.5, 1\}\ \forall k = 0:N-1 \tag{3.1e}$$

$$u_{min} \leq u_{xEV,ES}(k) \leq u_{max}\ \forall k = 0:N-1 \tag{3.1f}$$

$$P_D(k) + P_L(k) + P_{xEV}(k) + P_{HVAC}(k) + P_{ND}(k) = P_{Grid}(k) + P_{ES}(k) + P_{Solar}(k)\ \forall k = 1:N \tag{3.1g}$$

$$P_{Grid}(k) = h(x_k, u_k, w_k) \leq P_{cap}(k)\ \forall k = 1:N \tag{3.1h}$$

$$u_{D,L,xEV}(k) = 0\ \forall k < E(w_k)\ \forall k = 0:N-1 \tag{3.1i}$$

$$u_{D,L,xEV}(k) = 0\ \forall k > D(w_k)\ \forall k = 0:N-1 \tag{3.1j}$$

$$\sum_{0}^{N-1} u_{D,L,xEV}(k) = C \tag{3.1k}$$

$$u_{L,D}(k) \leq 1 - s_{L,D}(k)\ \forall k = 0:N-1 \tag{3.1l}$$

$$u_{L,D}(k-1) - u_{L,D}(k) \leq 1 - s_{L,D}(k)\ \forall k = 1:N-1 \tag{3.1m}$$

$$s_{L,D}(k) \leq s_{L,D}(k-1)\ \forall k = 1:N-1 \tag{3.1n}$$

In equation (3.1), the objective function $J(x,u,w)$ depends on the state vector x, the control vector u, and the external inputs vector w. The objective is evaluated

over N time steps of duration Δt and the total simulation time is given by $T_{end} = N \cdot \Delta t$ which in simulations conducted for this thesis was typically 1 month. Under the time of use pricing scheme, the electricity price is defined at time step k as $c_e(k)$, and $P_{Grid}(k)$ denotes the total power demanded from the grid by the smart home at that time step. The smart home operates the HVAC to minimize the deviation of the household temperature T_a from a desired set-point temperature of T_{set}, and the squared temperature deviation is penalized by a cost $c_t(k)$, a discrete parameter. The deferral cost $c_d(k)$ penalizes the delay in activation of an appliance after it was requested by the user. The user-defined activation of deferrable appliances is denoted by $E(w_k)$ while $D(w_k)$ is the associated deadline for completion, and C is the required time of activation associated with each deferrable appliance before completion. The costs $c_d(k)$ and $c_t(k)$ are discrete, tunable parameters and can be chosen by the resident based on their tolerance of the associated discomfort. For example, a large value of c_d results in a HEM strategy solution that prioritizes earlier activation of requested appliances. In this thesis, both $c_d(k)$ and $c_t(k)$ are constant and pre-defined.

The system is subject to the state dynamics and state constraints 3.1b and 3.1c, respectively. The input constraints are given in 3.1d, 3.1e, and 3.1f. The power balance equation must always be satisfied such that the demand of power is equal to the supply which is enforced by 3.1g. Moreover, a power capping constraint is considered such the total power demanded from the grid is always below a maximum allowable value and is enforced by 3.1h. The appliances and vehicle charging cannot be activated before the user enabling time $E(w_k)$ and each user request must also be completed before a certain deadline, $D(w_k)$, as described in constraints

3.1i and 3.1j respectively. Also, each appliance must be activated for a specified number of time steps C to allow for completion, as described in constraint 3.1k. Finally, the laundry and dishwasher operation cannot be interrupted once operation begins. This constraint is implemented using a slack variable in 3.1l, 3.1m, and 3.1n as shown in [71].

The state, control, and external input vectors (whose components were introduced in Sections 2.1.1-2.1.5) are defined in Equation 3.2 and the related constraints of the optimal control problem are summarized in Table 3.1.

$$x_k = [T_a(k), SOC_{xEV}(k), SOC_{ES}(k)]^T \tag{3.2a}$$

$$u_k = [u_{HVAC}(k), u_{xEV}(k), u_D(k), u_L(k), u_{ES}(k)]^T \tag{3.2b}$$

$$w_k = \left[T_\infty(k), P_{ND}(k), SOC_{xEV,0}(k), P_{Solar}(k)\right]^T \tag{3.2c}$$

Table 3.1: Optimal Control Problem Constraint Values

Parameter	**Minimum**	**Maximum**	**Value**
T_{ref}	-	-	$20°C$
$T_{set,winter}$	-	-	$22°C$
$T_{set,summer}$	-	-	$18°C$
$T_{a,winter}$	$21°C$	$23°C$	-
$T_{a,summer}$	$17°C$	$19°C$	-
SOC_{xEV}	20%	80%	-
SOC_{ES}	20%	80%	-
u_{xEV}	0 Amps	$2.5 \cdot N_{xEV,s}$ Amps	
u_{ES}	0 Amps	$2.5 \cdot N_{ES,s}$ Amps	-
P_{cap}	-	-	14 kW

3.2 Sequential Model Predictive Control for Load Coordination

The optimization problem defined in Section 3.1 is defined for the entire simulation period, which becomes intractable for real-time implementation with large T_{end}. Additionally, it is desired to ensure fast computation speed in light of an extensive simulation campaign to be conducted. Moreover, the external input vector w which is dependent on user activities and environmental conditions, is typically updated in real-time, and is not known before-hand for the entire duration of simulation. Therefore, for real-time implementation, a model predictive control (MPC) scheme is used to solve the optimization problem over a shorter control horizon $T_H < T_{end}$. At each time step, the first control action obtained after optimization is applied to update the plant model states for the next time step. Simultaneously, the external input w is also updated based on new user activities and updated environmental temperature and photovoltaic power. With the new states and external inputs, the optimization problem is solved again by shifting the time horizon forward by one time step. As the simulation approaches T_{end}, specifically when $T(k) + T_H > T_{end}$, the time horizon will shrink such that the simulation will not exceed the final simulation time and all the activities are completed within the simulation time. The receding horizon is defined in 3.3 where $T_{H,Rec}$ is the updated horizon length near the end of simulation. This process is continued until the end of the simulation when $T(k) = T_{end}$. The integration in the smart home plant model is shown in Figure 3.1 and the parameters for the MPC is shown in Table 3.2 in which the prediction horizon is the same length as the horizon.

$$T_{H,Rec} = \begin{cases} T_{end} - T(k), & T(k) + T_H > T_{end} \end{cases} \tag{3.3}$$

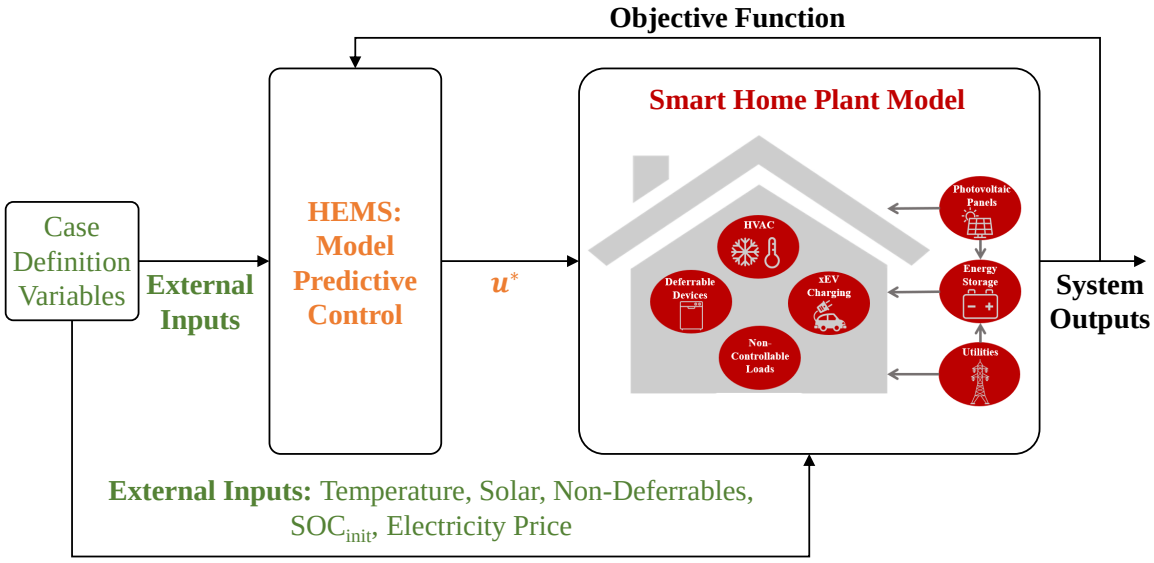

Figure 3.1: Block Diagram of Model Predictive Control Implemented on Home Plant Model

Table 3.2: Model Predictive Control Parameters

Parameter	**Description**	**Value**
T_H	Horizon Length	8 Hours
Δt	Time Step	10 Minutes
c_d	Weight for Deferral Time Cost	1e-9
$c_{t,summer}$	Summer Weight for Temp. Discomfort Cost	1e-5
$c_{t,winter}$	Winter Weight for Temp. Discomfort Cost	1e-10

Because of the nonlinearities in the system dynamics, integer and continuous control variables, and the large number of states and control inputs, solving the optimal control problem in Section 3.1 even for a shorter horizon T_H is computationally expensive for real-time implementation [31]. For this reason, a sequential

MPC scheme is proposed here that breaks the optimization problem of each control horizon into smaller subproblems in order to achieve real-time performance.

The original optimization problem is partitioned into three sub-optimization problems: (1) HVAC and energy storage; (2) vehicle charging and energy storage; (3) laundry, dishwasher and energy storage. In this sequential MPC scheme, the HVAC and energy storage subproblem is solved first, because HVAC control is required at every time-step irrespective of other user requests. The next subproblem solved is the optimization of the vehicle charging and energy storage which is optimized before laundry and dishwasher machines because vehicle plug-in occurs more frequently than user requests of laundry and dishwasher machines. The scheduling of laundry and dishwashing can be solved together due to the similar constraints and input variable types related only to the time of completion.

In this sequential MPC, the energy storage system can adjust the amount of free energy available to the other controllable appliances, thereby affecting their scheduling. For this reason, the control of the energy storage system is considered in every subproblem, thus coupling the appliances indirectly. An additional coupling of the subproblems is related to the capping constraint defined in equation 3.1h which limits the total power demanded from the smart home. Since this capping constraint is violated infrequently, it is checked and addressed at the end of the sequence. This sequential scheme of solving the smaller problems is shown in Figure 3.2.

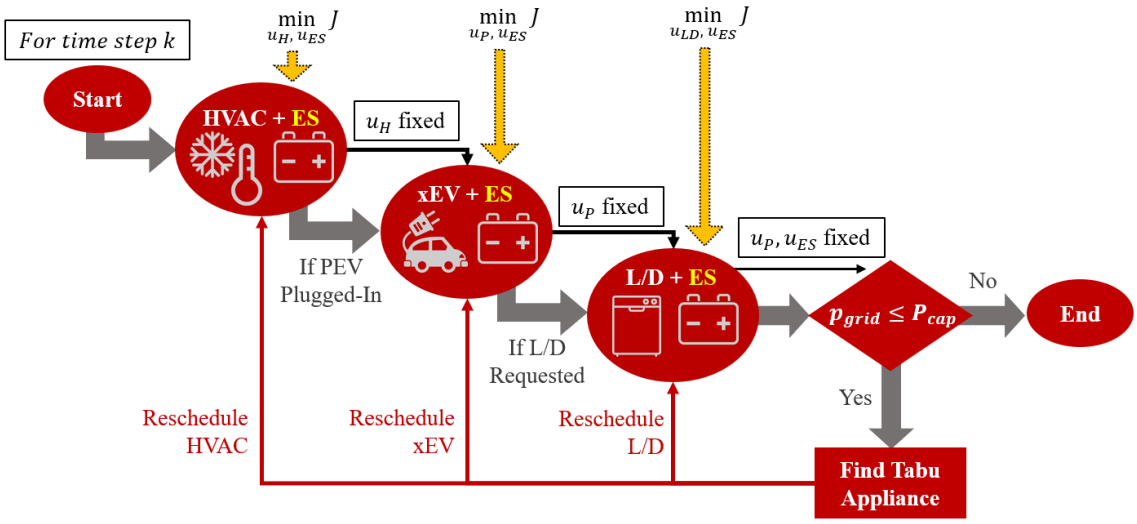

Figure 3.2: Hierarchical Optimization in HEMS at One Time Step

3.2.1 HVAC and Energy Storage Sub-Optimization Problem

The first sub-problem optimizes the operation of only the HVAC and energy storage over the time horizon $T_H < T_{end}$, corresponding to N_H time steps of duration Δt. Accordingly, the original cost function of Section 3.1 is modified to consider only the electricity cost and temperature difference from the set point, as defined in Equation 3.4a. Additionally, since the other appliance loads including xEV, laundry, and dishwasher are not considered, their respective control vectors are set to zero and the constraints are simplified, as shown in Equation (3.4). Only P_{HVAC} and P_{ND} remain in the power demands in the power balance constraint (3.4f).

$$\min_{u} J(x,u,w) = \sum_{k=0}^{N_H-1} c_e(k)P_{Grid}(k) + c_t(k)\left[T_a(k) - T_{set}\right]^2 \tag{3.4a}$$

Subject to:

$$x_{k+1} = f_k(x_k, u_k, w_k) \tag{3.4b}$$

$$x_{min} \leq x_k \leq x_{max} \ \forall k = 1 : N_H \tag{3.4c}$$

$$u_{HVAC}(k) \in \{0, 0.5, 1\} \ \forall k = 0 : N_H - 1 \tag{3.4d}$$

$$u_{min} \leq u_{ES}(k) \leq u_{max} \ \forall k = 0 : N_H - 1 \tag{3.4e}$$

$$\begin{aligned} &P_{HVAC}(k) + P_{ND}(k) \\ &\quad = P_{Grid}(k) + P_{ES}(k) + P_{Solar}(k) \ \forall k = 1 : N_H \end{aligned} \tag{3.4f}$$

Solving the above subproblem yields $u^{(1)}_{HVAC} \in \mathbb{R}^{N_H}$ and $u^{(1)}_{ES} \in \mathbb{R}^{N_H}$ which are the control commands for HVAC and energy storage respectively, over the time horizon T_H. When optimizing the remaining subproblems, the command of HVAC is held constant at the control command $u^{(1)}_{HVAC}$ associated with a power demand of $P^{(1)}_{HVAC} \in \mathbb{R}^{N_H}$.

3.2.2 Vehicle Charging and Energy Storage Sub-Optimization Problem

After the optimization of the first subproblem, if the xEV is plugged in, the sequential MPC optimizes the deferrable scheduling of the xEV charging, alongside the energy storage operation. The HVAC command is fixed at $u^{(1)}_{HVAC}$ and thus has no influence on the cost function. As a result, the objective function in the second subproblem optimization is updated to replace the temperature discomfort cost by the appliance delay discomfort cost. Similar to the previous subproblem, the input commands for the remaining appliances of laundry and dishwasher are set to zeros in this subproblem. The constraints of the second optimization subproblem are also updated, as indicated in Equation (3.5). The power balance constraint (3.5h) now features $P_{xEV}(k)$ and the previously obtained, $P^{(1)}_{HVAC}$ and $P_{ND}(k)$.

$$\min_{u} J(x,u,w) = \sum_{k=0}^{N_H-1} c_e(k)P_{Grid}(k) + c_d(k)\left[E(w_k) - u_{xEV}(k)\right] \tag{3.5a}$$

Subject to:

$$x_{k+1} = f_k(x_k, u_k, w_k) \tag{3.5b}$$

$$x_{min} \leq x_k \leq x_{max}\ \forall k = 1 : N_H \tag{3.5c}$$

$$u_{min} \leq u_{xEV,ES}(k) \leq u_{max}\ \forall k = 0 : N_H - 1 \tag{3.5d}$$

$$\begin{aligned} &P_{xEV}(k) + P^{(1)}_{HVAC}(k) + P_{ND}(k) \\ &\quad = P_{Grid}(k) + P_{ES}(k) + P_{Solar}(k)\ \forall k = 1 : N_H \end{aligned} \tag{3.5e}$$

$$u_{xEV}(k) = 0\ \forall k < E(w_k)\ \forall k = 0 : N - 1 \tag{3.5f}$$

$$u_{xEV}(k) = 0\ \forall k > D(w_k)\ \forall k = 0 : N - 1 \tag{3.5g}$$

$$\sum_{0}^{N_H-1} u_{xEV}(k) = C \tag{3.5h}$$

This subproblem optimization outputs the optimal control command for xEV, denoted by $u^{(2)}_{xEV} \in \mathbb{R}^{N_H}$ and energy storage $u^{(2)}_{ES} \in \mathbb{R}^{N_H}$ that minimizes the corresponding objective function in (3.5) in time horizon T_H.

3.2.3 Laundry, Dishwasher, and Energy Storage Sub-Optimization Problem

If a laundry or dishwashing request was raised by the user, the sequential MPC optimizes their deferrable scheduling alongside the energy storage operation. When optimizing this subproblem, the control commands of HVAC and xEV are held constant at the commands $u^{(1)}_{HVAC}$ and $u^{(2)}_{xEV}$, obtained from subproblems (3.4) and (3.5) respectively. Compared with the objective function in (3.5a), the delay discomfort cost is quantified due to the deferrable operations of laundry and

dishwasher $u_{D,L}(k)$ rather than that caused by xEV $u_{xEV}(k)$. Due to the fixed commands for HVAC and xEV, the power balance constraint in (3.6f) is also updated to include HVAC power $P^{(1)}_{HVAC}$ and xEV charging power $P^{(2)}_{xEV}$.

$$\min_{u} J(x,u,w) = \sum_{k=0}^{N_H-1} c_e(k)P_{Grid}(k) + c_d(k)\left[E(w_k) - u_{D,L}(k)\right] \tag{3.6a}$$

Subject to:

$$x_{k+1} = f_k(x_k, u_k, w_k) \tag{3.6b}$$

$$x_{min} \leq x_k \leq x_{max}\ \forall k = 1 : N_H \tag{3.6c}$$

$$u_{D,L}(k) \in \{0,1\}\ \forall k = 0 : N_H - 1 \tag{3.6d}$$

$$u_{min} \leq u_{ES}(k) \leq u_{max}\ \forall k = 0 : N_H - 1 \tag{3.6e}$$

$$\begin{aligned} &P_D(k) + P_L(k) + P^{(2)}_{xEV}(k) + P^{(1)}_{HVAC}(k) + P_{ND}(k) \\ &\quad = P_{Grid}(k) + P_{ES}(k) + P_{Solar}(k)\ \forall k = 1 : N_H \end{aligned} \tag{3.6f}$$

$$u_{D,L}(k) = 0\ \forall k < E(w_k)\ \forall k = 0 : N_H - 1 \tag{3.6g}$$

$$u_{D,L}(k) = 0\ \forall k > D(w_k)\ \forall k = 0 : N_H - 1 \tag{3.6h}$$

$$\sum_{0}^{N_H-1} u_{D,L}(k) = C \tag{3.6i}$$

$$u_{L,D}(k) \leq 1 - s_{L,D}(k)\ \forall k = 0 : N_H - 1 \tag{3.6j}$$

$$u_{L,D}(k-1) - u_{L,D}(k) \leq 1 - s_{L,D}(k)\ \forall k = 1 : N_H - 1 \tag{3.6k}$$

$$s_{L,D}(k) \leq s_{L,D}(k-1)\ \forall k = 1 : N_H - 1 \tag{3.6l}$$

The optimization in this subproblem yields optimal control commands for laundry $u^{(3)}_L \in \mathbb{R}^{N_H}$, dishwasher $u^{(3)}_D \in \mathbb{R}^{N_H}$, and energy storage $u^{(3)}_{ES} \in \mathbb{R}^{N_H}$ that minimize the objective function (3.6a) within time horizon T_H.

3.2.4 Power Capping Check

After solving all the above subproblems, the total power consumption associated with the optimized control commands for HVAC $u^{(1)}_{HVAC}$, vehicle charging $u^{(2)}_{xEV}$, laundry $u^{(3)}_{L}$, dishwasher $u^{(3)}_{D}$ and energy storage $u^{(3)}_{ES}$ are checked to see if the capping constraint is violated, as shown in Equation (3.7). The power of laundry, dishwasher, and energy storage under the optimal commands are denoted as constant vectors $P^{(3)}_{L} \in \mathbb{R}^{N_H}$, $P^{(3)}_{D} \in \mathbb{R}^{N_H}$, and $P^{(3)}_{ES} \in \mathbb{R}^{N_H}$.

$$\begin{aligned} &P^{(3)}_{D}(k) + P^{(3)}_{L}(k) + P^{(2)}_{xEV}(k) + P^{(1)}_{HVAC}(k) + P_{ND}(k) \\ &\quad = P_{Grid}(k) + P^{(3)}_{ES}(k) + P_{Solar}(k) \ \forall k = 1 : N_H \end{aligned} \tag{3.7a}$$

$$P_{Grid}(k) \leq P_{cap}(k) \ \forall k = 1 : N_H \tag{3.7b}$$

If the constraint is not satisfied, the algorithm finds the appliance with largest power consumption at the time steps when the capping constraint is violated. This appliance is referred to as the Tabu Appliance in Figure 3.2 and is restricted from being turned on at those time steps. The associated subproblem of that appliance is solved again with this restriction to find a solution that does not violate the capping constraint. When the constraint is satisfied, the control commands of the first time horizon are finalized and denoted by $\{u^*_{HVAC},\ u^*_{xEV},\ u^*_{L},\ u^*_{D},\ u^*_{ES}\} \in \mathbb{R}^{N_H}$

The first control command of each appliance, at time step $k = 0$ is implemented in the plant model to update the system states x for the next time step optimization. Simultaneously, the external input vector w is updated with new user requests and environmental conditions. With the updated states and external inputs, the optimization problem is solved again by shifting the time horizon forward by one time step as shown in Figure 3.1, and this is repeated until the end of the simulation, T_{end}.

3.3 Optimization via Genetic Algorithm

As described in Section 1.2.2, meta-heuristic methods have been successfully applied in online demand side management for multiple objectives including reduction of residential electric power demand and power peak to average ratio, minimizing overload times, improving grid system stability, renewable energy source integration, and consumer discomfort reduction. Among meta-heuristic approaches, genetic algorithm was found to perform better than swarm-intelligence based approaches [72–74]. Further, by tuning the genetic algorithm parameters related to convergence, mutation and crossover rates, both computational time associated with the evolutionary procedures and likelihood of pre-mature convergence can be reduced [75].

In this work, a genetic algorithm is applied in each decentralized subproblem of the HEM strategy described in Section 3.2 to output the optimal control commands of corresponding appliances. In each subproblem optimization, a population of feasible control commands is initialized in the genetic algorithm. Each individual in the initialized population represents one candidate solution to the optimization subproblem. Each individual stores the proposed appliances commands in the time horizon T_H as a chromosome. All individuals in the initial population are evaluated based on the objective function values. Based on the evaluation, some individuals are selected as parents. Among them, the individuals with even lower objective values are chosen as elite and these elite individuals are directly passed to the next population. Based on the parents, children are produced either by making random changes to a single parent that is called mutation, or combining the vector entries

of a pair of parents that is called crossover. Then, the current population is replaced with the children to form the next generation. The population evolution to the next generation is iteratively repeated until the stopping criteria is met. The sequence of the genetic algorithm implementation on the control command optimization at each time horizon is summarized in Figure 3.3.

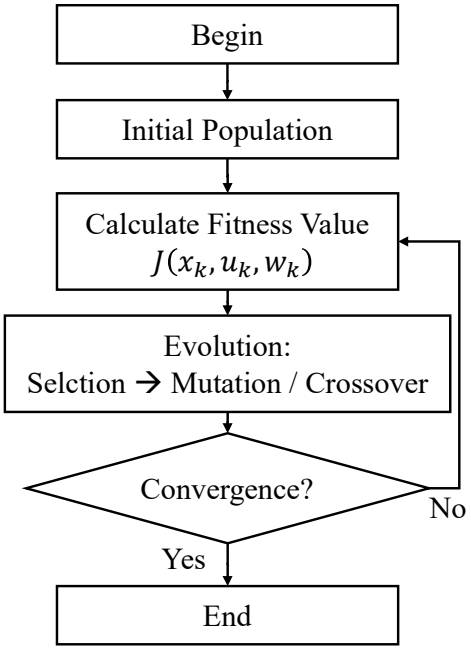

Figure 3.3: Structure of the Genetic Algorithm

In the subproblem of optimizing the operations of HVAC and energy storage in section 3.2.1, the control commands for HVAC and energy storage $u_{HVAC}(k)$ and $u_{ES}(k)$ both have a length of N_H. The individual genome in the population

directly represents the commands for the two appliances and has a length of $2N_H$. Each gene in the individual genome stores the command for the appliances at a single time step within the time horizon T_H. Next generation is repeatedly formed to achieve the minimum cost in (3.4a) until the stop criteria is met. During the generation evolution, the constraints also help to eliminate the individuals that violate the constraints. The individual genome in the last generation that has the lowest objective function value is stored and the vector entries of this individual are assigned as optimal control commands for HVAC $u^{(1)}_{HVAC}$ and energy storage $u^{(1)}_{ES}$.

In the subproblem of optimizing the operations of xEV and energy storage in section 3.2.2, the commands for xEV are optimized indirectly using the genetic algorithm. In optimizing HVAC commands, the commands are directly assigned to the individual genome and each gene in the vector entries represents a command value at one time step. However, for xEV charging commands optimization, the command activation moments are assigned to the individual genome. As shown in equation (3.8).

$$u_{xEV}(k) = \begin{cases} 1, \ \forall k \in \{k_1, k_2, \ldots, k_C\} \\ 0, \ \forall k \notin \{k_1, k_2, \ldots, k_C\} \cup k = 0 : N_H - 1 \end{cases} \tag{3.8a}$$

$$\rightarrow x_{xEV,GA} = [k_1, k_2, \ldots, k_C]^T, \ \{k_1, k_2, \ldots, k_C\} = 0 : N_H - 1 \tag{3.8b}$$

The original feasible commands for xEV $u_{xEV}(k)$ are on at C separate time steps to fully charge the vehicle, satisfying the constraints (3.5c) and (3.5h) in the original subproblem. After the interpretation, the genome $x_{xEV,GA}$ in the genetic algorithm only stores the activation moments for vehicle charging. This interpretation holds the constraints (3.5c) and (3.5h) automatically. In addition to simplifying

the constraints, this interpretation also helps to reduce the individual genome sizes in the genetic algorithm. The total length of the genome when optimizing the operations of xEV and energy storage is $N_H + C$, where C represents the number of time steps to fully charge the vehicle. After finding the optimal individual genome $x^*_{xEV,GA}$, the optimal command for xEV $u^{(2)}_{xEV}$ will be obtained by the converse interpretation shown in equation (3.8) from (3.8b) to (3.8a).

In the last subproblem optimization to output the optimal commands for laundry, dishwasher, and energy storage, the same command interpretation is applied. Due to the characteristics of laundry and dishwasher operations, the command interpretation for genetic algorithm implementation is simpler, as shown in equation (3.9).

$$u_L(k) = \begin{cases} 1, \ k = k_L : k_L + C_L - 1 \\ 0, \ k \notin \{k_L : k_L + C_L - 1\} \cup k = 0 : N_H - 1 \end{cases} \tag{3.9a}$$

$$\rightarrow x_{L,GA} = k_L, \ k_L = 0 : N_H - C_L \tag{3.9b}$$

$$u_D(k) = \begin{cases} 1, \ k = k_D + C_D - 1 \\ 0, \ k \notin \{k_L : k_D + C_D - 1\} \cup k = 0 : N_H - 1 \end{cases} \tag{3.9c}$$

$$\rightarrow x_{D,GA} = k_D, \ k_D = 0 : N_H - C_D \tag{3.9d}$$

The subproblem optimization after the interpretation also simplifies the constraints (3.6d, 3.6f-3.6j). Now the individual genome in the genetic algorithm has a length of $N_H + 2$, which is also reduced compared to the original length of the three appliances commands $3N_H$. After the optimization over the time horizon T_H is complete, a converse interpretation of the optimal individual $x^*_{L,D,GA}$ is

Table 3.3: Genetic Algorithm Settings for Sub-Optimization Problems

GA Options	HVAC		xEV	L/D
	Summer	Winter		
Maximum number of generations	500			
Maximum number of stalled generations	50			
Elite count	10	10	15	20
Objective function tolerance	0.01	0.001	0.0001	0.001
Time limit [s]	30			
Population size	100	50	250	250
Crossover fraction	0.4	0.2	0.4	0.2
Selection function	*selectionremainder*			
Crossover function	*crossoverlaplace*			
Creation function	*gacreationuniformint*			
Mutation function	*mutationpower*			

transformed to the individual optimal control commands for laundry $u_L^{(3)}$ and dishwasher $u_D^{(3)}$, separately.

For the above three different subproblems, the optimizations are all achieved using the genetic algorithm, but with different specific settings. These settings are tuned based on the specific properties of the three subproblems. The hyperparameters of the genetic algorithm are selected by tuning them systematically based on the algorithm convergence speed for each setting. The detailed hyperparameter settings for the three sub-system optimization problems are summarized in Table 3.3. Some hyperparameter settings are the same for all sub-problems while some options vary seasonally and based on the characteristics of each sub-problem.

3.4 1 Day Simulation Results

To verify the sequential optimization strategy a simulation was performed over a single day, July 1st, 2018 for a single family home in Columbus, Ohio. The model parameters and settings are summarized in Table 3.4. For this simulation, it is assumed that the energy storage system is installed inside the house, hence its temperature is the same as the temperature of the house.

Table 3.4: 1 Day Simulation: Smart Home Plant Model Parameters

Case	**Location**	**House Size [ft^2]**	**xEV Battery [kWh]**	**ES Battery [kWh]**	**ES Temp. Controlled**
1	Columbus	1606	60	14	Yes

A three-tier, time of use pricing scheme was considered where the price is highest from 12:00pm to 6:00pm and lowest throughout the night from 9:30pm to 8:30am, as shown in Figure 3.4.

The performance of the HEM strategy is compared against the baseline controller using basic performance metrics, namely the grid electricity cost; the appliance delay, which is the time difference between the expected time of completion and actual completion due to load deferral; and the temperature discomfort, which is the root mean squared error between the actual house temperature and the user-set temperature point.

For the 1 day simulation study, the associated metrics are summarized in Table 3.5. The deployment of the HEM strategy results in a 7% cost reduction compared to the baseline controller. This is accomplished by scheduling appliance operation

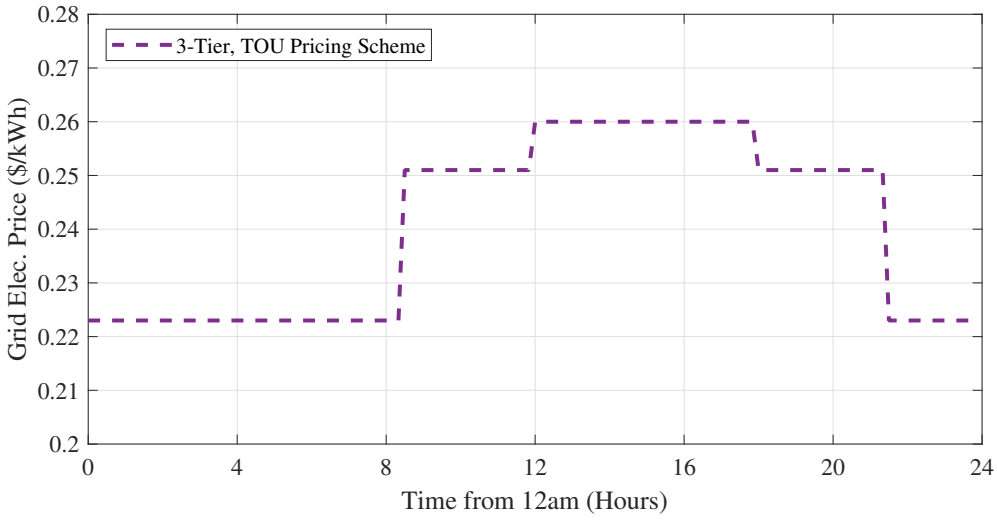

Figure 3.4: 3-Tier Time of Use Utility Pricing Scheme

during low electricity cost periods, which results in a total appliance delay 1.67 hours. The scheduling of the smart appliances is shown in Figures 3.5c and 3.5d. In addition to a reduced cost, the HEM strategy achieved a 47% improvement in lower temperature discomfort compared to the baseline controller due to the benefits obtained from the model predictive approach. The control command for the HVAC system is shown in 3.5b, while the resulting home temperature is shown in 3.5a.

Table 3.5: 1 Day Simulation: Summary of Performance Metrics

Case	**Controller Type**	**Grid Cost [$ USD]**	**Appliance Delay [Hours]**	**Temperature Discomfort [°C]**
1	*Baseline*	6.60	NA	0.68
	HEMS	6.12	1.67	0.36

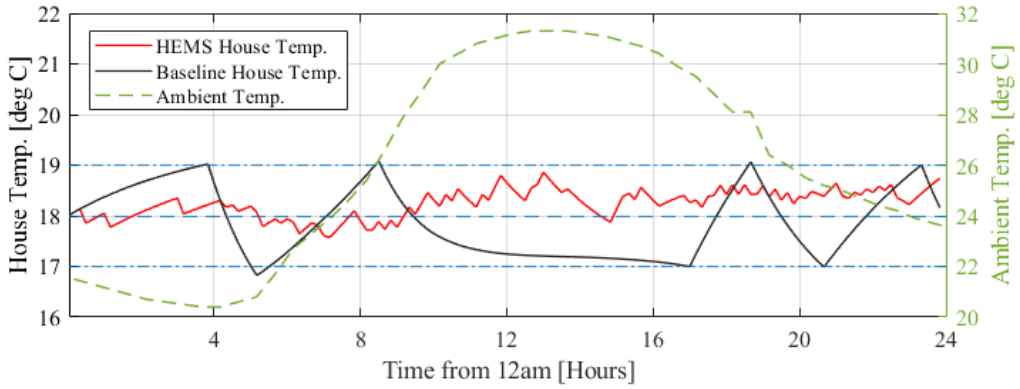

(a) House Temperature

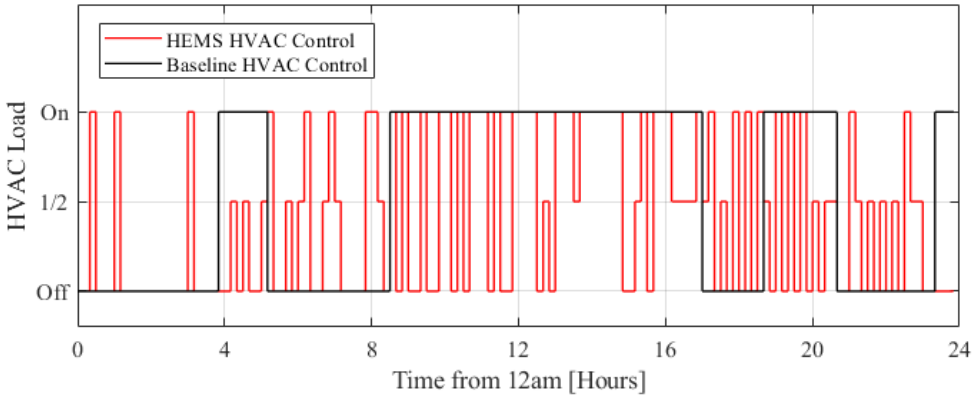

(b) HVAC Load

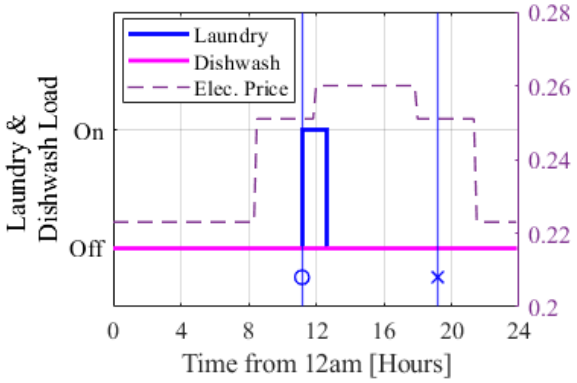

(c) Appliance Command

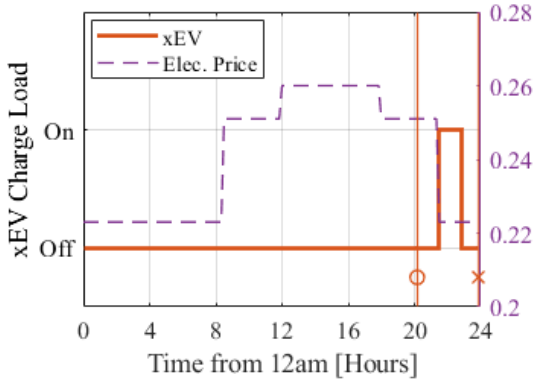

(d) xEV Command

Figure 3.5: 1 Day Sample Results - Appliance Control: 'O' Request Time, 'X' Completion Deadline

An additional comparison of the operation between the HEM strategy and the baseline controller is conducted based on the cumulative power from the grid. As sown in Figure 3.6a, for much of the high electricity price region, the HEM controller is able to defer loads to lower price regions. Figure 3.6b shows the state of charge of the battery for each control strategy. The HEM controller charges the battery during lower price regions, such that power requests during peak electricity price times don't require purchasing from the grid. Conversely, the baseline controller only charges the battery if surplus solar generation is available, and utilizes stored energy immediately after. Therefore, the HEM strategy resulted in a higher utilization of the energy storage system, as shown in Figure 3.6b. It should be noted that the energy storage begins and ends at the same state of charge for both the baseline and HEM controller; therefore, there is never excess stored energy at the end of simulation. In the case of the HEM controller, this is due to the fact that energy storage power is practically cost-free and results in an optimal control of energy storage discharge at the end of each time horizon. If this were not true, a terminal cost should be considered for the final energy storage state of charge to make a fair comparison between the baseline and HEM controller.

Finally, the power balance for both, supply and demand side is analyzed and shown in Figures 3.7 for the baseline controller and 3.8 for the HEM strategy. Negative power represents supplied and generated power, such as power from the grid and solar; while positive power corresponds to a demand. It is worth noting that at any point in time, the power supply matches the demand. The cost benefits from the HEM strategy are obtained by shifting deferrable loads from high electricity cost times to lower price times. This is particularly evident when comparing

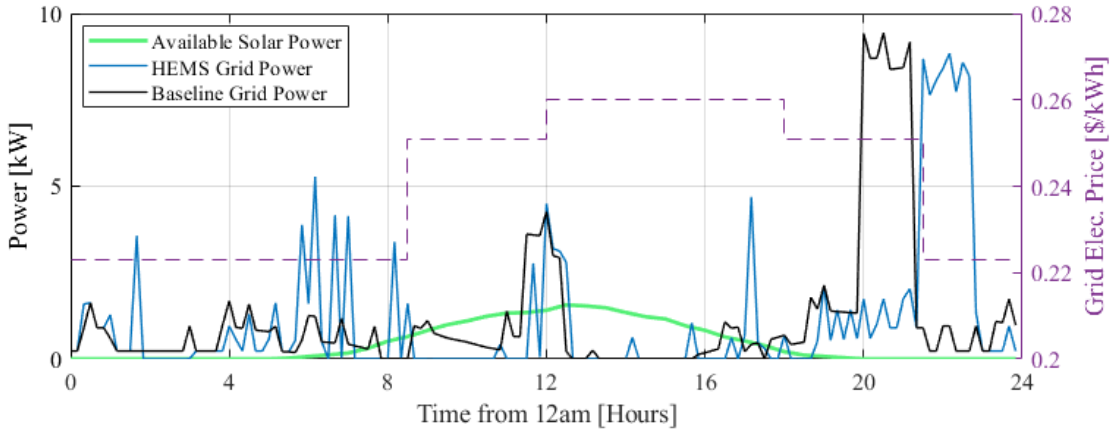

(a) Power Balance

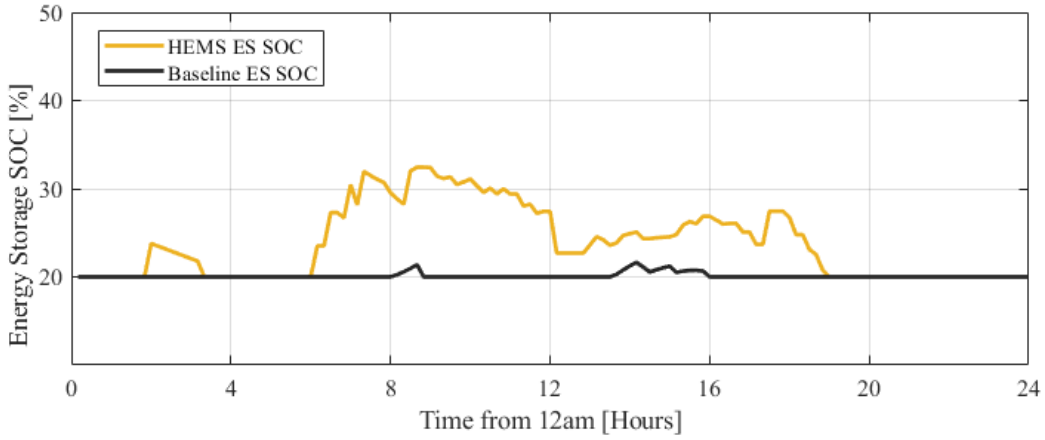

(b) ES State of Charge

Figure 3.6: 1 Day Sample Results: Power balance and state of charge comparison

the timing of the large evening power drawn for both the HEM strategy and the baseline controller.

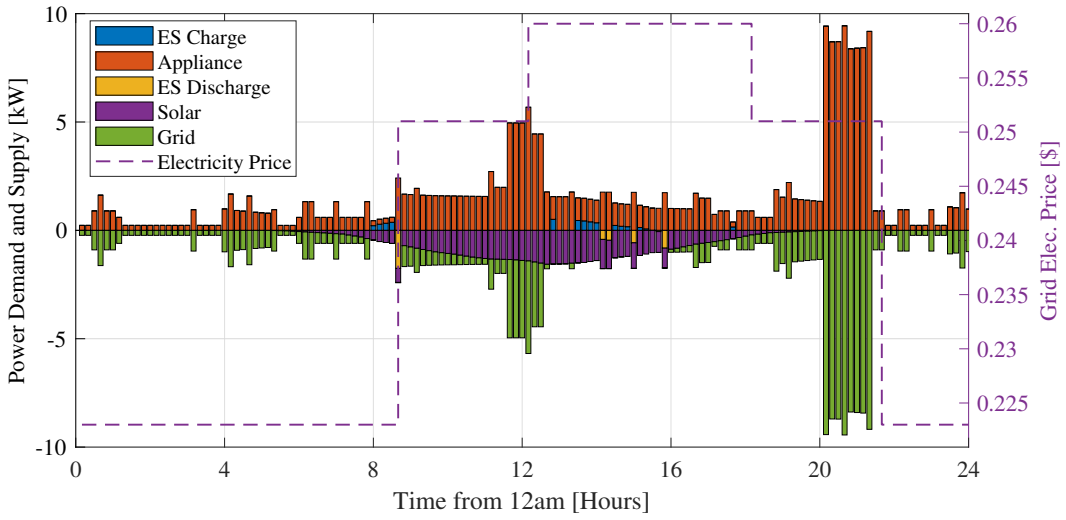

Figure 3.7: 1 Day Sample Results: Baseline Power Supply and Demand

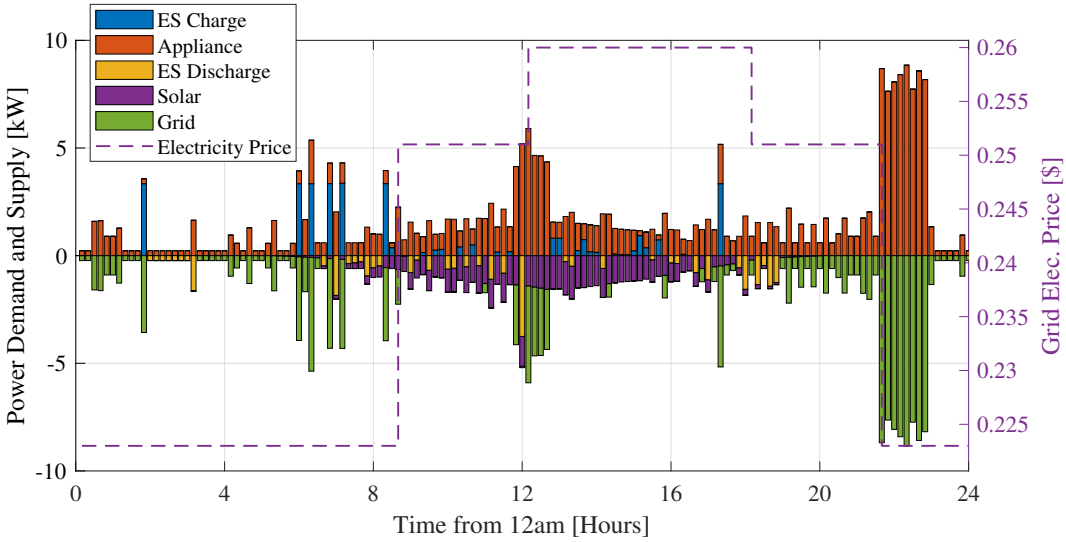

Figure 3.8: 1 Day Sample Results: HEMS Power Supply and Demand

3.5 Simulation Campaign

An extensive simulation campaign was conducted to quantify the effect of location, house size, electric vehicle battery size, and energy storage battery size on the HEM strategy performance. Overall, 12 case studies are simulated over 1 year each, such that the effect of seasonality is also captured. A summary of the parameters for the batch simulation is shown in Table 3.6.

Table 3.6: Case Studies Summary - Plant Model Settings

Case	Location	House Size (ft^2)	xEV Battery Size (kWh)	ES Battery Size (kWh)	ES Temp. Control
1	Columbus	1500-2500	60	14	Yes
2	Columbus	***500-1500***	60	14	Yes
3		***2500-3500***		14	
4		***3500-4500***		28	
5	***Los Angeles***	1500-2500	60	14	Yes
6	***San Antonio***				
7	***Boston***				
8	Columbus	1500-2500	***25***	14	Yes
9			***100***		
10	Columbus	2500-3500	60	***28***	Yes
11		3500-4500		***14***	
12	Columbus	1500-2500	60	14	No

The simulation campaign results are analyzed based on the metrics shown in Figure 3.10, which are an extension to the ones used for the one day simulation.

First, cumulative metrics have been defined to evaluate the benefits of a HEM strategy for the end user. Specifically, the total electricity cost is considered, while for customer acceptability, a temperature discomfort metric and an appliance delay metric are calculated. This comparison will provide an insight on the trade off

between energy cost savings and discomfort that is achieved with the load optimization strategy.

Because the cost savings obtained by the smart home system is dependent on the type of pricing scheme, the total deferrable power, and the relative price of the different tiers, a metric related to the total deferred power is introduced to evaluate the ability of the HEM strategy to defer loads from their expected activation window. Additionally, to understand the performance of the management strategy to shift specific appliance loads, the same metric will be quantified for each appliance. An example of dishwasher deferral is shown in Figure 3.9 to illustrate how this metric is obtained, where P_{Def} is the total power needed to complete the operation and $P_{Def,actual}$ is the total power deferred past the expected completion time.

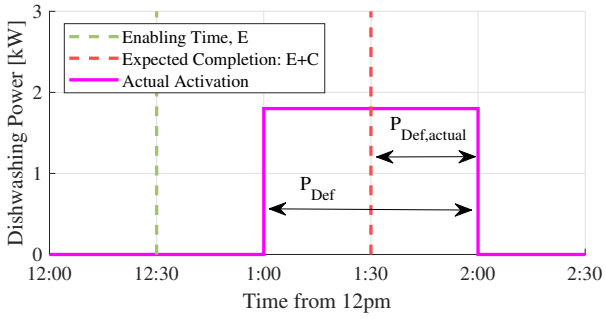

Figure 3.9: Example Dishwasher Deferred Power

Finally, it is postulated that a large majority of the benefits in the final cost to the user are achieved by leveraging the availability of the stationary energy storage. This is accomplished by charging the battery during low pricing times, as well as

storing electricity generated by the solar instead of using it directly for meeting the instantaneous demand. To verify this hypothesis, metrics related to the power split from solar as well as the utilization of the battery are obtained. For the latter, indicators for average state of charge and current are defined.

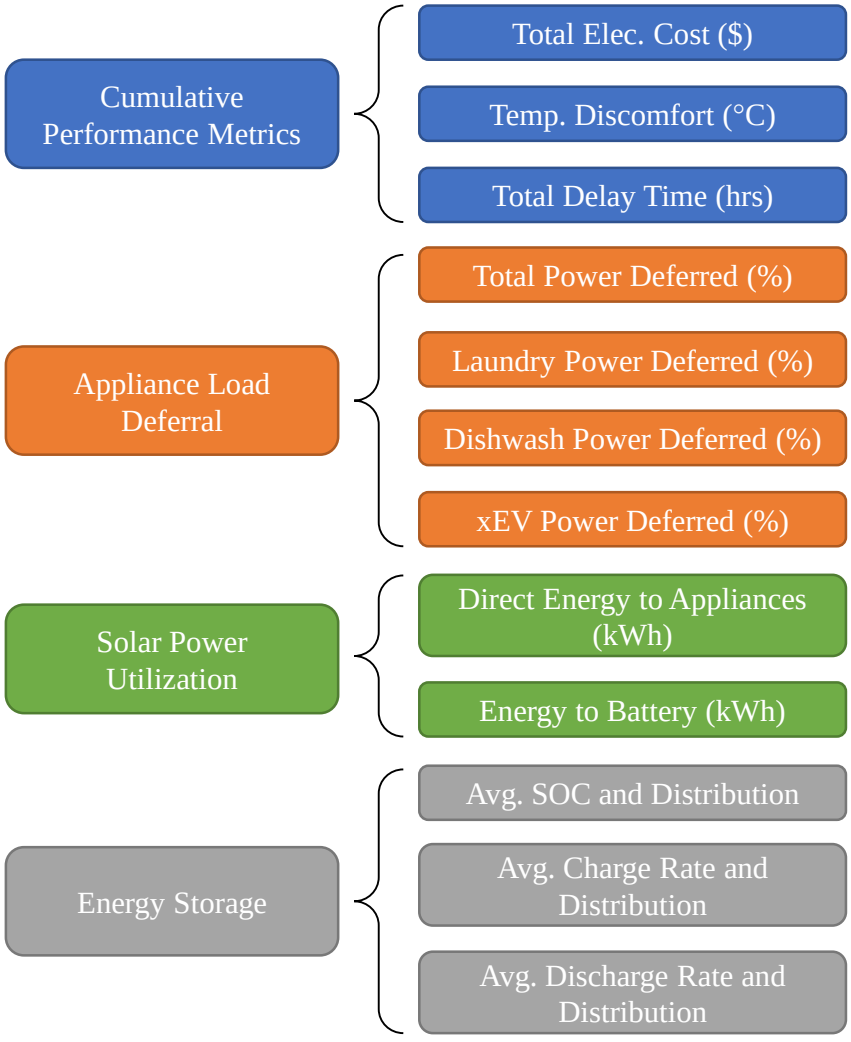

Figure 3.10: Desired Output Metrics for Simulation Campaign

3.5.1 Effect of House Size

To visualize the metrics defined in Figure 3.10, a general analysis is presented in Figure 3.12 for the cases pertaining to the effect of house size (cases 1 to 4). For the effect of house size, the average total grid cost savings of using the HEM strategy is 5.7% in place of the baseline controller. It is also observed that the total energy saving are insensitive to the house size. On the other hand, Figure 3.11a shows that the HEM strategy obtained better temperature control in smaller houses. This is due to the thermal mass of the home and its smaller time constant. When the home is smaller, the effect of external temperature is significant and an improved control strategy has a non-negligible effect on temperature tracking.

Figures 3.11b shows the total deferred power for the appliances and vehicle charging. Among every case study, the total power required for appliances and vehicle charging is almost the same; however, the total deferred power percentage decreased with house size. This can be attributed to the fact that larger house sizes require greater power to operate the HVAC.

As expected, the baseline controller uses the majority of the solar generation to meet the power demand instantaneously, while the HEM strategy includes a prediction of future demands and costs, and therefore utilizes the battery more to offset costs. This is shown in Figures 3.11c. Moreover, the higher average state of charge in the HEM strategy result shown in Figure 3.11d could be attributed to the additional power drawn from the grid when electricity cost is low. Figures for the metrics of the other effects is presented in the appendix.

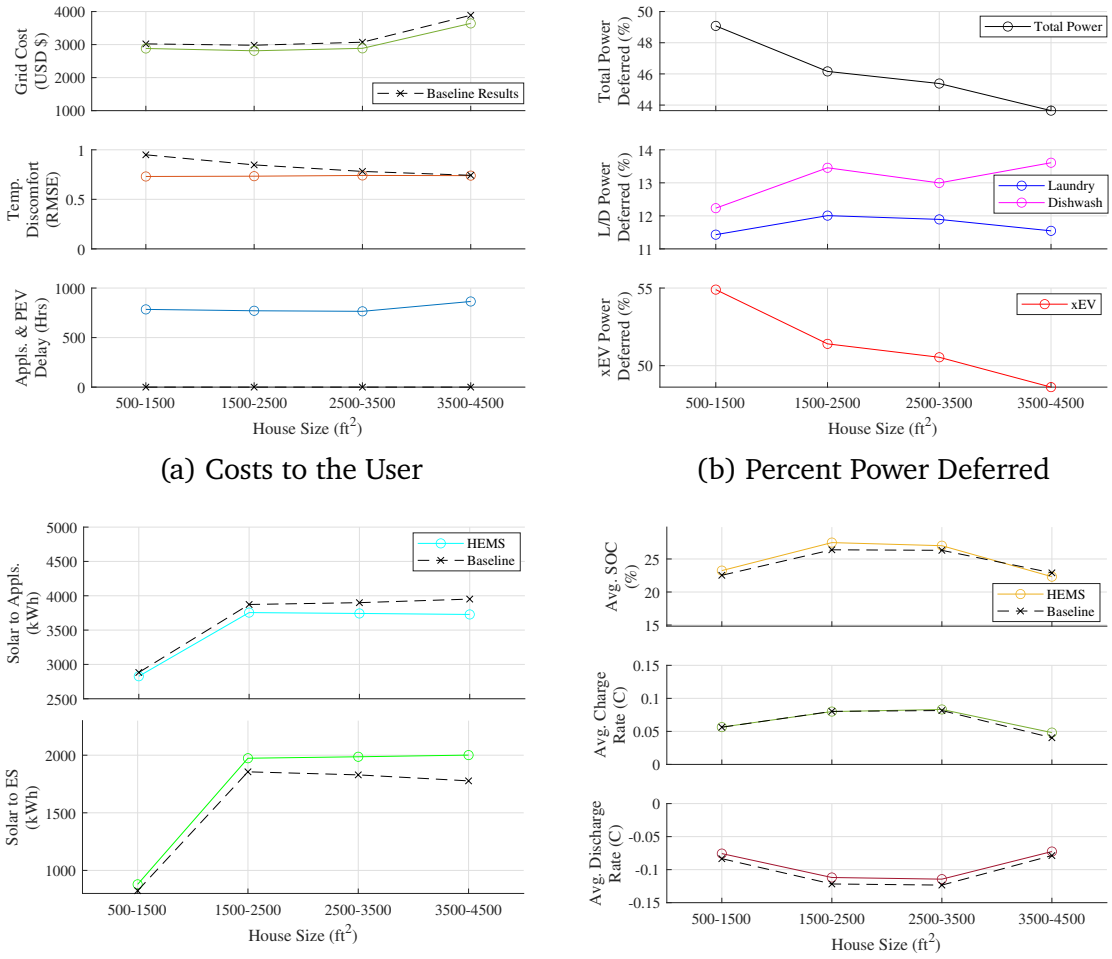

(a) Costs to the User

(b) Percent Power Deferred

(c) Solar Power Utilization

(d) Energy Storage Behavior

Figure 3.11: Effect of House Size Metrics

3.5.2 HEMS Deferral Performance

The performance of a HEM strategy can be analyzed by its effectiveness in deferring electricity loads to lower price regions. In general, the performance of the HEM strategy can be compared to the baseline controller in Figures 3.12b and 3.12a respectively for 1 month simulation period. From time 18:00 to 23:59, it is

clear that the HEM strategy tended to defer much of the load from the $0.25 price region to the lowest price region.

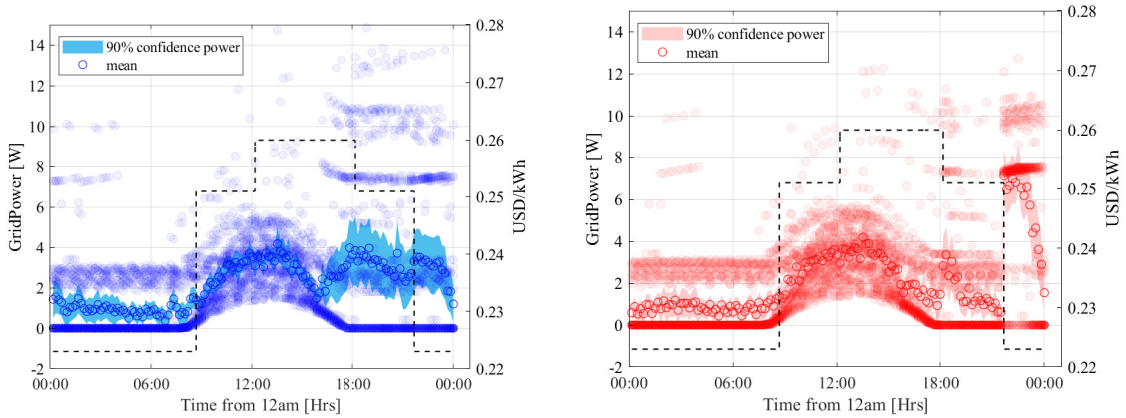

(a) Baseline (b) HEM Strategy

Figure 3.12: 1 Month Load Deferral

To quantify this effectiveness, a metric is defined as the deferral efficiency which is the percentage of the total deferrable loads that were actually deferred to lower price regions:

$$\eta_{Def} = \frac{P_{Def,actual}}{P_{Def}} \cdot 100 \tag{3.10}$$

Where P_{Def} is the total power of all of the appliance loads in the house that can be deferred and $P_{Def,actual}$ is the total amount of power actually deferred by the HEM strategy which is obtained by determining the total amount of power consumed outside of the expected activation time window $(C + E)$. The appliance loads that can be deferred are the laundry washing and drying machine, dishwasher, and vehicle charging.

Additionally, it is valuable to understand the flexibility of the home to defer power. For example, a home with a connected, smart dishwasher will be more flexible than the a home without a connected, smart dishwasher.

$$\eta_{flex} = \frac{P_{Def}}{P_{Household}} \cdot 100 \tag{3.11}$$

The home deferral flexibility and deferral efficiency were quantified to see the effects of house size and location in Figures 3.13a and 3.13b respectively. The smart home in question is quite flexible, in which over 60% of the household loads can be shifted for every case in shown. Additionally, the deferral efficiency surpassed 50% for every case shown, validating that the HEM strategy was effective. The power distribution within the four house sizes is summarized in Table 3.7.

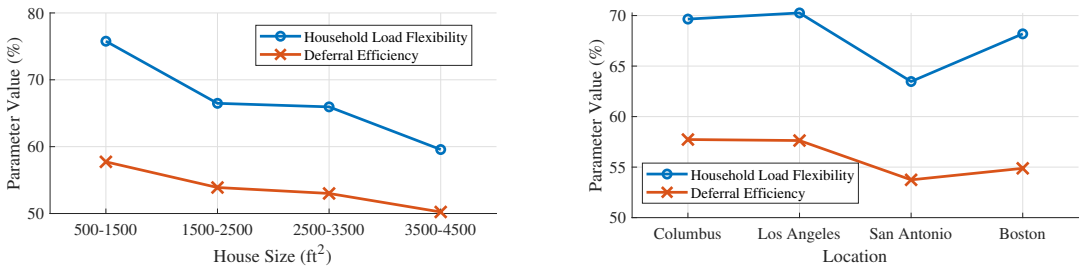

(a) Effect of House Size

(b) Effect of Location

Figure 3.13: HEM Strategy Performance

The flexibility tended to decrease with larger house sizes. This is because as house size increases, only the power required for HVAC operation increases which is not defined as a deferrable load. However, this correlation does not hold for location because the power needed for non-deferrable loads is variable between locations in addition to HVAC operation.

Table 3.7: Power [MWh] Summary for House Size Cases

House Size	**500-1500** ft^2	**1500-2500** ft^2	**2500-3500** ft^2	**3500-4500** ft^2
P_{xEV}	24.09	24.09	24.09	22.89
$P_{Laundry}$	0.49	0.49	0.49	0.49
$P_{Dishwash}$	0.20	0.20	0.20	0.20
P_{HVAC}	2.86	4.57	4.86	8.04
$P_{Act,ND}$	7.92	7.92	7.92	7.92
P_{Def}	24.77	24.77	24.77	23.58
$P_{Def,Actual}$	14.30	13.35	13.13	11.84
$P_{Household}$	32.69	37.26	37.56	39.58

Additionally, the deferral efficiency tended to decrease with larger house sizes. This is a unique result given that the deferral efficiency does not consider HVAC power in the calculation and it is known that only HVAC power varies between house size. It can be postulated that at larger house sizes the algorithm cared more about user temperature discomfort rather than grid cost savings.

3.5.3 Solar Power Utilization and Grid Cost

It was found, that in certain cases the HEM strategy was able to more efficiently utilize the solar power by leveraging the energy storage system to drive down grid cost. For example, as shown in Figure 3.14a, in San Antonio the utilization of the energy storage relative to the baseline was much greater than any other location. This utilization ensured greater cost savings relative to the baseline for the case in San Antonio as shown in Figure 3.14b. Although San Antonio did generate the most solar power, the trend to use the energy storage more is not correlated to total solar power generated.

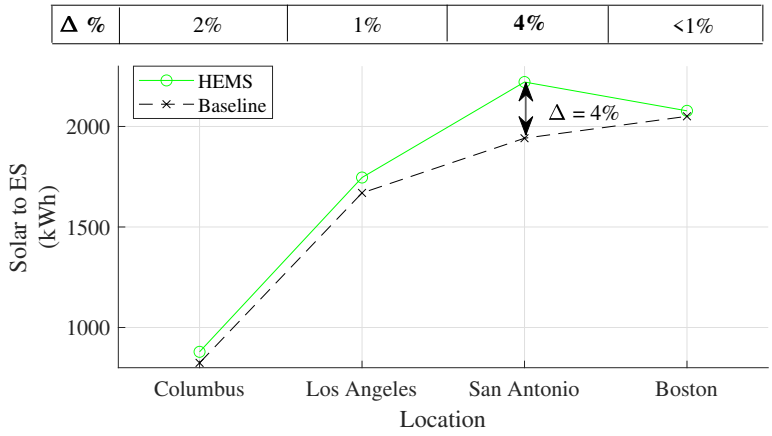

(a) Energy Storage Utilization via Solar Power

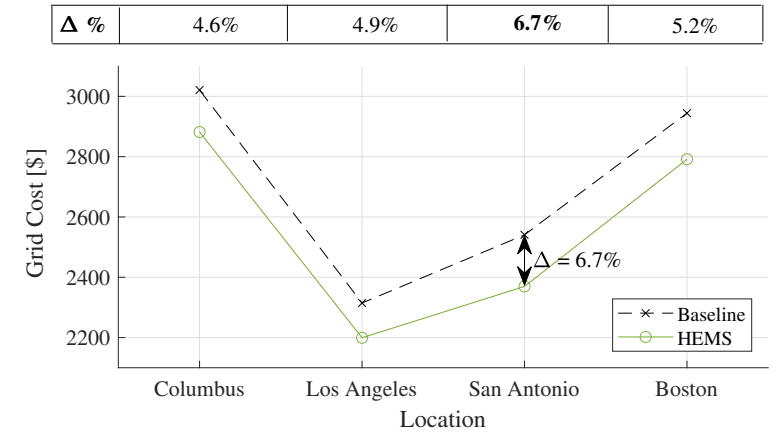

(b) Grid Savings due to Energy Storage Utilization

Figure 3.14: Solar Power Utilization and Grid Cost

3.5.4 Solar Power Utilization and Energy Storage Behavior

Conversely to the results discussed in Section 3.5.3, it was found that energy storage utilization did correlate to house size. This is demonstrated in Figure 3.15 in which the solar power dedicated to energy storage increased with house size increase.

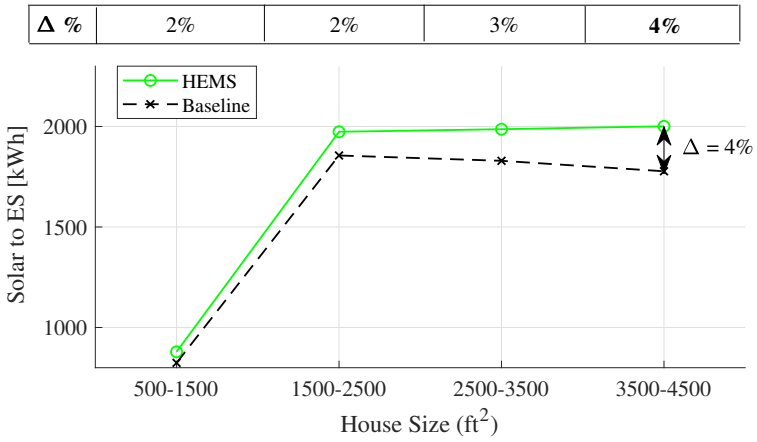

Figure 3.15: Energy Storage Utilization via Solar Power

It would be expected that with an increased utilization of the energy storage that the average state of charge of the battery would increase; however, this was not found to be true in every case. As demonstrated in Figure 3.16, for the largest house size, when the energy storage was most utilized in the four cases, the average state of charge of the battery was actually less for the HEM strategy compared to the baseline strategy.

This trend of the energy storage behavior is not intuitive at first, but by analyzing the operation of the energy storage in different cases the reason for the trend becomes clear. Figures 3.17a and 3.17b illustrates the operation of the energy storage system, via state of charge, for the a mid-sized home at 1606 square feet and the largest house size at 4252 square feet respectively for a single day.

Of course for the larger house, the average state of charge appears to be greater; however, it is also clear that for both house sizes, the frequency of charge and discharge events is greater for the HEM strategy compared to the baseline. This

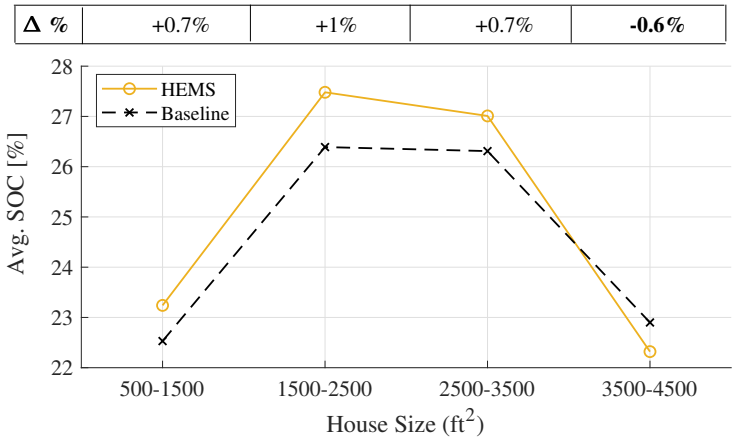

Figure 3.16: Energy Storage Average State of Charge

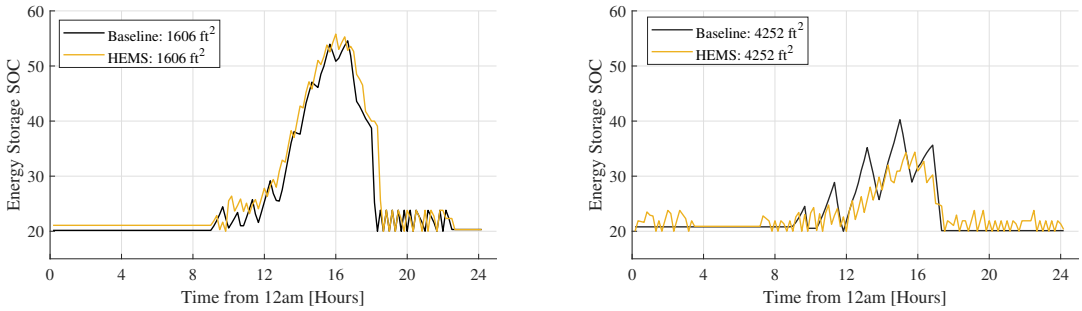

(a) 1606 ft^2 (b) 4252 ft^2

Figure 3.17: Energy Storage State of Charge

means that the overall utilization could still be greater as quantified by the total amp-hour throughput in Table 3.8.

It is understood that as the house size increase, the relative power dedicated to the HVAC operation drastically increases, as shown in Table 3.9. This will result in greater discharge events of the energy storage for larger house sizes. Additionally,

Table 3.8: Total (1-Year) Ah-Throughput

	1606 ft^2	**4252** ft^2
Baseline	385 Ah	343 Ah
HEMS	405 Ah	480 Ah
Δ %	5.2%	40%

Table 3.9: Relative HVAC Power

	HEMS		**Baseline**	
House Size	***HVAC Power***	***% of Total Power***	***HVAC Power***	***% of Total Power***
1606 ft^2	2.86 MWh	18%	3.07 MWh	19%
4252 ft^2	8.04 MWh	38%	8.73 MWh	40%

the frequency of HVAC operation is much greater for the HEM strategy compared to the baseline operation which utilizes bang-bang control as demonstrated previously in Figure 3.5a. Therefore, in this context, the trend that as house size increases, the energy storage utilization increases is understood. Additionally, it understood that does not necessarily correlate to a higher average state of charge relative to the baseline controller.

3.6 Summary

This chapter focuses on the design of the scheduling for appliances including HVAC, vehicle charging, laundry washer and dryer, dishwasher, solar generation, and energy storage. Considering a time of use pricing scheme, the HEM strategy is used to minimize grid cost to the user while also considering user discomfort via appliance deferral times and temperature differences. The general operation of the

HEM strategy was analyzed with a 1 day simulation study, and the performance was analyzed with an extensive simulation campaign.

The HEM strategy is found to be able to save approximately $160 on of the electricity cost per year relative to using the baseline controller on average for every case. Additionally, the HEM strategy tends to do a much better job of keeping the house temperature closer to the set point relative to using the bang-bang control from the Baseline controller.

Another difference found between the HEM strategy and the baseline strategy is the overall operation of the energy system. In all cases it was found that the energy storage was utilized more by the HEM strategy compared to the baseline strategy. While it is clear that the energy storage system is not used in a highly strenuous operating state in any of the cases, it is still of interest to understand the relative rates of battery degradation for operating with the HEM strategy or the baseline strategy. For example, given battery cell capacity fade is heavily dependent on battery temperature, the effect of energy storage temperature control will be of interest. This will be further investigated in the following chapter.

Chapter 4: Semi-Empirical Battery Degradation Model

Due to the complexities in both computation and calibration with limited amount of data as discussed in Chapter 1.3, in this chapter a semi-empirical battery aging model is developed to quantify the imposed capacity fade due to the HEM strategy and the baseline controller for each of the simulation campaign case studies.

4.1 Mixed-Degradation Model

4.1.1 Development of a Mixed-Degradation Model

A mixed approach was chosen to model battery aging that combines the respective benefits from the data-driven calibration approach [60] and a semi-empirical physics-based model [76, 77]. Consistently with other semi-empirical models, the proposed Mixed-Degradation Model employs physics-based equations that model two primary battery aging mechanisms, SEI layer growth and LAM [76, 77]. The equations that model these mechanisms are:

$$Q_{SEI} = \int_0^t \frac{k_{SEI} \cdot e^{-\frac{E_{SEI}}{RT_{batt}}}}{2(1+\lambda\theta)\sqrt{t}} dt \tag{4.1}$$

$$Q_{LAM} = \int_0^t k_{LAM} \cdot e^{-\frac{E_{LAM}}{RT_{batt}}} \cdot SOC \cdot |I| dt \tag{4.2}$$

$$Q_{total} = Q_{SEI} + Q_{LAM} \tag{4.3}$$

Where k_{SEI}, E_{SEI}, and λ are calibration parameters of the SEI layer growth equation, k_{LAM} and E_{LAM} are calibration parameters of the LAM equation, R is the universal gas constant, T_{batt} is the battery temperature, and θ is a parameter that captures the effects of the reaction overpotential. Finally, t is the virtual time which is the equivalent amount of time for any prior capacity fade due to SEI layer growth [55].

Except θ, which captures the effects of the reaction overpotential, all other parameters of the equations are available as constant battery characteristics, calibration parameters, or inputs from an equivalent circuit model. The parameter θ is obtained from complex electrochemical models in which partial differential equations must be solved, such as an extended single particle model [76, 77].

The proposed model differs from Equation 4.1 because, rather than solving for θ, it is instead defined as an additional calibration parameter. Given that λ in Equation 4.1, is also a calibration parameter, λ and θ are lumped as a single parameter, $\chi := \lambda \cdot \theta$. Then the equation for capacity loss due to SEI layer growth becomes:

$$Q_{SEI} = \int_0^t \frac{k_{SEI} \cdot e^{-\frac{E_{SEI}}{RT_{batt}}}}{2(1+\chi)\sqrt{t}} dt \tag{4.4}$$

The procedure to calibrate the five model parameters, k_{SEI}, E_{SEI}, χ, k_{AM}, and E_{AM} to a specific battery type follows a procedure similar to the one used in [60] for the calendar aging calibration. First, the parameters k_{SEI}, E_{SEI}, and χ in Equation 4.4 are calibrated to match experimental calendar aging data for the specific battery chemistry type by minimizing the deviation between model and experimental data. This calendar aging calibration approach relies on the assumption that χ is

only a function of state of charge (SOC) and temperature and is not dependent on C-rate. Although the C-rate does have a minimal contribution in θ which is a function of reaction overpotential; this error accumulation is negligible so this assumption is reasonable [77].

Next, χ is calibrated against additional calendar aging data sets in which the battery SOC and temperature are varied while k_{SEI} and E_{SEI} are held constant from the intial calibration step. This initial calendar aging procedure determines a map of χ as a function of battery temperatures and SOC.

The final step consists of the calibration of the parameters k_{LAM} and E_{LAM} in Equation 4.2 to match cycling aging data. Because cycling aging is also affected by calendar, and both mechanisms, SEI and LAM, are present, this calibration procedure is performed on the overall capacity fade Q_{total} defined in Equation 4.3.

In the following sections, the calibration procedure is applied to a 2.3 Ah LFP Battery (26650) from A123 [3, 4, 77].

4.1.2 Calibration of Capacity Loss Due to SEI Layer Growth

The 2.3 Ah battery model was calibrated to fit calendar aging data due to SEI layer growth given in [3, 4], and the resulting parameters are shown in Table 4.1. The SEI layer growth coefficients are then held constant and used during the calibration of χ at four additional operating conditions against calendar aging data from [3, 4, 77]. The results of the χ calibration at each operating condition is summarized in Table 4.2 and shown in Figure 4.1. The values of χ not given in the

Table 4.1: Q_{SEI} Model Coefficients for the A123 LFP Battery

Parameters	Value	Unit
k_{SEI}	7,350	$1/sec^{1/2}$
E_{SEI}	39,330	J/mol

Table 4.2: Values of χ at Various Operating Points for the A123 LFP Battery

$SOC(\%)/T°C$	$25°C$	$30°C$	$45°C$	$60°C$
30%	-	1.6227	1.0331	-
50%	0.6970	-	0.2841	-
100%	0.0482	-	0.0331	0.0101

table, but denoted with an 'X' in Figure 4.1 were obtained using a natural neighbor, linear extrapolation. Next, a cubic surface fit was plotted over the original data points in the plot.

To demonstrate the fitness of Equation 4.4 after the calibration, Figure 4.2 below displays the experimental and model's capacity loss due to SEI layer growth for five of the calibration sets.

The agreement of the calibrated model with the calibration data set is shown in Figure 4.2. The model shows very good fit in relation to the experimental data; however, towards the beginning of the data set the model tends to over-predict the calendar aging and towards the end of the data set the model tends to under-predict calendar aging.

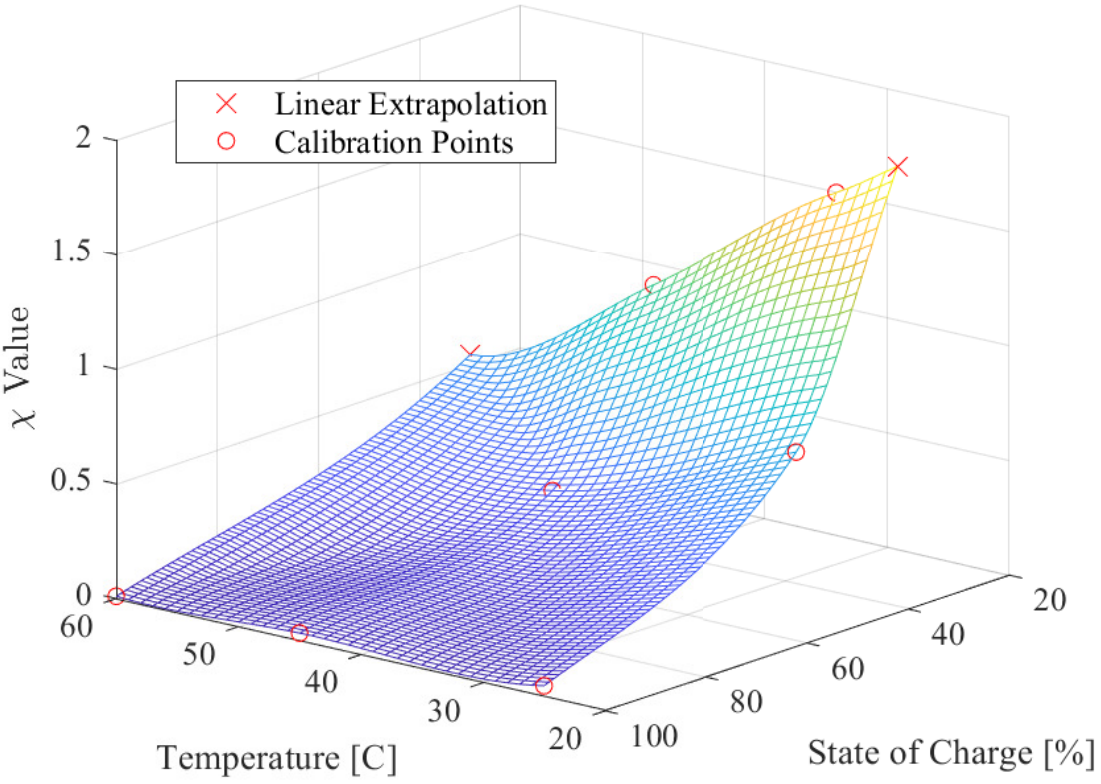

Figure 4.1: Mapping of χ as a Function of Temperature and State of Charge

4.1.3 Calibration of Capacity Loss Due to LAM

Finally, k_{LAM} and E_{LAM} are calibrated using experimental cycling aging data from [4].

This experimental data set was collected by imposing a synthesized current profile to the battery that mimics a Hybrid Electric Vehicle duty cycle shown in Figure 4.3. While the variation in state of charge is minimal, as in the case of a charge sustaining vehicle, the data contains a large variation in C-rate. The values of the model coefficients after the calibration are summarized in Table 4.3.

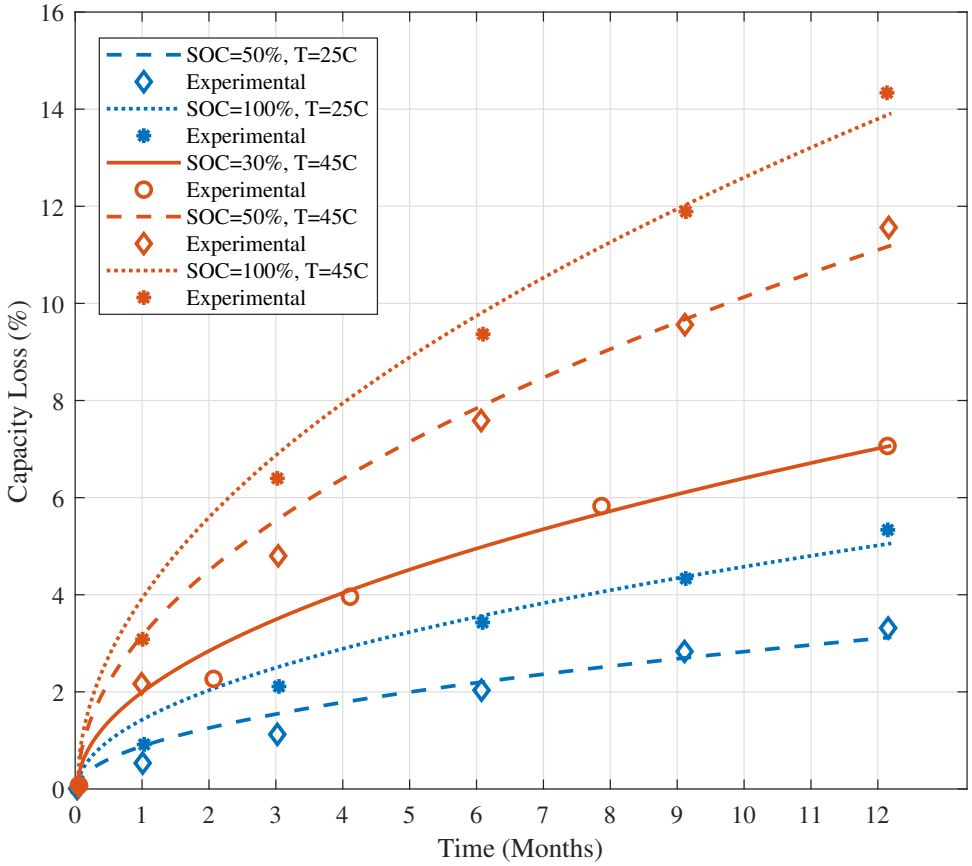

Figure 4.2: Comparison of the Capacity Loss Due to SEI Layer Growth Obtained with the Calibrated Model Against Experimental Data from [3, 4]

A verification of the complete and calibrated model is shown in Figure 4.4 for the calibration set. The results show a great fit between model and experimental data; however, there seems to be a slight under-prediction of capacity fade at the start of the experimental data.

Table 4.3: Q_{LAM} Model Coefficients for the A123 LFP Battery

Parameters	Value	Unit
k_{LAM}	1.1798	$1/Ah$
E_{LAM}	39,111	J/mol

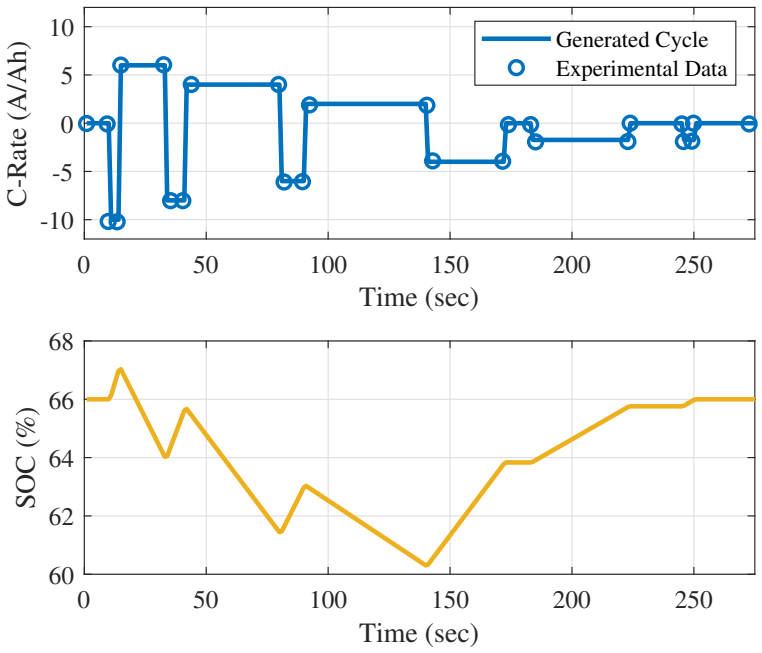

Figure 4.3: Synthesized Current Profile and Corresponding SOC [4]

4.1.4 Validation of Calibrated Model

Because of the relatively low C-rates that are observed in stationary energy storage applications, the model is validated on a data set that included the lowest C-rate conditions available in investigated literature [78]. The imposed C-rate profile

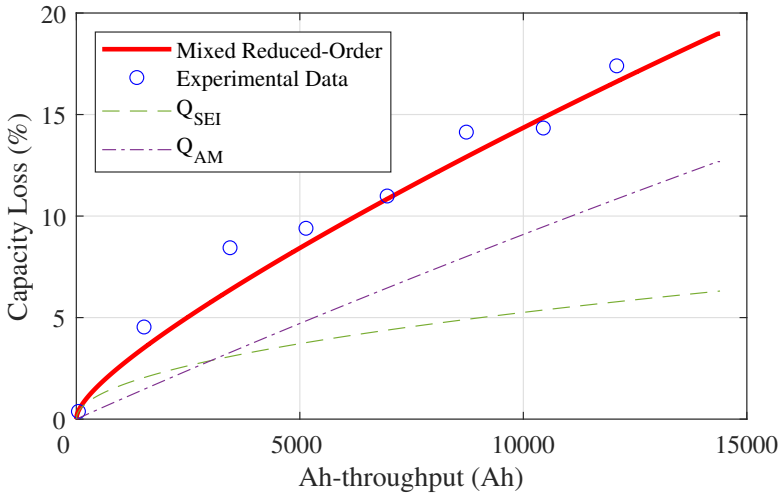

Figure 4.4: Comparison of the total capacity loss predicted by the mixed degradation model against the experimental data used for calibration

for the model verification cycles the battery between 20% and 95% and it is shown in Figure 4.5.

The results of the mixed-degradation model validation are shown in Figure 4.6. Overall, the model tends to underestimate capacity loss and this deviation is attributed to the different current profiles and C-rate used for calibration as compared the validation set. Improvements in model accuracy can be obtained by extending the calibration set, and ideally include low C-rate data.

4.2 Simulation Campaign Post-processing

For the work in this thesis, it is vital to understand if the developed HEM strategy in Chapter 3 results in greater battery capacity fade relative to a simpler control strategy such as the Baseline controller proposed in Chapter 2.2. As discussed, it

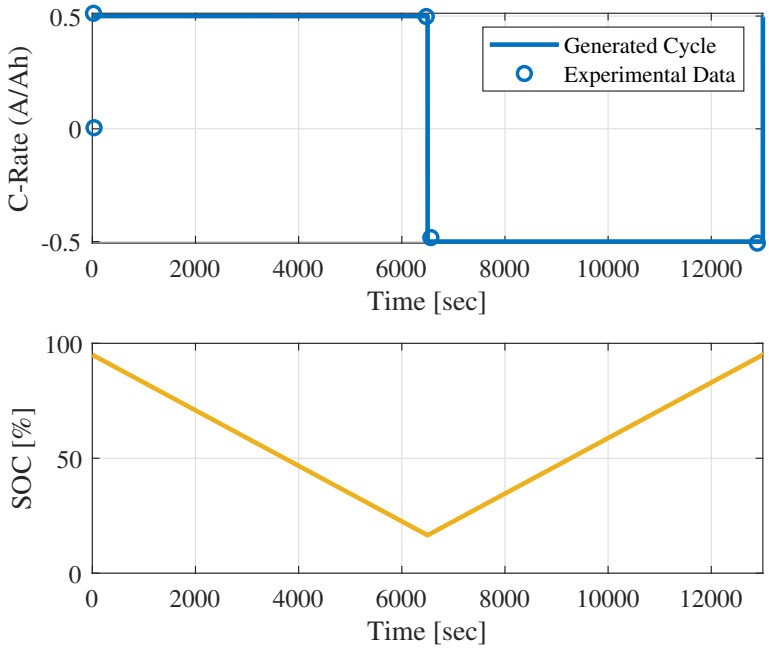

Figure 4.5: Synthesized current profile representing low C-Rate cycling [4]

is well understood the operation of the energy storage varies depending on the control strategy. For this reason, the mixed-degradation model presented in this chapter will be used to evaluate the capacity fade associated with the different current profiles that resulted from the HEM strategy operation.

4.2.1 Model Integration

To evaluate the capacity fade, Q_{tot} in Equation 4.3, the current profile, initial SOC, and ambient temperature obtained from the residential home simulator are imposed as inputs to the mixed-degradation model. As the battery ages, the battery capacity is fed back to the energy storage model within the plant model. The

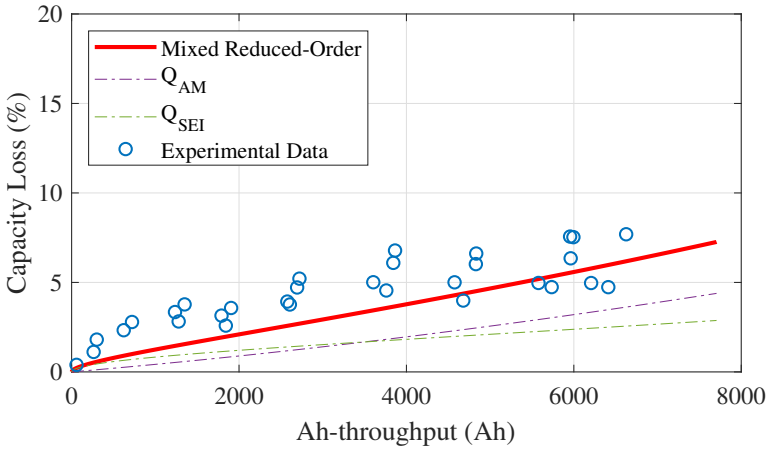

Figure 4.6: Validation of the total capacity loss predicted by the mixed-degradation model against experimental data.

integration of the semi-empirical battery aging model with the HEM system and smart home plant model is shown in Figure 4.7.

It is important to note that the battery model does not include a thermal model that accounts for the heat generated by the battery. This simplification is due to the reasonable assumption that only low C-rates are imposed on the battery which result in negligible heat generation. Hence, the battery temperature is assumed to be the same as the home temperature if stored inside, or ambient temperature if stored outside.

4.2.2 Simulation Campaign Battery Aging Results

An example of the 1-year battery total capacity fade, capacity fade due to SEI, and capacity fade due to LAM for each strategy is represented in Figures 4.8a, 4.8b and 4.8c respectively for case study 1. Additionally, the total capacity fade for a

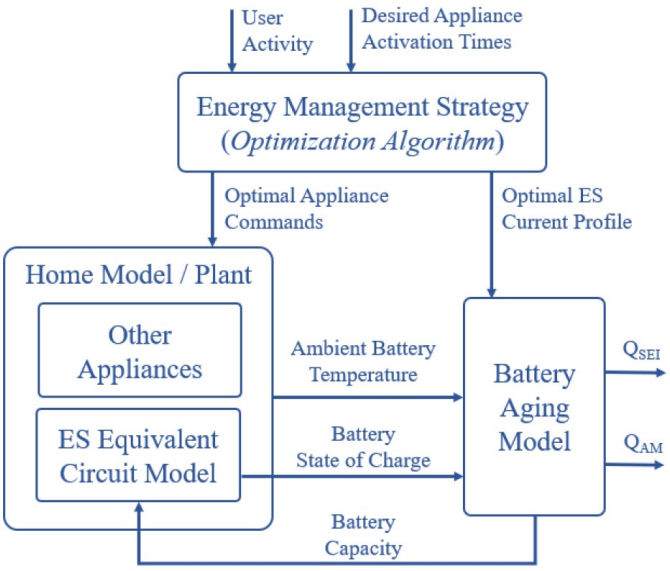

Figure 4.7: Home Energy Management System Integrated with Battery Aging Model Summary

battery without any imposed current, sitting at 20% SOC and 18°C (calendar aging only) is shown in Figure 4.8a. This demonstrates how the capacity fade due to the two control strategies matches up to a minimal capacity fade case.

For both control strategies, the total capacity fade is quite minimal and slightly over 1%. This minimal fade can be attributed to the fact that the battery was subject to extremely low C-Rates in which LAM capacity fade is heavily dependent on. This resulted in a LAM capacity fade less than 0.1%. Therefore, the main contributor to capacity fade in this application is SEI layer growth which is heavily dependent on battery SOC and temperature instead.

The rate of capacity fade was similar regardless of month or season as demonstrated in Figure 4.8a. However there is some slight variation shown in the rate of

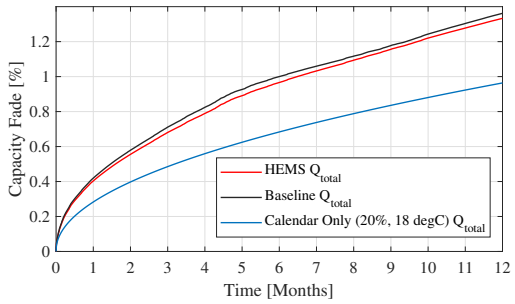

(a) Total Capacity Fade

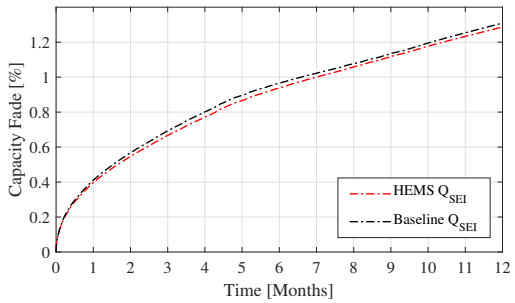

(b) Capacity Fade due to SEI Layer Growth

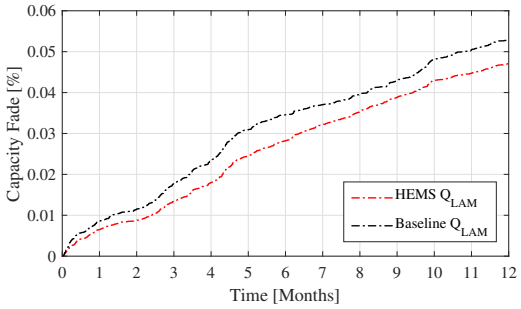

(c) Capacity Fade due to LAM

Figure 4.8: 1-Year Capacity Fade for Case Study 1

capacity fade due to loss of active material depending on month as seen in Figure 4.8c. This could be attributed to the differences in energy demand depending on season as the HVAC required variable amounts of power. There is a much greater variation in the rate of capacity fade as a function of season when the energy storage is installed outside and the battery temperature is equivalent to the ambient

temperature This is because battery degradation is heavily dependent on battery temperature.

Figure 4.9 shows the total capacity fade, average SOC, Charge and Discharge rates, and amp-hour throughput for each of the 12 one-year case studies from Table 3.6, which include dependencies on house size, location, vehicle battery size, energy storage battery size, and whether the battery is temperature controlled or not.

Figure 4.9a shows that the total capacity fade is similar for the two control strategies. Moreover, the strategy that caused greater capacity fade is different for each case study, suggesting that energy storage operation is dependent on case study and plant model settings rather than load scheduling method. The total Ah-throughput is shown in Figure 4.9b and is similar between cases, with minimal tendency for additional Ah-throughput imposed by the HEM strategy. This is consistent with the fact that the HEM strategy utilizes the energy storage more. However, this does not necessarily result in greater capacity fade because the model is somewhat insensitive to the different ranges of Ah-throughput between control strategies. Additionally, other factors than Ah-throughput may have a much greater impact of aging. The average state of charge, shown in Figure 4.9c, is slightly higher in the case of the HEM strategy, which again is consistent with the higher level of energy storage utilization observed in the HEM strategy. Similarly, to the Ah-throughput metric, the difference in state of charge is not sufficient to result in a change in capacity fade. Finally, the average charge and discharge rates are shown in Figure 4.9d and 4.9e, respectively. No significant difference can be observed in the average values. One thing to notice, however is that the average

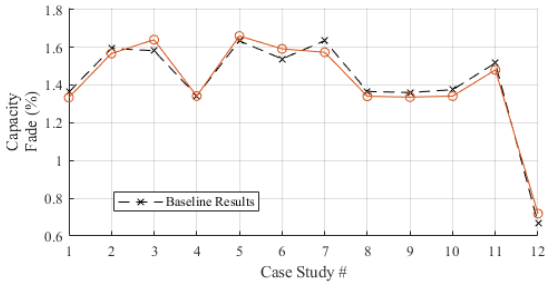

(a) Capacity Fade

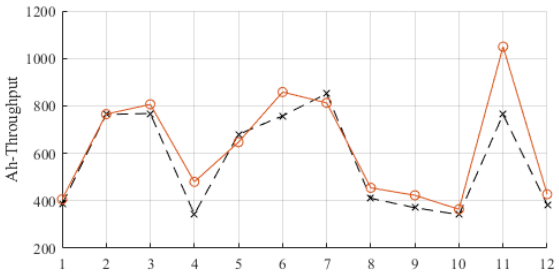

(b) Ah-Throughput

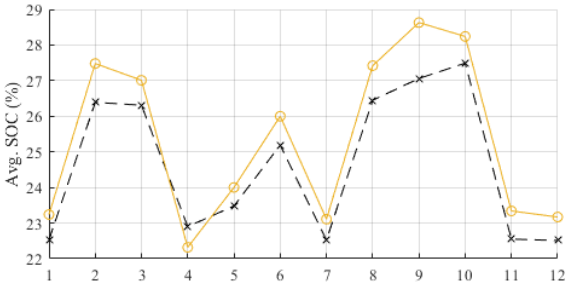

(c) Avg. SOC

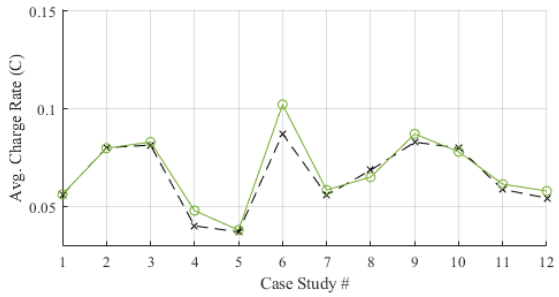

(d) Avg. Charge Rate

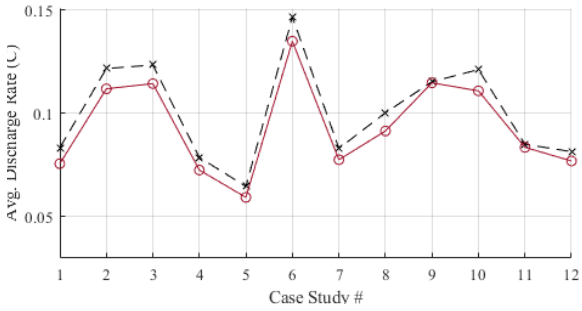

(e) Avg. Discharge Rate

Figure 4.9: Energy Storage Aggregate Capacity Fade and Operation Behaviour

C-rate is well below the calibration range of the aging model, resulting in extrapolation. Although the extrapolation may result in the capacity fade due to loss of active material being inaccurate, it is safe to assume the error is almost entirely negligible given that Q_{LAM} was nearly only a fraction of Q_{tot}.

4.3 Summary

In this thesis, a Mixed-Battery Degradation model was developed which combines the respective benefits of an entirely physics-based model and an empirical model. The model presented in this thesis allows for easy calibration for different battery chemistry types.

Although the model is computationally efficient, it is lacking validation in battery operating regions outside the calibration zone. Specifically, the battery was calibrated to a relatively large, unique C-rate profile; therefore, any model evaluation at different C-rate profiles will result in extrapolation of capacity fade in loss of active material that cannot ensure accuracy. However, when at low C-Rates, this error due to extrapolation could be considered nearly negligible because capacity fade due to loss of active material is minimal compared to the total capacity fade. Future work should calibrate the model at a wider range of C-rate profiles to extend the model validity. With additional validity, the model can be more confidentially implemented in real-time control applications.

In this thesis, the degradation model is used in post-processing to evaluate and compare the effect of different home energy management strategy on capacity fade. Although the operation of the energy storage system due to the HEM strategy was slightly different than that of the operation due to baseline control operation, the aggregate capacity fade in both cases was minimal and similar.

Chapter 5: Optimization of Battery Temperature and Durability for DC Fast Charging Applications

In 2019, the transportation sector was responsible for more than 29% of all greenhouse gas emissions in the United States, having surpassed the electric power generation sector in 2017 [79]. Newly developed plug-in electric and electric vehicles have been assessed to lower life-cycle emissions by 57% to 68% for comparable internal combustion engines [80]. However, the median driving range of an internal combustion engine vehicle in 2021 was 403 miles while that of an electric vehicle was only 234 miles [81]. In addition to the range anxiety experienced by electric vehicle adopters, the wait time to recharge the battery is also much longer than that required to refuel a conventional vehicle, resulting in reduced travel flexibility for the user.

For increased penetration in the transportation sector, electric vehicles must provide both economical and practical benefits to customers when compared with internal combustion engine vehicles. With respect to charging time, the state-of-the-art Direct Current Fast Charging (DCFC) units can provide more than 200 miles of range in 30 minutes but input significantly high power to the battery, between 25 to 350kW [82]. The associated charge current is large and results in higher battery temperatures, which has a great impact on battery life [83, 84]. In a study

conducted by the US National Renewable Energy Laboratory, a 15°C reduction in average battery temperature over the life-time of the battery was found to result in roughly a double useful battery life [85]. Additionally, insufficient battery thermal management could result in thermal runaway if the temperature reaches a critical point, posing a hazard to the user [86]. Due to the unavoidably high C-rates required for DCFC and the associated high temperatures, an effective battery thermal management system is thus essential for the safe fast charging at various operating conditions.

5.1 Current Practice for DCFC Optimization

While active cooling strategies have already been proposed to mitigate degradation due to heat [87], a preemptive approach is to implement charging strategies that maintain the temperature within desired bounds during fast-charging. In this case, the battery temperature control is more active compared to the application of cooling strategies. In terms of modeling, an equivalent circuit model describing the battery's electrochemical behavior is usually combined with a thermal model that captures the heat generation and dissipation. An optimal control framework is then built to minimize a cost function related to the battery degradation [88]. By integrating a battery aging model, it is possible to obtain a degradation aware charging profile that minimizes the degradation due to DC fast charging [89].

However, the challenge is that, the resulting optimal control problem formulation with an objective of achieving fast-charging while minimizing capacity fade is highly nonlinear due to the electro-thermal-aging coupling [90]. Many algorithms have been proposed to find solutions, with varying successes regarding to

real-time implementability. For example, DP resulted in a 4.6% reduction in capacity fade due to solid electrolyte interface growth over 3300 charge discharge cycles (only considering capacity fade due to charging), when compared with the constant-current (CC) charging protocol [91]. However, considering the number of states involved and the curse of dimensionality associated with DP, the computational expense is high. Moreover, their approach minimized temperature rise and capacity fade separately, yielding the possibility of two different charge profiles that minimize respective cost functions. The optimal control problem can also be solved using Pontryagin's Minimum Principle [92], where a simplified aging model is used to define a severity factor that compares the expected aging with that from a nominal current profile. This is thus dependent on the selection criteria of the nominal current profile, which varies significantly from user-to-user. Machine Learning methods have been recently investigated to minimize the capacity loss during fast charging [93]. While results are promising, the approach requires extensive laboratory testings to failure of batteries to ensure reliable predictions of on-board cycle-life estimation.

More computationally efficient methods have been investigated such as PSO [94]. Results from this multi-objective optimization showed fast convergence of the algorithm to a near globally-optimal solution to minimize capacity fade and charge time to achieve a desired Ahr throughput. However, this study and all other previously mentioned literature neglect the effect of driving the vehicle immediately after charging. This is a strong assumption since DCFC units are more likely to be utilized on long-distance drives, indicating a greater likelihood of immediate driving after the charge event [95]. Additionally, since the battery degradation is a

heavily dependent on pack temperature, and DCFC causes higher battery temperatures, the expected driving behavior post-charging under a higher temperature cannot be neglected.

In this thesis, the DCFC current profile is optimized considering expected future driving within the optimal control problem, to account for the higher temperatures at the end of charging. The solution is firstly obtained through DP to benchmark the results obtained from a real-time capable meta-heuristic optimization algorithm. Thus, the results provide an insight into the effect of battery temperature on the overall degradation during a charging event by considering both the charge and subsequent discharge processes. When the expected driving is not considered in the optimal control problem formulation, the results show a higher temperature at the end of charging with greater capacity fade at the end of the discharge cycle, indicating the importance of this consideration.

5.2 Thermally Coupled, Mixed-Degradation Model

The battery model consists of three main components, namely a 0^{th} order ECM, a lumped thermal mass model for the temperature dynamics and a simplified degradation model for battery aging, which are integrated as shown in Figure 5.1.

5.2.1 Equivalent Circuit Model

The state of charge (SOC) of the battery is defined as:

$$\frac{dSOC}{dt} = \frac{I(t)}{Q} \tag{5.1}$$

Where Q is the battery capacity and I(t) is the battery current.

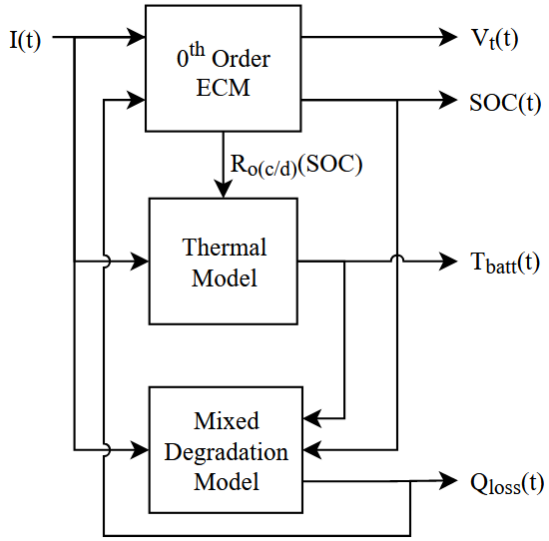

Figure 5.1: Coupled Battery System Block Diagram

A 0th order equivalent circuit model is then used:

$$V_{oc}(SOC) = V_t + R_{o(c/d)}(SOC) \cdot I \tag{5.2}$$

Where V_{OC} is the open-circuit potential, V_t is the terminal voltage, R_0 is the internal resistance, and c/d denotes charge and discharge respectively. The values for internal resistance and open circuit voltage in Equation 5.2 are obtained from [96].

5.2.2 Lumped Thermal Model

A simple lumped thermal mass model is developed to describe the battery temperature dynamics considering the effect of the battery current:

$$\frac{dT_{batt}}{dt} = \frac{1}{mc}(I^2 R_{o(c/d)} - hA(T_{batt} - T_{amb})) \tag{5.3}$$

Where m is the mass of the battery pack, c is the thermal capacity, h is the heat convection coefficient, A is the surface area, and T_{amb} is the ambient temperature. The values of the parameters are summarized in Table 5.1 and obtained from the specification sheet for the A123 System's 26650 LFP Cylindrical Battery Cell.

Table 5.1: Parameters for Thermal Model

Parameter	**Value**	**Unit**
m	0.07	kg
c	1100	$J/kg \cdot K$
h	5	$W/m^2 \cdot K$
A	$6.36E(-3)$	m^2

5.2.3 Mixed-Degradation Model Verification

The same mixed degradation model developed in Chapter 4 is used here which captures capacity fade due to SEI layer growth and loss of active material only. By using this model, an assumption is being made that capacity fade due to Lithium plating is non-existent during this DC fast-charging protocol. However, it is well known in literature that Lithium plating is also present in the cases of high C-Rates, high states of charge, and low temperatures [97]. While this mechanism heavily affects rate of capacity fade, it also leads to safety concerns because Lithium plating can result in dendrite formation across the electrolyte in the cell and potentially, a subsequent short circuit [97]. Therefore, state of the art fast charging requires the use of constant-current, constant-voltage (CC-CV) charging protocols which limit the allowable C-Rate towards the end of the charge cycle (near a high state of charge) to ensure Lithium plating does not occur [98].

The added current constraint for Lithium plating leads to infeasible solutions within the selected charge time for this work; specifically the battery cannot reach full charge in 15-minutes. Therefore, the presence of Lithium plating and it's maximum current constraints have been neglected in the initial results presented in Section 5.4 to test the algorithm and allow for a proof of concept. However, it is still desired to analyze potential capacity fade reduction in fast charging cycles while also considering the constraints of Lithium plating. Section 5.5 presents additional results with as a result of including the Lithium plating constraint.

To validate the degradation model for this specific application of DC fast charging, battery capacity fade data for an EV with a 'complex duty cycle' was obtained from [5] for a 2.3 Ah LFP battery from A123 Systems (26650). The battery was charged up to 100%, held for a rest period, and discharged using this duty cycle. The cycle was repeated to yield a one-year capacity fade profile. The imposed current profile, together with a comparison between model results and original data are shown in Figure 5.2, which shows a good validation of the degradation model. With modeling for one year, the capacity fade is 6.58% and the data shows a 7.57% fade.

5.3 Optimization of Charging Profile

5.3.1 Problem Formulation

The objective of the DC Fast Charging controllers is to optimize a charging profile $u(t)$ such that the total capacity fade, due SEI layer growth and loss of active material, of the battery is minimized over both a charge and subsequent

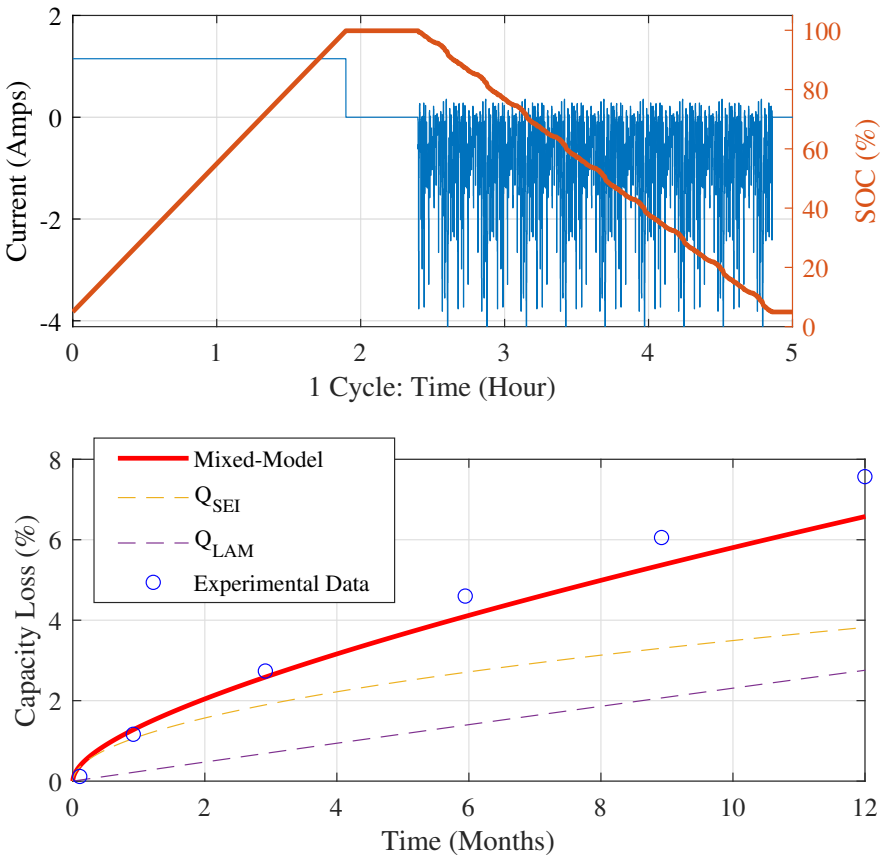

Figure 5.2: One year mixed-degradation model validation on experimental data from [5]

discharge cycle, subject to state and input constraints:

$$\begin{aligned} \min_{u} J(x,u,w) &= \int_0^{t_f} Q_{total}(x,u,w)dt \\ \text{s.t.} \quad \dot{x} &= f(x,u) \\ x_{min} \leq x(t) &\leq x_{max} \\ 0 \leq u(t) &\leq u_{max} \\ w(t) = 0 \quad \forall \quad 0 < t &\leq t_{ch} \\ u(t) = 0 \quad \forall \quad t_{ch} < t &\leq t_f \end{aligned} \tag{5.4}$$

where x is the state vector $x = \begin{bmatrix} SOC & T_{batt} & Q_{total} \end{bmatrix}^T$; $f(x,u)$ defines the state dynamics; and $w(t)$ is the external input vector which defines the current while driving. The total time, t_f, is a fixed time that includes both charging, t_{ch}, and driving time, $t_f - t_{ch}$. The charging time is also fixed in this problem. With this definition of control input and external input, the SOC equation in Eq. (5.1) becomes:

$$\frac{dSOC}{dt} = \frac{(u(t) + w(t))}{3600} \tag{5.5}$$

The constraints on state variables are based on A123 Systems, High Power Lithium Ion ANR26650:

$$\begin{aligned} SOC_{min} \leq SOC(t) \leq SOC_{max} \\ T_{batt,min} \leq T_{batt}(t) \leq T_{batt,max} \end{aligned} \tag{5.6}$$

Moreover, at the end of the charging event at time t_{ch}, the battery must be at the required SOC (fully charged):

$$SOC(t_{ch}) = SOC_{max} \tag{5.7}$$

Finally, an algebraic constraint is introduced on the terminal voltage $V_t(t)$ based on the battery specifications and Equation 5.2:

$$V_{t,min} \leq V_t(t) \leq V_{t,max} \tag{5.8}$$

Due to the nonlinearities in the optimization problem, a possible solution approach is based on DP [99]. However, due to the size of the state vector, DP is computationally prohibitive for online implementation [91]. Moreover, splitting the battery current into a controllable profile $u(t)$ and an external input $w(t)$ makes

the DP challenging to implement without further increasing the number of states. For this reason, a meta-heuristic optimization technique, PSO, is implemented to find a near optimal solution with reduced computation time [100].

5.3.2 PSO Implementation

PSO is a population-based metaheuristic algorithm where the position of each particle in the swarm is a potential solution to the optimization problem [101]. The population or swarm of particles is initialized with positions randomly assigned throughout the feasible search space and the cost associated with the position of each particle is computed. Assuming a minimization objective, the cost associated with the position of each particle is saved as the 'personal best' solution for that particle while for the entire swarm, the solution with the minimum cost is saved as the 'global best' solution. The position and associated cost of each particle is updated at every iteration, based on a velocity equation that is a function of the personal and global best solution. The exploration through the search space continues for a defined maximum number of iterations, or until convergence.

For 2^m time-steps required for DCFC, the C-rate $u(t)$ is optimized over a 2^m dimensional search space. To ensure that the battery is charged up to the defined SOC_f, $\bar{u}_{cc}$ which is the constant C-rate required to charge fully, is first calculated. Then sequentially, the constant C-rate is repeatedly discretized temporally into two, while maintaining the average current to be $\bar{u}_{cc}$ over the available time.

At the first discretization step, two C-rates $u_p(1)$ and $u_p(2)$ must be obtained that have a mean current of $\bar{u}_{cc}$. This is as defined by Eq. (5.9) where SOC_0 is the

initial SOC, in decimals and t_{Ch} is the available charging time in hours.

$$\bar{u}_{cc} = \frac{SOC_f - SOC_0}{t_{Ch}} = \frac{u_p(1) + u_p(2)}{2} \tag{5.9}$$

This constraint is implemented within a 1D PSO exploration of the first discretization, by defining the particle position x_p as the deviation from $\bar{u}_{cc}$, yielding C-rates $u_p(1)$ and $u_p(2)$ as obtained in Eq. (5.10, 5.11). These C-rates contribute to the Q_{total} which is the integrand of the cost function used in the PSO.

$$u_p(1) = \bar{u}_{cc} + x_p \quad \text{and} \quad u_p(2) = \bar{u}_{cc} - x_p \tag{5.10}$$

$$-\bar{u}_{cc} \leq x_p \leq u_{max} - \bar{u}_{cc} \tag{5.11}$$

The update equations of the PSO are defined by Eq. (5.12-5.13) where tunable parameters of the algorithm are the inertial weight b and acceleration coefficients c_1 and c_2. Random numbers $r_1, r_2 \in [0, 1]$ perform the stochastic aspect of the exploration, k is the iteration number, p is the particle identity and α is the relaxation factor.

$$v_p^{k+1} = bv_p^k + c_1 r_1 (pbest_p - x_p^k) + c_2 r_2 (gbest_p - x_p^k) \tag{5.12}$$

$$x_p^{k+1} = x_p^k + \alpha x_p^{k+1} \tag{5.13}$$

After the exploration of the search space at the first discretization step, the optimal deviation x_* is found by the 1D PSO and the resulting charge profile is composed of $u_*^{1D}(1)$ and $u_*^{1D}(2)$ as illustrated in Figure 5.3.

To discretize further and obtain a 4 time-step C-rate profile that maintains $\bar{u}_{cc}$ as the overall average current, the first two time-steps and last two time-steps must average $u_*^{1D}(1)$ and $u_*^{1D}(2)$ respectively. This is achieved by a 2D PSO where the particle position is associated with $x_p(1)$ and $x_p(2)$ which are the respective

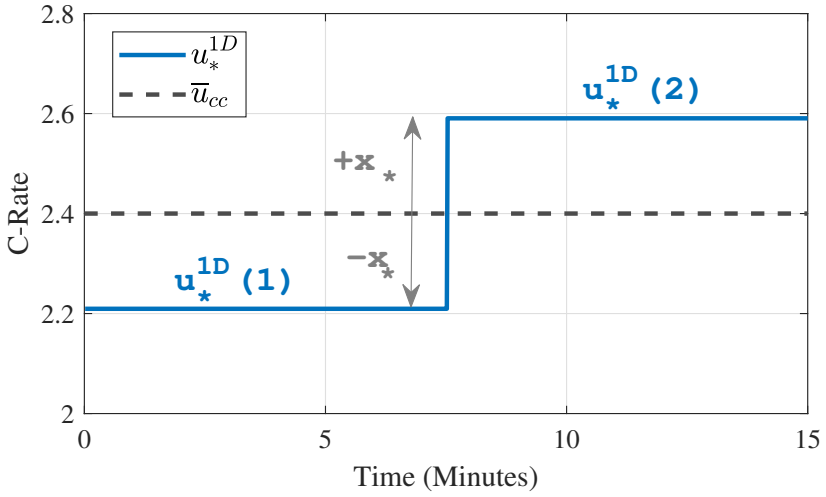

Figure 5.3: 1-D PSO Optimal Solution

deviations from $u_*^{1D}(1)$ and $u_*^{1D}(2)$ as described by Equation (5.14-5.17). Once the PSO finds the optimal position denoted by x_*, the 4 step current profile is given by $u*^{4D}$ as illustrated in Figure 5.4

$$u_p(1) = u_*^{1D}(1) + x_p(1) \quad \text{and} \quad u_p(2) = u_*^{1D}(1) - x_p(1) \tag{5.14}$$

$$u_p(3) = u_*^{1D}(2) + x_p(2) \quad \text{and} \quad u_p(4) = u_*^{1D}(2) - x_p(2) \tag{5.15}$$

$$-u_*^{1D}(1) \leq x_p(1) \leq u_{max} - u_*^{1D}(1) \tag{5.16}$$

$$-u_*^{1D}(2) \leq x_p(2) \leq u_{max} - u_*^{1D}(2) \tag{5.17}$$

This approach of increasing discretization by repeatedly doubling the time-steps can be continued until the desired number of discretized time-steps is reached. Thus, 1D, 2D, 4D, ... , 2^{m-1}D PSOs are performed sequentially to arrive at the C-rates for the 2^m time-steps. At each new PSO formulation, the overall average

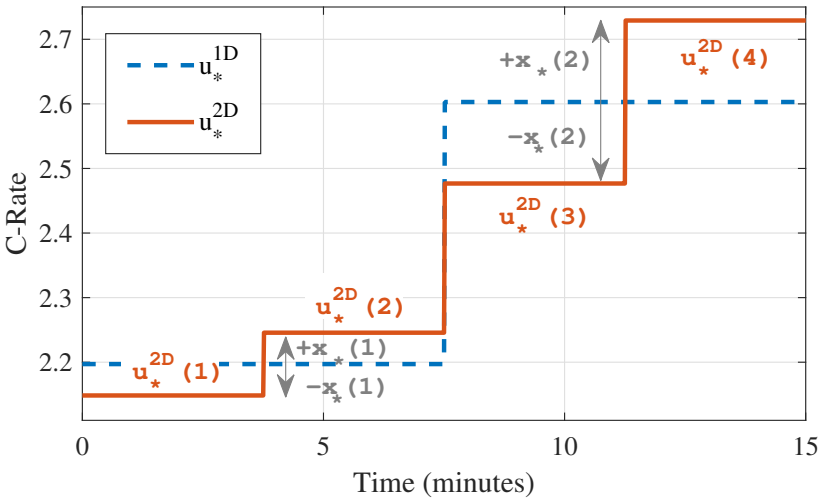

Figure 5.4: 2-D PSO Optimal Solution

current is maintained to be $\bar{u}_{cc}$ with the discretization rule for the ND PSO summarized in Equation (5.18).

$$\frac{u_*^{2ND}(2n-1)+u_*^{2ND}(2n)}{2} = u_*^{ND}(n); \qquad for \quad n=[1:N] \tag{5.18}$$

In this example, discretization up to 8 time-steps was desired, and so 1D, 2D and 4D PSOs were run and the final solution is illustrated in Figure 5.5.

For a simplified case without considering the discharge cycle, the C-rate profile obtained from the PSO algorithm is compared against that from the DP algorithm described in [102]. The solutions are shown in Figure 5.6, where the overall shape of the charge profiles are similar between the two algorithms, with a root mean square deviation of 0.57 and total Q_{loss} listed in Table 5.2. The difference in resulting solutions may be attributed to the metaheuristic nature of the PSO and the

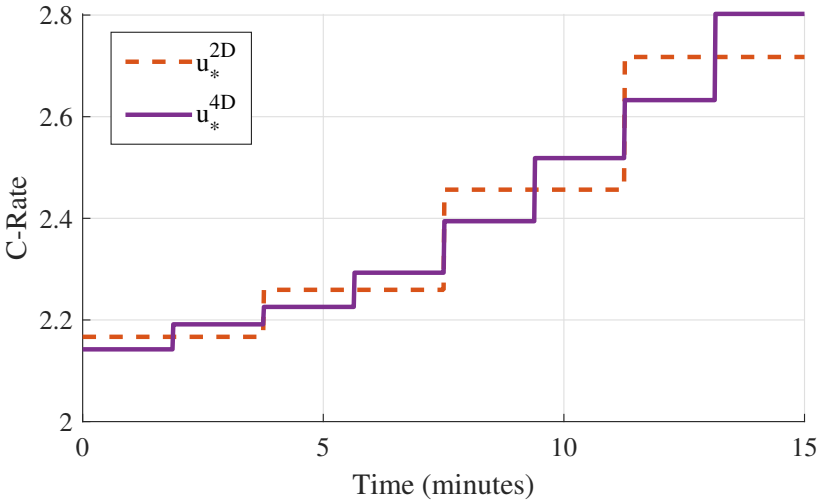

Figure 5.5: 4-D PSO Optimal Solution

discretization of the DP algorithm used. Additionally, this DP algorithm interpolates for state variable positions and uses a backward recursion approach while the PSO simulates forward.

Table 5.2: DP vs PSO Computation

	Computation Time	Q_{loss}
DP	$\tilde{3}$ Hours	0.019%
PSO	$\tilde{3}$ Minutes	0.020%

5.4 DC Fast Charging Optimization Results

Following the optimization steps prescribed earlier, an 8-step charging profile was obtained for a 15-minute DC fast charge (20% to 80% SOC) initialized at

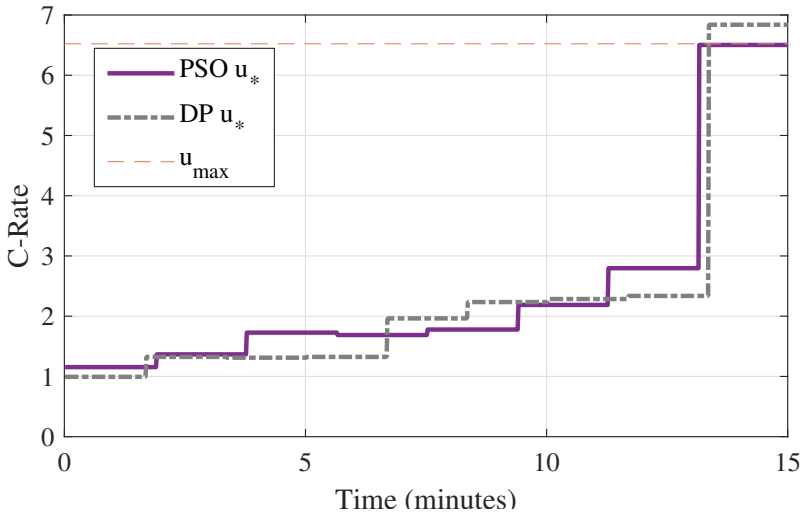

Figure 5.6: PSO Validation vs Optimal DP Solution

25°C followed by a complex EV duty cycle discharge (to 20% SOC). The obtained charging profile is compared with a baseline policy that uses constant-current in Fig. 5.7, which also shows the battery temperature during charging and discharging. The total capacity fade after the optimized charge-discharge cycle was found to be 0.1015% while that for the baseline was found to be 0.1022% over a single cycle.

To evaluate the importance of considering the driving load immediately after DCFC, another study was conducted in which only the charging profile was optimized (the discharge was not included in optimization). The resulting optimized charge policy left the battery 12°C hotter than in the previously studied charge policy that accounted for future discharge. This is shown in Fig. 5.8 and the resulting capacity fade of the battery from this policy was 0.1362% compared to that of the baseline constant-current policy of only 0.1022% over just one cycle.

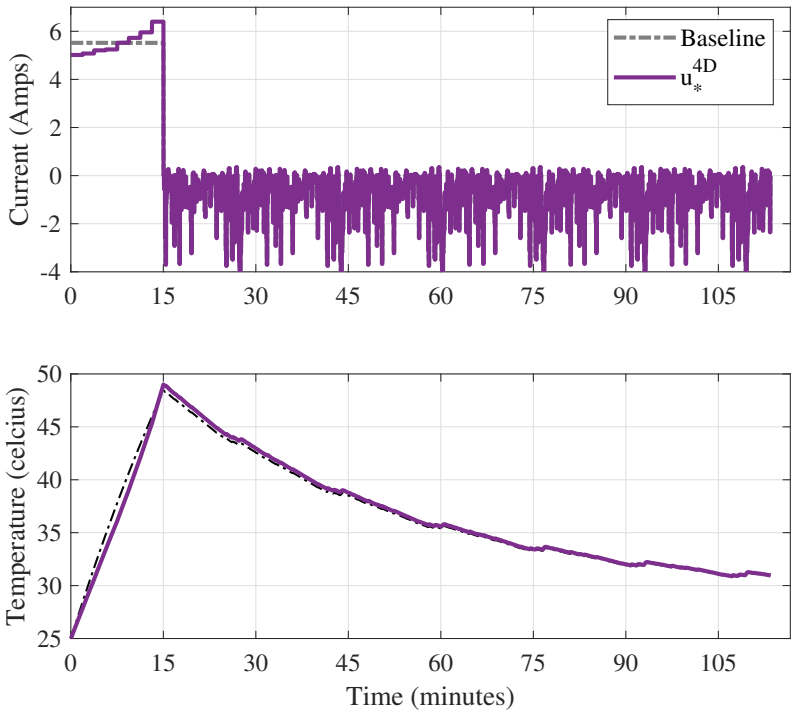

Figure 5.7: Optimal Charging Policy and Temperature with Discharge Considered in Optimization

One of the primary mechanisms of degradation is capacity loss due to SEI layer growth, which is greater when the battery is held at a high SOC. Therefore, keeping the battery at a lower SOC for a longer period would be advantageous to limit capacity fade, as seen in the profiles obtained from the PSO. Additionally, temperature also plays a significant role in capacity loss, both in the loss of active material and in the SEI layer growth by affecting the reaction rate multiplied with k_{SEI} and k_{LAM}. This explains why the optimized profiles do not impose larger C-Rates on the battery which would yield larger temperatures.

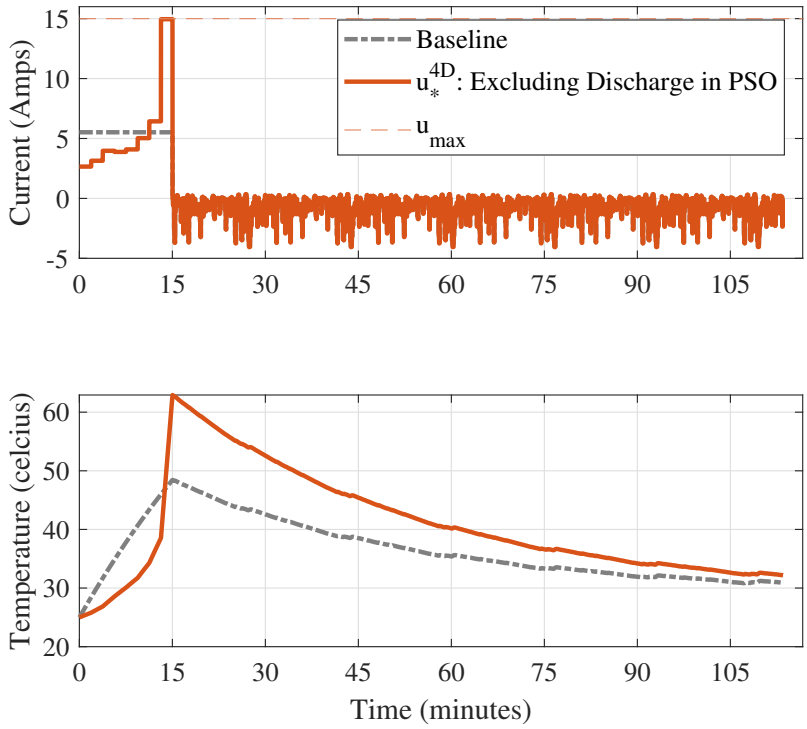

Figure 5.8: Optimal Charging Policy and Temperature without Discharge Considered in Optimization

It is also of interest to evaluate how the optimized charge policy evolves over extended simulations because the capacity loss due to SEI layer growth contributes lesser to the total capacity loss as the battery ages [5,76,77]. As shown in Figure 5.9 a battery starting at 0% capacity fade, the charge-discharge cycle of the initial study was repeated 100 times, where the PSO optimization of charging was repeated every 10 cycles.

It is clear that at charging sessions in later battery life the optimal policy limits the amount of battery temperature rise due to high C-Rate rather than limiting time

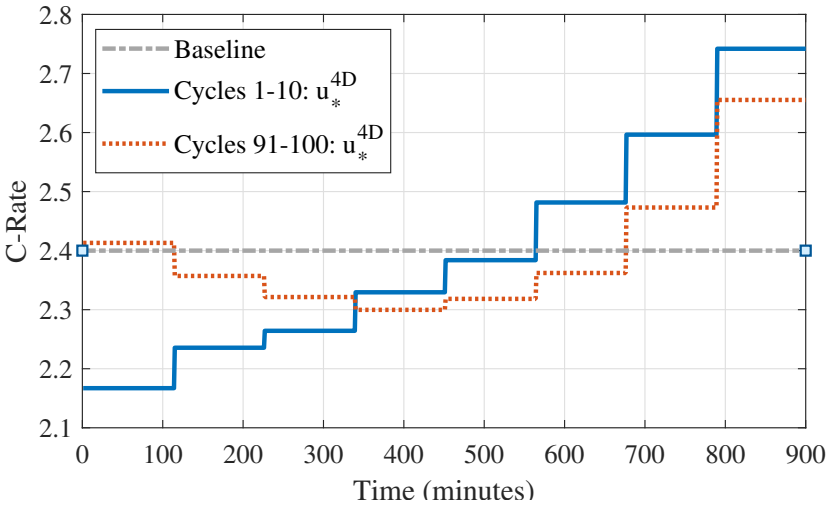

Figure 5.9: Evolution of Optimal Charging Profile as the Influence of Q_{SEI} Decreases

at high SOC given that Q_{LAM} becomes the dominant loss mechanism in Q_{total}. The characteristic result in a charge profile increasingly similar to a constant-current charge profile and it can be assumed that this trend will continue as time goes on.

5.5 Results Considering Lithium Plating

As mentioned in Section 5.2.3, it is desired to analyze results which consider current constraints to ensure Lithium plating does not occur. To do achieve this result, a CC-CV profile is used to determine maximum allowable current as a function of state of charge such that Lithium plating does not occur. Available data for this maximum current was obtained from test cycles on an NMC battery type as a function of battery voltage. By utilizing the open-circuit voltage versus state of charge curve, the voltage can be defined as state of charge and assumed to be similar to other battery types such as LFP as in this application. The cost function

will not change with this new constraint; rather, when the constraint is broken the respective cost will be set substantially high such that the algorithm stays within desired current bounds as a function of state of charge. The maximum current constraint as a function of state of charge for the LFP battery type is shown in Figure 5.10.

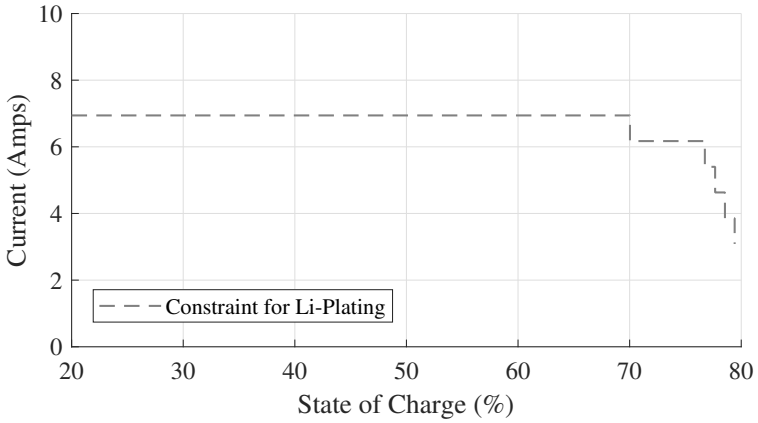

Figure 5.10: LFP Maximum Current Constraint to Limit Li-Plating

Again, due to the infeasibility of a solution within a 15 minute charge cycle, the charging time was extended to 25 minutes. The optimal charging policy over the 25-minute charge cycle is shown in Figure 5.11. It is clear that the constraint was held such that Lithium plating does not occur. The resultant total capacity fade after the charge and discharge cycle due to loss of active material and SEI layer growth amounted to 0.071%. In comparison, the baseline constant-current profile also resulted in a total capacity fade of 0.071% at the end of the charge and discharge cycle. This extreme similarity in total capacity fade is because the optimal

charge protocol was nearly constant current. The implication of this result is that when considering Lithium-plating, the state of the art CC-CV charging protocol is the best approach to charge electric vehicles in minimal time frames.

Also shown in Figure 5.11 is the optimal charge protocol for the case without the constraint for Lithium plating for a 25 minute charge period. For the case without the Lithium plating constraint, the current tends to ramp up throughout the entire charge cycle as was discovered previously. Although this will yield slightly less capacity fade due to loss of active material and SEI layer growth, it cannot be ensured that Lithium plating will not occur.

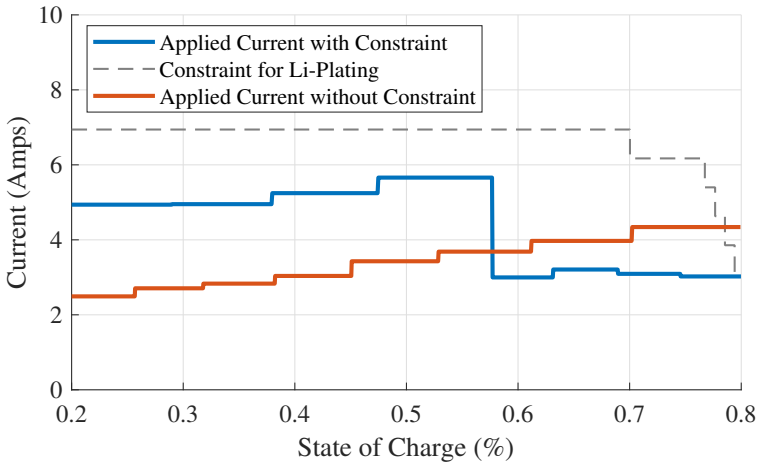

Figure 5.11: Optimal Charging Policy with Constraint for Li-Plating

A summary of the capacity fade due to both mechanisms for both cases at the end of the charge cycle and at the end of the discharge cycle is summarized in Table

Table 5.3: Capacity Fade by Mechanism for Considering and Not Considering Lithium Plating

	Considering Plating	**Without Considering Plating**
Q_{tot} (At End of Charge)	0.026	0.023
Q_{SEI} (At End of Charge)	0.025	0.022
Q_{LAM} (At End of Charge)	0.001	0.001
Q_{tot} (At End of Discharge)	0.071	0.070
Q_{SEI} (At End of Discharge)	0.070	0.069
Q_{LAM} (At End of Discharge)	0.001	0.001

5.3. Additionally, it should be noted that in both cases the total charging time and the total Ah-throughput is equivalent.

5.6 DC Fast Charging Optimization Discussion / Conclusions

In this thesis, a PSO algorithm was used to optimize a discrete-step DCFC current profile, such that the battery capacity fade was minimized. The capacity fade due to an expected drive cycle immediately after charging was imposed as an additional cost in the objective function to mimic realistic charging and driving conditions. The results of the PSO algorithm showed a decrease in overall capacity fade compared to the baseline CC profile and was computationally efficient enough to be solved in real time. Future work will include the use of data driven methods to generate synthetic current profiles for the driving portion of the optimization problem.

However, in light of state of the art fast charging approaches with CC-CV to ensure Lithium-plating does not occur, this type of optimization is practically infeasible because the added current constraints. These constraints limit almost all flexibility of the charging profile to reduce capacity fade for SEI layer growth or loss of active material.

Chapter 6: Conclusion and Future Work

This thesis presented a HEM strategy to control the optimal scheduling of a smart home's appliance load time, HVAC operation, xEV charging, and coupled ES-RES energy distribution. The goal of HEM controller was to minimize a multi-objective function which considered the grid electricity cost, the deferral time of the appliances that are activated with a delay, and the temperature discomfort considering the difference between the desired and actual temperatures. The loads in the smart home was coordinated using a sequential MPC approach. The resulting nonlinear mixed-integer optimization problem within the receding horizon was solved using Genetic Algorithm.

An extensive simulation study was conducted by varying the house size, location, vehicle battery size, energy storage battery size, and energy storage temperature control with the objective of evaluating the benefit of a smart home energy management system. The simulation study showed that on average, the developed HEM strategy reduced grid cost by approximately $160 per year relative to the the simpler, baseline controller. The total savings tended to be greater for larger house sizes, houses located in San Antonio, houses with a 60 kWh battery sized vehicle, and in the summer months. Additionally, it was found that varying the energy storage size did not result in much change between relative savings because regardless

of size, the entire capacity of the battery was never utilized. The temperature control also did not make an impact on the relative cost savings.

The economical benefits shown by the HEM system were obtained through an improved load coordination strategy that heavily relied on the stationary battery. To evaluate the additional battery degradation, and hence, the consequences on the cost-benefits analysis, a mixed-degradation model was developed. By calculating the capacity fade associated with both, the HEM and baseline strategy, a negligible difference in degradation was observed.

6.1 Future Work

Consistently with the literature on energy storage systems for smart homes, the capacity loss has been evaluated a posteriori and was not included in the optimization strategy. The simulation study has shown that the developed HEM strategy resulted in an extremely similar battery capacity loss compared to a baseline controller. While the simulation campaign showed limited effect of using an advanced smart home algorithm on long-term capacity fade, the developed semi-empirical aging model used in this study was calibrated using supplier data collected for automotive applications, which are at relatively high C-rate. The energy storage would age differently at the lower C-rates in the order of C/20 that are common in stationary applications (both, stationary energy storage and vehicle to home). For example, a study on low C-rate cycling published by [103] showed that these specific operating conditions could result in the traditional aging models to significantly under-predict the long-term aging effects.

Appendix A: Simulation Campaign Results

The effect of xEV battery size variation will be analyzed as shown in Figure A.1. On average the total grid cost savings of using the HEMS controller instead of the Baseline controller was 3.7%. This can be assumed to have less grid savings with a smaller xEV battery size because there is less relative power required to charge which can be deferred to lower price regions. This effect can be seen well in the major difference in overall xEV load deferral between sizes. Additionally, from the other plots in the figure, it is clear that the other metrics were relatively unaffected.

As shown in Figure A.2, the effect of ES battery size will be analyzed next. What should be considered mainly in this case is the comparison between two different sized ES systems for two different house sizes; the 2500 to 3500 square foot house with a 14 kWh or 28 kWh battery & the 3500 to 4500 square foot house with a 28 kWh or 14 kWh battery. Of course, in both cases when the battery capacity was decreased the average state of charge of the battery increased and the relative rates of charge and discharge increased. However, in considering all other metrics, there was not much deviation.

Next, as shown in Figure A.3, the effect of ES temperature control will be analyzed. Again, the ES system subject to temperature control had an assumed battery

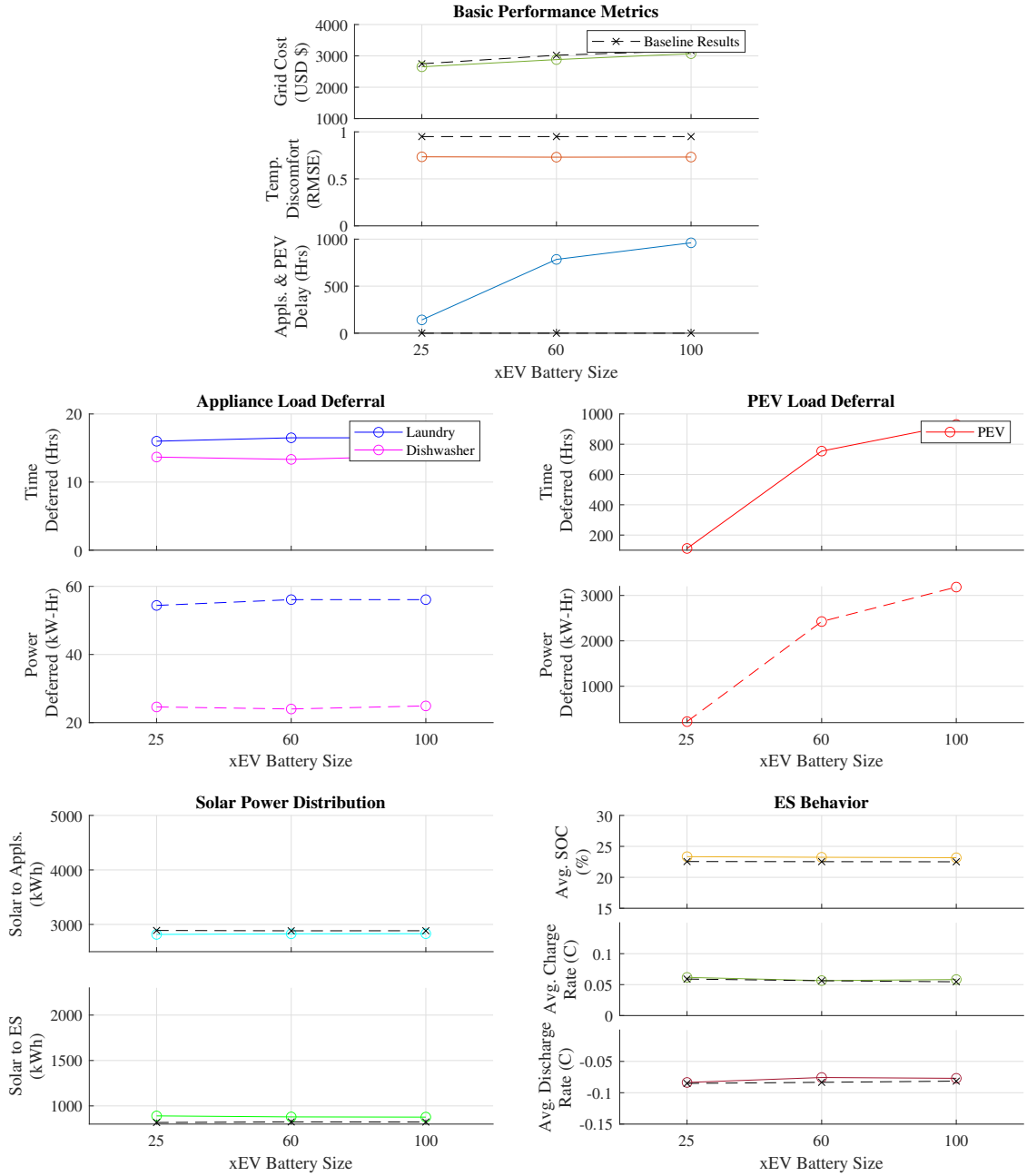

Figure A.1: Effect of xEV Battery Size on HEMS & Baseline Controller Operation

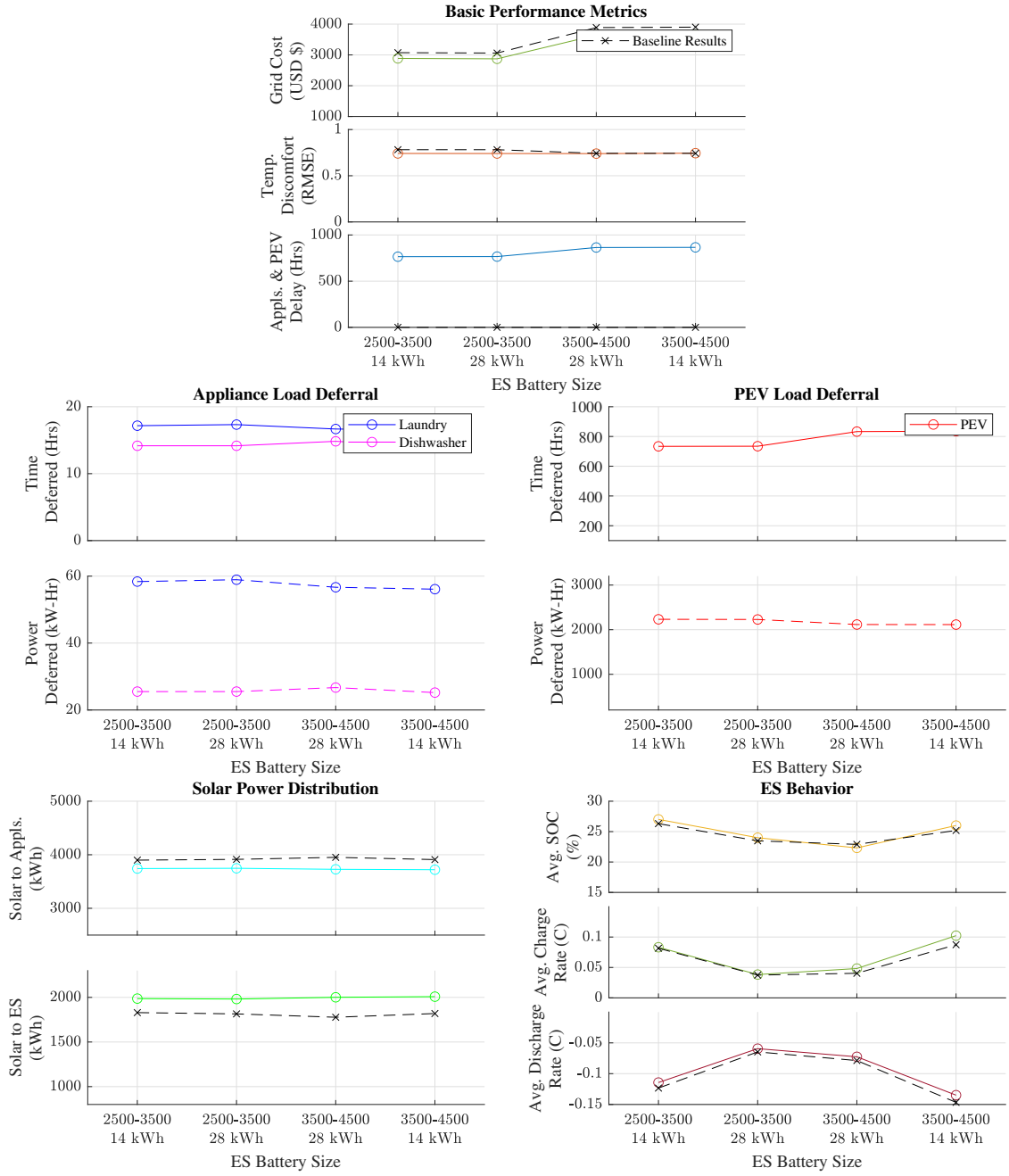

Figure A.2: Effect of ES Battery Size on HEMS & Baseline Controller Operation

temperature equivalent to the house temperature and the ES system without temperature control assumed a battery temperature equivalent to the ambient temperature. As clearly seen in the plots, this had no effect on the operation metrics of the systems.

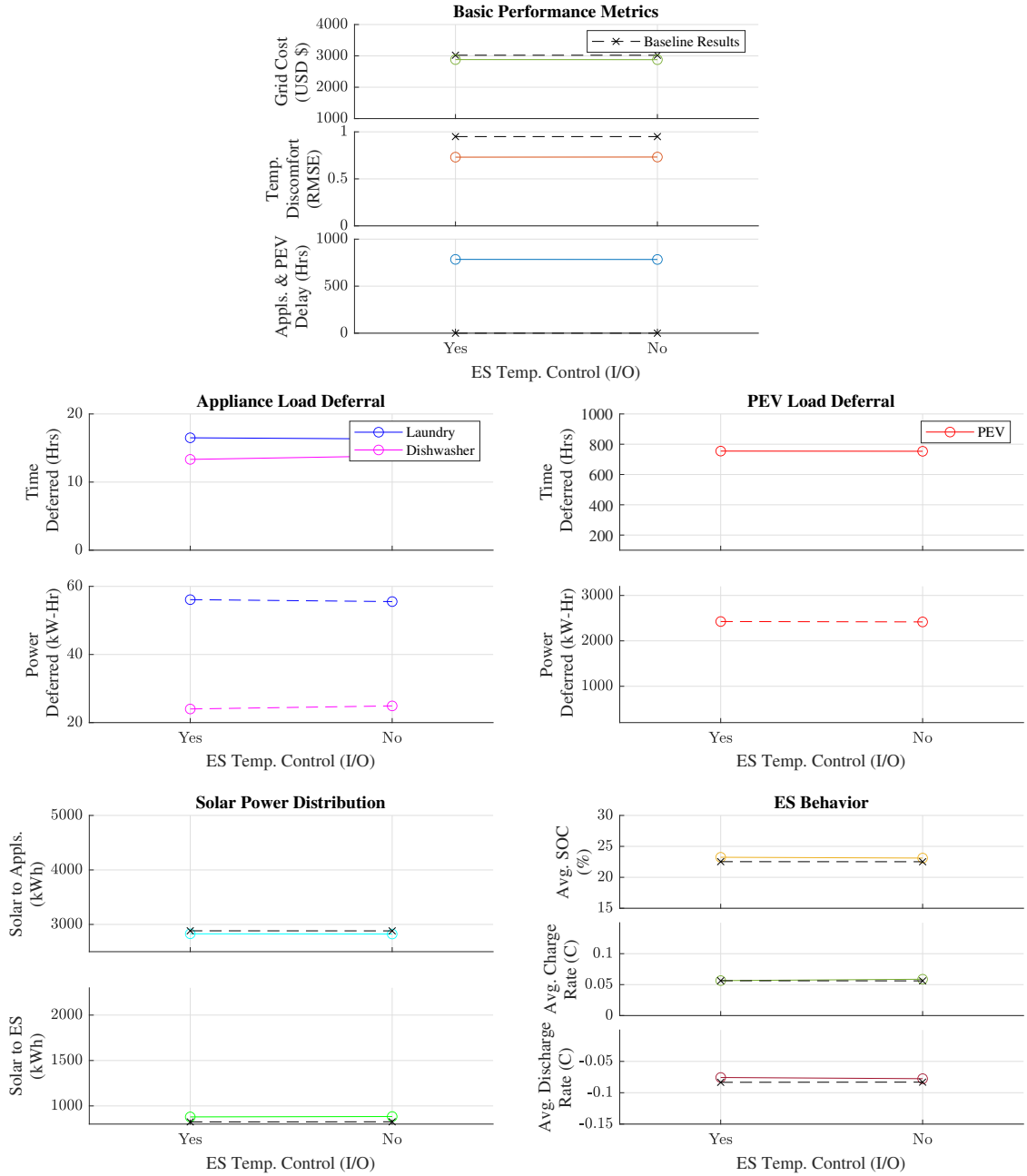

Figure A.3: Effect of ES Temperature Control on HEMS & Baseline Controller Operation

Bibliography

[1] U.S. Energy Information Administration - EIA - independent statistics and analysis.

[2] Godiana Hagile Philipo, Yusufu Abeid Chande Jande, and Thomas Kivevele. Demand-side management of solar microgrid operation: Effect of time-of-use pricing and incentives. *Journal of Renewable Energy*, 2020, 2020.

[3] Xing Jin, Ashish Vora, Vaidehi Hoshing, Tridib Saha, Gregory Shaver, R Edwin García, Oleg Wasynczuk, and Subbarao Varigonda. Physically-based reduced-order capacity loss model for graphite anodes in li-ion battery cells. *Journal of Power Sources*, 342:750–761, 2017.

[4] C Delacourt and M Safari. Life simulation of a graphite/lifepo4 cell under cycling and storage. *Journal of The Electrochemical Society*, 159(8):A1283, 2012.

[5] M Safari and C Delacourt. Aging of a commercial graphite/lifepo4 cell. *Journal of The Electrochemical Society*, 158(10):A1123, 2011.

[6] National Climatic Data Center, NESDIS, NOAA, and U.S. Department of Commerce. Global surface summary of the day - gsod.

[7] NOAA (National Oceanic and Atmospheric Administration). Climate change indicators: Heat waves, Jul 2022.

[8] Lawrence A Palinkas, Michael S Hurlburt, Cecilia Fernandez, Jessenia De Leon, Kexin Yu, Erika Salinas, Erika Garcia, Jill Johnston, Md Mostafijur Rahman, Sam J Silva, et al. Vulnerable, resilient, or both? a qualitative study of adaptation resources and behaviors to heat waves and health outcomes of low-income residents of urban heat islands. *International Journal of Environmental Research and Public Health*, 19(17):11090, 2022.

[9] Mayuri Rajput, Godfried Augenbroe, Brian Stone, Matei Georgescu, Ashley Broadbent, Scott Krayenhoff, and Evan Mallen. Heat exposure during a power outage: A simulation study of residences across the metro phoenix area. *Energy and Buildings*, 259:111605, 2022.

[10] Lisa Patel, Kathryn C Conlon, Cecilia Sorensen, Samia McEachin, Kari Nadeau, Khyati Kakkad, and Kenneth W Kizer. Climate change and extreme heat events: how health systems should prepare. *NEJM Catalyst Innovations in Care Delivery*, 3(7):CAT–21, 2022.

[11] Shady Attia, Ronnen Levinson, Eileen Ndongo, Peter Holzer, Ongun Berk Kazanci, Shabnam Homaei, Chen Zhang, Bjarne W Olesen, Dahai Qi, Mohamed Hamdy, et al. Resilient cooling of buildings to protect against heat waves and power outages: Key concepts and definition. *Energy and Buildings*, 239:110869, 2021.

[12] Anna M Brockway and Laurel N Dunn. Weathering adaptation: Grid infrastructure planning in a changing climate. *Climate Risk Management*, 30:100256, 2020.

[13] John Confrey, Amir H. Etemadi, Steven M. F. Stuban, and Timothy J. Eveleigh. Energy storage systems architecture optimization for grid resilience with high penetration of distributed photovoltaic generation. *IEEE Systems Journal*, 14(1):1135–1146, 2020.

[14] Charles Ibrahim, Imad Mougharbel, Hadi Y Kanaan, Nivine Abou Daher, Semaan Georges, and Maarouf Saad. A review on the deployment of demand response programs with multiple aspects coexistence over smart grid platform. *Renewable and Sustainable Energy Reviews*, 162:112446, 2022.

[15] Sergio B. Sepúlveda-Mora and Steven Hegedus. Making the case for time-of-use electric rates to boost the value of battery storage in commercial buildings with grid connected pv systems. *Energy*, 218:119447, 2021.

[16] Anawach Sangswang and Mongkol Konghirun. Optimal strategies in home energy management system integrating solar power, energy storage, and vehicle-to-grid for grid support and energy efficiency. *IEEE Transactions on Industry Applications*, 56(5):5716–5728, 2020.

[17] Onur Ayan and Belgin Turkay. Domestic electrical load management in smart grids and classification of residential loads. In *2018 5th International Conference on Electrical and Electronic Engineering (ICEEE)*, pages 279–283. IEEE, 2018.

[18] U.S. Energy Information Administration. Residential energy consumption survey (recs). 2020.

[19] Christoph Goebel, Vicky Cheng, and Hans-Arno Jacobsen. Profitability of residential battery energy storage combined with solar photovoltaics. *Energies*, 10(7):976, 2017.

[20] Behnam Zakeri, Samuel Cross, Paul E Dodds, and Giorgio Castagneto Gissey. Policy options for enhancing economic profitability of residential solar photovoltaic with battery energy storage. *Applied Energy*, 290:116697, 2021.

[21] Berk Celik, Siddharth Suryanarayanan, Robin Roche, and Timothy M Hansen. Quantifying the impact of solar photovoltaic and energy storage assets on the performance of a residential energy aggregator. *IEEE Transactions on Sustainable Energy*, 11(1):405–414, 2019.

[22] Bonnie Wylie Pratt and Jon D Erickson. Defeat the peak: Behavioral insights for electricity demand response program design. *Energy Research & Social Science*, 61:101352, 2020.

[23] Xing Yan, Yusuf Ozturk, Zechun Hu, and Yonghua Song. A review on price-driven residential demand response. *Renewable and Sustainable Energy Reviews*, 96:411–419, 2018.

[24] Moira L Nicolson, Michael J Fell, and Gesche M Huebner. Consumer demand for time of use electricity tariffs: A systematized review of the empirical evidence. *Renewable and Sustainable Energy Reviews*, 97:276–289, 2018.

[25] Bandana Mahapatra and Anand Nayyar. Home energy management system (hems): Concept, architecture, infrastructure, challenges and energy management schemes. *Energy Systems*, 13(3):643–669, 2022.

[26] Xiuwang Wang, Xinna Mao, and Hossein Khodaei. A multi-objective home energy management system based on internet of things and optimization algorithms. *Journal of Building Engineering*, 33:101603, 2021.

[27] Monica Neukomm, Valerie Nubbe, and Robert Fares. Grid-interactive efficient buildings. Technical report, US Dept. of Energy (USDOE), Washington DC (United States); Navigant ..., 2019.

[28] Heather Buckberry, Jennifer Burke, Michael Starke, Helia Zandi, Jeffrey Munk, Supriya Chinthavali, Christopher Winstead, Ben Ollis, Joe Hagerman, Teja Kuruganti, et al. Smart technologies enable homes to be efficient and interactive with the grid. Technical report, Oak Ridge National Lab.(ORNL), Oak Ridge, TN (United States), 2020.

[29] Lieko Earle, Jeff Maguire, Prateek Munankarmi, and Dave Roberts. Colorado residential retrofit energy district (corred) phase i: Final modeling results. Technical report, National Renewable Energy Lab.(NREL), Golden, CO (United States), 2022.

[30] John Clint. Residential intelligent energy management solution: Advanced intelligence to enable integration of distributed energy resources. Technical report, California energy Commission, Energy Research and Development Division, 2020.

[31] Yantai Huang, Wanliang Wang, and Beiping Hou. A hybrid algorithm for mixed integer nonlinear programming in residential energy management. *Journal of Cleaner Production*, 226:940–948, 2019.

[32] Michael Angelo A Pedrasa, Ted D Spooner, and Iain F MacGill. Scheduling of demand side resources using binary particle swarm optimization. *IEEE Transactions on Power Systems*, 24(3):1173–1181, 2009.

[33] Zhu Wang, Rui Yang, and Lingfeng Wang. Multi-agent control system with intelligent optimization for smart and energy-efficient buildings. In *IECON 2010-36th annual conference on IEEE industrial electronics society*, pages 1144–1149. IEEE, 2010.

[34] MA Pedrasa, ED Spooner, and IF MacGill. Robust scheduling of residential distributed energy resources using a novel energy service decision-support tool. In *ISGT 2011*, pages 1–8. IEEE, 2011.

[35] Avinash Divecha, Stephanie Stockar, and Giorgio Rizzoni. Nonlinear model predictive control for the coordination of electric loads in smart homes. In *Dynamic Systems and Control Conference*, volume 58295, page V003T42A005. American Society of Mechanical Engineers, 2017.

[36] Rania Hassan, Babak Cohanim, Olivier De Weck, and Gerhard Venter. A comparison of particle swarm optimization and the genetic algorithm. In *46th AIAA/ASME/ASCE/AHS/ASC structures, structural dynamics and materials conference*, page 1897, 2005.

[37] Mehdi Rahmani-Andebili and Haiying Shen. Energy scheduling for a smart home applying stochastic model predictive control. In *2016 25th international conference on computer communication and networks (ICCCN)*, pages 1–6. IEEE, 2016.

[38] Maomao Hu and Fu Xiao. Price-responsive model-based optimal demand response control of inverter air conditioners using genetic algorithm. *Applied energy*, 219:151–164, 2018.

[39] Zhuang Zhao, Won Cheol Lee, Yoan Shin, and Kyung-Bin Song. An optimal power scheduling method for demand response in home energy management system. *IEEE transactions on smart grid*, 4(3):1391–1400, 2013.

[40] Amirsaman Arabali, Mahmoud Ghofrani, Mehdi Etezadi-Amoli, M Sami Fadali, and Yahia Baghzouz. Genetic-algorithm-based optimization approach for energy management. *IEEE Transactions on Power Delivery*, 28(1):162–170, 2012.

[41] C Bharathi, Duraisamy Rekha, and V Vijayakumar. Genetic algorithm based demand side management for smart grid. *Wireless personal communications*, 93(2):481–502, 2017.

[42] Chao-Rong Chen, Ming-Jen Lan, Chi-Chen Huang, Ying-Yi Hong, and Steven H Low. Demand response optimization for smart home scheduling using genetic algorithm. In *2013 IEEE International Conference on Systems, Man, and Cybernetics*, pages 1461–1465. IEEE, 2013.

[43] Ahmed Abdulaal, Ramin Moghaddass, and Shihab Asfour. Two-stage discrete-continuous multi-objective load optimization: An industrial consumer utility approach to demand response. *Applied energy*, 206:206–221, 2017.

[44] U.S. Energy Information Administration. Residential energy consumption survey (recs), 2020. `https://www.eia.gov/consumption/residential/data/2020/`.

[45] Johannes Weniger, Tjarko Tjaden, and Volker Quaschning. Sizing of residential pv battery systems. *Energy Procedia*, 46:78–87, 2014.

[46] Sima Aznavi, Poria Fajri, Reza Sabzehgar, and Arash Asrari. Optimal management of residential energy storage systems in presence of intermittencies. *Journal of Building Engineering*, 29:101149, 2020.

[47] Battery pack prices cited below $100/kwh for the first time in 2020, while market average sits at $137/kwh, Dec 2020.

[48] Wenlong Jing, Chean Hung Lai, Wallace SH Wong, and ML Dennis Wong. A comprehensive study of battery-supercapacitor hybrid energy storage system for standalone pv power system in rural electrification. *Applied energy*, 224:340–356, 2018.

[49] Eric Tervo, Kenechi Agbim, Freddy DeAngelis, Jeffrey Hernandez, Hye Kyung Kim, and Adewale Odukomaiya. An economic analysis of residential photovoltaic systems with lithium ion battery storage in the united states. *Renewable and Sustainable Energy Reviews*, 94:1057–1066, 2018.

[50] D Zhang, BS Haran, A Durairajan, Ralph E White, Y Podrazhansky, and Branko N Popov. Studies on capacity fade of lithium-ion batteries. *Journal of Power Sources*, 91(2):122–129, 2000.

[51] P Ramadass, Bala Haran, Parthasarathy M Gomadam, Ralph White, and Branko N Popov. Development of first principles capacity fade model for li-ion cells. *Journal of the Electrochemical Society*, 151(2):A196, 2004.

[52] MM Kabir and Dervis Emre Demirocak. Degradation mechanisms in li-ion batteries: a state-of-the-art review. *International Journal of Energy Research*, 41(14):1963–1986, 2017.

[53] Christoph R Birkl, Matthew R Roberts, Euan McTurk, Peter G Bruce, and David A Howey. Degradation diagnostics for lithium ion cells. *Journal of Power Sources*, 341:373–386, 2017.

[54] Shuangqi Li, Hongwen He, Chang Su, and Pengfei Zhao. Data driven battery modeling and management method with aging phenomenon considered. *Applied Energy*, 275:115340, 2020.

[55] Zachary M Salyer. Identification of optimal fast charging control based on battery state of health. Master's thesis, The Ohio State University, 2020.

[56] Jim Kalupson, Gang Luo, and Christian E Shaffer. Autolion™: A thermally coupled simulation tool for automotive li-ion batteries. *SAE Technical Papers*, 2, 2013.

[57] Xiao-Guang Yang, Yongjun Leng, Guangsheng Zhang, Shanhai Ge, and Chao-Yang Wang. Modeling of lithium plating induced aging of lithium-ion batteries: Transition from linear to nonlinear aging. *Journal of Power Sources*, 360:28–40, 2017.

[58] Rutooj D Deshpande and Dawn M Bernardi. Modeling solid-electrolyte interphase (sei) fracture: coupled mechanical/chemical degradation of the lithium ion battery. *Journal of The Electrochemical Society*, 164(2):A461, 2017.

[59] Izaro Laresgoiti, Stefan Käbitz, Madeleine Ecker, and Dirk Uwe Sauer. Modeling mechanical degradation in lithium ion batteries during cycling: Solid electrolyte interphase fracture. *Journal of Power Sources*, 300:112–122, 2015.

[60] Martin Petit, Eric Prada, and Valérie Sauvant-Moynot. Development of an empirical aging model for li-ion batteries and application to assess the impact of vehicle-to-grid strategies on battery lifetime. *Applied energy*, 172:398–407, 2016.

[61] Johannes Schmalstieg, Stefan Käbitz, Madeleine Ecker, and Dirk Uwe Sauer. A holistic aging model for li (nimnco) o2 based 18650 lithium-ion batteries. *Journal of Power Sources*, 257:325–334, 2014.

[62] Yongzhi Zhang, Rui Xiong, Hongwen He, and Michael G Pecht. Lithium-ion battery remaining useful life prediction with box–cox transformation and monte carlo simulation. *IEEE Transactions on Industrial Electronics*, 66(2):1585–1597, 2018.

[63] Mario Maiorino, Stephanie Stockar, Marco Sorrentino, and Giorgio Rizzoni. Modeling and simulation of residential power demand including transportation. In *Dynamic Systems and Control Conference*, volume 57250, page V002T29A003. American Society of Mechanical Engineers, 2015.

[64] Mithun Goutham. Machine learning based user activity prediction for smart homes. Master's thesis, The Ohio State University, 2020.

[65] Loredana Cristaldi, Marco Faifer, Marco Rossi, and Ferdinanda Ponci. A simple photovoltaic panel model: Characterization procedure and evaluation of the role of environmental measurements. *IEEE transactions on instrumentation and measurement*, 61(10):2632–2641, 2012.

[66] Paul Gilman. Sam photovoltaic model technical reference. Technical report, National Renewable Energy Lab.(NREL), Golden, CO (United States), 2015.

[67] Long Lam, Pavol Bauer, and Erik Kelder. A practical circuit-based model for li-ion battery cells in electric vehicle applications. In *2011 IEEE 33rd International Telecommunications Energy Conference (INTELEC)*, pages 1–9. IEEE, 2011.

[68] Matteo Muratori. *Dynamic management of integrated residential energy systems*. The Ohio State University, 2014.

[69] T Markel, A Meintz, K Hardy, B Chen, T Bohn, J Smart, D Scoffield, R Hovsapian, S Saxena, J MacDonald, et al. Multi-lab ev smart grid integration requirements study. providing guidance on technology development and demonstration. Technical report, National Renewable Energy Lab.(NREL), Golden, CO (United States), 2015.

[70] U.S. Bureau of Labor Statistics. American time use survey, 2003–2009. `https://www.bls.gov/tus/home.htm`.

[71] Kin Cheong Sou, James Weimer, Henrik Sandberg, and Karl Henrik Johansson. Scheduling smart home appliances using mixed integer linear programming. In *2011 50th IEEE conference on decision and control and European control conference*, pages 5144–5149. IEEE, 2011.

[72] Sahar Rahim, Nadeem Javaid, Ashfaq Ahmad, Shahid Ahmed Khan, Zahoor Ali Khan, Nabil Alrajeh, and Umar Qasim. Exploiting heuristic algorithms to efficiently utilize energy management controllers with renewable energy sources. *Energy and Buildings*, 129:452–470, 2016.

[73] Voratas Kachitvichyanukul. Comparison of three evolutionary algorithms: Ga, pso, and de. *Industrial Engineering and Management Systems*, 11(3):215–223, 2012.

[74] Qi Liu, Xiaofeng Li, Haitao Liu, and Zhaoxia Guo. Multi-objective metaheuristics for discrete optimization problems: A review of the state-of-the-art. *Applied Soft Computing*, 93:106382, 2020.

[75] Zahra Beheshti, Siti Mariyam Shamsuddin, and Siti Sophiayati Yuhaniz. Binary accelerated particle swarm algorithm (bapsa) for discrete optimization problems. *Journal of Global optimization*, 57(2):549–573, 2013.

[76] Xing Jin, Ashish Vora, Vaidehi Hoshing, Tridib Saha, Gregory Shaver, R Edwin García, Oleg Wasynczuk, and Subbarao Varigonda. Physically-based reduced-order capacity loss model for graphite anodes in li-ion battery cells. *Journal of Power Sources*, 342:750–761, 2017.

[77] Zachary Salyer, Matilde D'Arpino, and Marcello Canova. Extended physics-based reduced-order capacity fade model for lithium-ion battery cells. *ASME Letters in Dynamic Systems and Control*, 1(4), 2021.

[78] Issam Baghdadi, Olivier Briat, Jean-Yves Delétage, Philippe Gyan, and Jean-Michel Vinassa. Lithium battery aging model based on dakin's degradation approach. *Journal of Power Sources*, 325:273–285, 2016.

[79] Environmental Protection Agency (EPA). Inventory of US Greenhouse Gas Emissions and Sinks, 1990-2019. Technical report, US Environmental Protection Agency, https://www.epa.gov/ghgemissions/us-greenhouse-gas-inventory-report-archive, April 2021.

[80] Georg Bieker. A global comparison of the life-cycle greenhouse gas emissions of combustion engine and electric passenger cars. *communications*, 49(30):847129–102, 2021.

[81] Department of Energy (DOE). FOTW#1221 Model year 2021 all-electric vehicles had a median driving range about 60% that of gasoline powered vehicles. January 2022. https://www.energy.gov/eere/vehicles/articles/fotw-1221-january-17-2022-model-year-2021-all-electric-vehicles-had-median.

[82] Mollie Putzig, Jesse Bennett, Abigail Brown, Stephen Lommele, and Kaylyn Bopp. Electric vehicle basics. Technical report, National Renewable Energy Lab.(NREL), Golden, CO (United States), 2021.

[83] SJ Drake, M Martin, DA Wetz, JK Ostanek, SP Miller, JM Heinzel, and A Jain. Heat generation rate measurement in a li-ion cell at large c-rates through temperature and heat flux measurements. *Journal of Power Sources*, 285:266–273, 2015.

[84] Anna Tomaszewska, Zhengyu Chu, Xuning Feng, Simon O'Kane, Xinhua Liu, Jingyi Chen, Chenzhen Ji, Elizabeth Endler, Ruihe Li, Lishuo Liu, et al. Lithium-ion battery fast charging: A review. *ETransportation*, 1:100011, 2019.

[85] Matthew Keyser, Ahmad Pesaran, Qibo Li, Shriram Santhanagopalan, Kandler Smith, Eric Wood, Shabbir Ahmed, Ira Bloom, Eric Dufek, Matthew Shirk, et al. Enabling fast charging–battery thermal considerations. *Journal of Power Sources*, 367:228–236, 2017.

[86] Drasti Patel, James B Robinson, Sarah Ball, Daniel JL Brett, and Paul R Shearing. Thermal runaway of a li-ion battery studied by combined arc and multi-length scale x-ray ct. *Journal of The Electrochemical Society*, 167(9):090511, 2020.

[87] Guodong Xia, Lei Cao, and Guanglong Bi. A review on battery thermal management in electric vehicle application. *Journal of power sources*, 367:90–105, 2017.

[88] Caiping Zhang, Jiuchun Jiang, Yang Gao, Weige Zhang, Qiujiang Liu, and Xiaosong Hu. Charging optimization in lithium-ion batteries based on temperature rise and charge time. *Applied energy*, 194:569–577, 2017.

[89] Zhen Guo, Bor Yann Liaw, Xinping Qiu, Lanlan Gao, and Changshui Zhang. Optimal charging method for lithium ion batteries using a universal voltage protocol accommodating aging. *Journal of Power Sources*, 274:957–964, 2015.

[90] Xiaosong Hu, Hector E Perez, and Scott J Moura. Battery charge control with an electro-thermal-aging coupling. In *Dynamic Systems and Control Conference*, volume 57243, page V001T13A002. American Society of Mechanical Engineers, 2015.

[91] Meng Xu, Rui Wang, Peng Zhao, and Xia Wang. Fast charging optimization for lithium-ion batteries based on dynamic programming algorithm

and electrochemical-thermal-capacity fade coupled model. *Journal of Power Sources*, 438:227015, 2019.

[92] L Tang, G Rizzoni, and A Cordoba-Arenas. Battery life extending charging strategy for plug-in hybrid electric vehicles and battery electric vehicles. *IFAC-PapersOnLine*, 49(11):70–76, 2016.

[93] Peter M Attia, Aditya Grover, Norman Jin, Kristen A Severson, Todor M Markov, Yang-Hung Liao, Michael H Chen, Bryan Cheong, Nicholas Perkins, Zi Yang, et al. Closed-loop optimization of fast-charging protocols for batteries with machine learning. *Nature*, 578(7795):397–402, 2020.

[94] Zachary Salyer, Matilde D'Arpino, Marcello Canova, and Yann Guezennec. Optimal health-conscious fast charging of lithium ion batteries. *IFAC-PapersOnLine*, 54(20):516–521, 2021.

[95] Li Zhang, Brendan Shaffer, Tim Brown, and G Scott Samuelsen. The optimization of dc fast charging deployment in california. *Applied energy*, 157:111–122, 2015.

[96] Long Lam, Pavol Bauer, and Erik Kelder. A practical circuit-based model for li-ion battery cells in electric vehicle applications. In *2011 IEEE 33rd International Telecommunications Energy Conference (INTELEC)*, pages 1–9. IEEE, 2011.

[97] Xianke Lin, Kavian Khosravinia, Xiaosong Hu, Ju Li, and Wei Lu. Lithium plating mechanism, detection, and mitigation in lithium-ion batteries. *Progress in Energy and Combustion Science*, 87:100953, 2021.

[98] Markos Koseoglou, Evangelos Tsioumas, Dimitra Ferentinou, Iordanis Panagiotidis, Nikolaos Jabbour, Dimitrios Papagiannis, and Christos Mademlis. Lithium plating detection using differential charging current analysis in lithium-ion batteries. *Journal of Energy Storage*, 54:105345, 2022.

[99] Dimitri Bertsekas. *Dynamic programming and optimal control: Volume I*, volume 1. Athena scientific, 2012.

[100] Russell Eberhart and James Kennedy. A new optimizer using particle swarm theory. mhs'95. In *Proceedings of the sixth international symposium on micro machine and human science*, volume 1, pages 39–43. Ieee Piscataway, NJ, USA, 1995.

[101] Riccardo Poli, James Kennedy, and Tim Blackwell. Particle swarm optimization. *Swarm intelligence*, 1(1):33–57, 2007.

[102] Olle Sundstrom and Lino Guzzella. A generic dynamic programming matlab function. In *2009 IEEE control applications,(CCA) & intelligent control,(ISIC)*, pages 1625–1630. IEEE, 2009.

[103] Peter Keil and Andreas Jossen. Calendar aging of nca lithium-ion batteries investigated by differential voltage analysis and coulomb tracking. *Journal of The Electrochemical Society*, 164(1):A6066, 2016.